

**KINEMATICS OF LOCALIZATION ACCOMPANYING
LÜDERS INSTABILITY USING INFRARED THERMAL
IMAGING AND DIGITAL IMAGE CORRELATION**

By

**N. SRINIVASAN
(ENGG02200904027)**

Indira Gandhi Centre for Atomic Research, Kalpakkam

A thesis submitted to the

Board of Studies in Engineering Sciences

In partial fulfillment of requirements

for the Degree of

DOCTOR OF PHILOSOPHY

of

HOMI BHABHA NATIONAL INSTITUTE

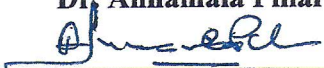


AUGUST, 2014

Homi Bhabha National Institute

Recommendations of the Viva Voce Board

As members of the Viva Voce Board, we certify that we have read the dissertation prepared by N.Srinivasan titled "Kinematics of Localization Accompanying Lüders Instability Using Infrared Thermal Imaging and Digital Image Correlation" and recommend that it may be accepted as fulfilling the thesis requirement for the award of Degree of Doctor of Philosophy.

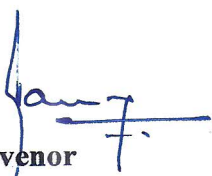
Chairman	 Dr. A.K. Bhaduri	29/4/2015 Date
Guide	Dr. M.D. Mathew - Retired	Date
Convenor/ Technology Adviser	 Dr. B. Venkatraman	Date 29-04-2015
Member 1	Dr. R.S. Keshavamurthy - Retired	Date
Member 2	 Dr. B.P.C. Rao	29/4/2015 Date
External Examiner	 Dr. Annamala Pillai	29-04-2015 Date

Final approval and acceptance of this thesis is contingent upon the candidate's submission of the final copies of the thesis to HBNI.

I/We hereby certify that I/we have read this thesis prepared under my/our direction and recommend that it may be accepted as fulfilling the thesis requirement.

Date: 29.04.2015

Place: KALPAKKAM


Convenor

STATEMENT BY AUTHOR

This dissertation has been submitted in partial fulfillment of requirements for an advanced degree at Homi Bhabha National Institute (HBNI) and is deposited in the Library to be made available to borrowers under rules of the HBNI.

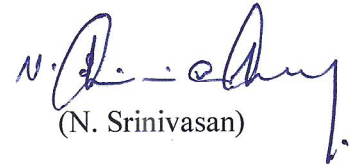
Brief quotations from this dissertation are allowable without special permission, provided that accurate acknowledgement of source is made. Requests for permission for extended quotation from or reproduction of this manuscript in whole or in part may be granted by the Competent Authority of HBNI when in his or her judgment the proposed use of the material is in the interests of scholarship. In all other instances, however, permission must be obtained from the author.


(N. Srinivasan)

DECLARATION

I, hereby declare that the investigation presented in the thesis has been carried out by me.

The work is original and has not been submitted earlier as a whole or in part for a degree / diploma at this or any other Institution / University.


(N. Srinivasan)

List of Publications arising from the thesis

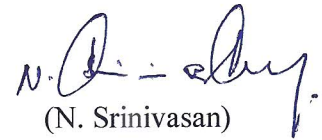
Journals

1. “Study on the kinetics of thermomechanical response accompanying plastic instability in mild steel”, **Srinivasan Nagarajan**, Raghu Narayanaswamy, Venkatraman Balasubramaniam, **Mech. Mater.**, 2015, 80, 27-36.
2. “An insight into Lüders deformation using advanced imaging techniques”, **Srinivasan Nagarajan**, Raghu Narayanaswamy, Venkatraman Balasubramaniam, **J. Mater. Eng. Per.**, 2013, 22, 3085-3092.
3. “Study on local zones constituting to band growth associated with inhomogeneous plastic deformation”, **Srinivasan Nagarajan**, Raghu Narayanaswamy, Venkatraman Balasubramaniam, **Mater. Lett.**, 2013, 105, 209-212.
4. “Advanced imaging for early prediction and characterization of zone of Lüders band nucleation associated with pre-yield microstrain”, **Srinivasan Nagarajan**, Raghu N., Venkatraman B, **Mater. Sci. Eng. A**, 2013, 561, 203-211.
5. “Study on Lüders deformation in welded mild steel using infrared thermography and digital image correlation”, **N. Srinivasan**, N. Raghu, B. Venkatraman, **Adv. Mater. Res.**, 2012, 585, 82-86.
6. “Discontinuous yielding behavior of welded mild steel accompanying Lüders instability: A thermomechanical study”, **N. Srinivasan**, N. Raghu, B. Venkatraman, **Submitted to Mater. Sci. Eng. A**.
7. “Lüders instability: A review of experimental findings”, **N. Srinivasan**, N. Raghu, B. Venkatraman, **To be submitted to J. Mater. Process. Technol.**

Conference Proceedings/Presentations

1. “Dynamics of strain localization associated with Lüders deformation - An insight”, **Srinivasan Nagarajan**, Raghu Narayanaswamy, Venkatraman Balasubramaniam, **Exp. Appl. Mech.**, **2015, 6, 187-194**: Proceedings of the 2014 Annual Conference on Experimental and Applied Mechanics (**SEM-2014**), 2-5, June 2014, Hyatt Regency Greenville, Greenville, South Carolina, U.S.A.
2. “Enhanced understanding on Lüders band phenomenon using infrared thermography and digital image correlation”, **Srinivasan Nagarajan**, Raghu N., Venkatraman B., Asia Pacific Conference on Nondestructive Testing (**APCNDT-2013**), 18-22, November 2013, Hotel Renaissance, Mumbai, Maharashtra, India.
3. “Digital image correlation - A non-contact, imaging tool for studying heterogeneous deformation”, **Srinivasan Nagarajan**, Raghu N., Venkatraman B, International Conference on Pressure Vessels and Piping (**OPE-2013**), 13-16, January 2013, Radisson Blu Resort, Mamallapuram, Tamil Nadu, India.
4. “Study on band growth aspects of Lüders deformation in mild steel using digital image correlation”, **Srinivasan Nagarajan**, Raghu N., Venkatraman B, National Seminar on Nondestructive Evaluation (**NDE-2012**), 10-12, December 2012, Hotel Clarks Inn Suits, Ghaziabad, New Delhi, India.
5. “Creep deformation associated with yield point phenomenon in mild steel using digital image correlation and infrared thermography”, **Srinivasan Nagarajan**, Raghu N., Venkatraman B, National Metallurgist Day - Annual Technical Meeting (**NMD-ATM-2012**), 16-19, November 2012, XLRI campus, Jamshedpur, Jharkhand, India.

6. "Characterization of Lüders deformation in mild steel using infrared thermography and digital image correlation" **Srinivasan Nagarajan**, Raghu N., Venkatraman B., National Metallurgist Day - Annual Technical Meeting (NMD-ATM-2012), 16-19, November 2012, XLRI campus, Jamshedpur, Jharkhand, India.
7. "Thermal and strain patterns associated with Lüders deformation in mild steel using infrared thermography and digital image correlation", **N. Srinivasan**, N. Raghu, B. Venkatraman, Nandagopal, National Seminar on Nondestructive Evaluation (NDE-2011), 8-10, December 2011, Convention Centre, Chennai, Tamil Nadu, India.


(N. Srinivasan)

Dedicated to my family

ACKNOWLEDGEMENTS

I was able to complete this dissertation with the support of several people. First and foremost, I wish to thank my research advisor, **Dr. B. Venkatraman** for providing me complete freedom to experiment with my ideas, guidance when needed and unconditional support throughout the course of my research work.

The advice and guidance from my Guide, **Dr. M.D. Mathew** is gratefully acknowledged. I am deeply grateful to **Dr. A.K. Bhaduri**, Chairman, Doctoral Committee for his discussion and suggestions on my work during the review meetings. I also thank other committee members **Dr. R.S. Keshavamurthy** and **Dr. B.P.C. Rao** for their valuable comments.

I am very much thankful to my well wisher **Shri N. Raghu** for his involvement and inputs in my work. In addition to our academic collaboration, I greatly value the close personal rapport with him which we have forged over the years.

I would like to express my sincere gratitude to all the Directors of IGCAR during my tenure, **Dr. Baldev Raj**, **Shri S.C. Chetal** and **Dr. P.R. Vasudeva Rao** for their support and encouragement. Special thanks to **Shri B. Ananthapadmanaban**, Head, QAD for his concern and good wishes.

I thank **Dr. T. Jayakumar**, Chairman, Standing Committee and **Dr. G. Sasikala**, Dean and Member Secretary, Engineering Sciences, HBNI at IGCAR for their efforts and help in all the academic procedures. I also thank **Dr. M. Saibaba**, **Dr. Vidya Sundararajan** and **Smt. Jalaja Madhanmohan**, RMG for taking care of course work activities and ensuring comfortable stay at enclave.

I gratefully acknowledge the research fellowship from **Indira Gandhi Centre for Atomic Research, Department of Atomic Energy**. I also thank **Science and Engineering Research Board, Department of Science and Technology** and

Homi Bhabha National Institute for providing me the international travel support to present my doctoral thesis work in SEM-2014 annual conference at U.S.A.

My big thanks to **Ms. Anastasia Iziumova** and **Prof. Oleg A. Plekhov**, Institute for Continuous Media Mechanics, Russian Academy of Sciences for their valuable discussions on the heat power estimation. I also thank **Shri S. Raviprakash**, Pyrodynamics, for his advice on various practical issues while experimenting with Digital Image Correlation.

I deeply appreciate the works of **Mr. K.A. Gopal** and **Mr. R. Saxena**, RIRD and **Mr. G. Kempulraj**, **Mr. P. Shanmugam**, **Mr. T. Saravanan** and **Mr. V. Rajendran**, CWD in machining and fabrication of tensile specimens.

My heartfelt thanks to **Mr. D. Sharath**, **Mrs. D. Chitra**, and **Mr. D. Kuppusamy**, QAD and **Dr. V. Karthik**, **Mr. P. Visweswaran** and **Mr. Sukumar**, PIED for their experimental assistance.

I also thank my lab mates, **Mrs. M. Menaka**, **Mrs. E. Kani**, **Mrs. K. Vani** and other staff members of QAD for their support.

I would like to acknowledge my batch mate friends, **Mr. A. Masilamani Chelladurai**, **Mr. Shashwat Kumar Swain**, **Ms. N. Priyadarshini**, **Mr. S. Shuaib Ahmed**, **Mr. Ravikirana** and **Mr. C. Arunchandran**, and all the senior and junior friends for making my academic ambience comfortable and pleasant.

This dissertation would have never been possible without the love and patience of my family members: mother **Mrs. N. Madhavi**, father **Mr. P. Nagarajan**, brother **Mr. N. Murugan**, sisters **Mrs. N. Meena** and **Mrs. N. Chandra** and babies **S.M. Adhirshta** and **M. Praneetha Arshini** who have supported me despite their unwillingness of my separation from them. My love and gratitude for them can hardly be expressed in words.

CONTENTS

	Page No.
SYNOPSIS	i
LIST OF FIGURES	xi
LIST OF TABLES	xiv
LIST OF ABBREVIATIONS	xv
LIST OF SYMBOLS	xvi
CHAPTER 1 INTRODUCTION	1
1.1 Materials and Deformation	1
1.2 Infrared Thermography and Digital Image Correlation	2
1.3 Plastic instabilities	6
1.3.1 Proposed theories and experimental works on Lüders instability - International scenario	8
1.3.1.1 Microscopy	9
1.3.1.2 Photography	10
1.3.1.3 Strain gauges and Extensometers	11
1.3.1.4 Acoustic emission	12
1.3.1.5 Magnetic Barkhausen noise and Flux leakage	13
1.3.1.6 Speckle pattern interferometry	13
1.3.1.7 Studies on Lüders deformation using IRT and DIC	14
1.4 Motivation for the study	15
1.5 Objectives and Significance of the work	17
1.6 Outline of the dissertation	18
CHAPTER 2 INFRARED THERMAL IMAGING AND DIGITAL IMAGE CORRELATION: THEORY AND EXPERIMENTAL APPROACH	20
2.1 Infrared thermal imaging	20
2.1.1 Infrared imaging system	21
2.1.1.1 Detectors	22
2.1.1.2 Cooling systems	25

2.1.2	Advantages of IR imaging	25
2.1.3	Disadvantage	25
2.2	Approaches in Infrared thermography	26
2.3	Theory of IR imaging	26
2.4	Digital image correlation	28
2.4.1	Theory of DIC	28
2.4.2	Practical considerations for minimization of errors in 2D DIC	32
2.4.3	Advantages of DIC	33
2.4.4	Disadvantage	33
2.5	Thermal and optical imaging systems used in the present study	33
2.6	Material and Qualification	34
2.7	Experimental setup and Methodology	35
CHAPTER 3	STUDIES ON LÜDERS BAND FORMATION AND GROWTH KINEMATICS	38
3.1	Experimental	38
3.2	Spatiotemporal evolutions of temperature and strain accompanying Lüders instability	39
3.2.1	Region I - Microstrain evolutions, Thermoelasticity and Lüders band formation	41
3.2.1.1	Thermoelastic effect and Microstrain evolutions	43
3.2.1.2	Lüders band formation	45
3.2.2	Region II - Kinematics of Lüders band front propagation	48
3.2.2.1	Stress-strain distribution across the band front	48
3.2.3	Region III - Uniform strain hardening	55
3.3	Local zones of Lüders band and band growth behavior	56
CHAPTER 4	HEAT POWER AND STRAIN RATE BASED STUDY ON LÜDERS INSTABILITY	62
4.1	Background Theory	63
4.1.1	Thermomechanical frame work	63

4.1.2	Heat power estimation	64
4.1.3	Estimation of plastic, dissipated heat and stored powers	65
4.2	Methodology adopted for heat power and strain rate estimation	67
4.3	Spatiotemporal evolutions of temperature and heat power	67
4.4	Lüders band formation and growth in regions I and II	70
4.5	Delayed localized yielding in regions II and III	73
4.6	Plastic, dissipated heat and stored powers accompanying Lüders instability	75
4.7	Energy conversion rate ratios	78
CHAPTER 5	DISCONTINUOUS YIELDING BEHAVIOR OF WELDED MILD STEEL ACCOMPANYING LÜDERS INSTABILITY	81
5.1	Experimental	82
5.2	Thermomechanical characterization	83
5.2.1	Nucleation and band growth kinematics	85
5.2.2	Uniform strain hardening	88
5.2.3	Local variations of temperature, heat power, strain and strain rate	89
5.2.4	Local variations of the thermomechanical parameters	92
5.2.5	Energy conversion rate ratio	94
CHAPTER 6	SUMMARY, CONCLUSIONS, HIGHLIGHTS, CONTRIBUTIONS AND FUTURE DIRECTIONS	97
6.1	Summary and conclusions	97
6.2	Highlights	101
6.3	Contributions	102
6.4	Future directions	103
	REFERENCES	105

SYNOPSIS

1. Introduction

Strain ageing of materials such as low carbon steels, mild steels and Al-Mg alloys involving interaction of solute atoms with dislocations leads to an unstable elastic-plastic transition and plastic flow commonly called as plastic instability which deteriorates the formability and ductility of such steels. Instability in the plastic flow is generally characterized by the appearance/formation of deformation bands on the material surface at the macroscopic scale. These deformation bands induce surface roughness thereby affecting the surface quality of sheet metal products during metal forming operations and also affect the high cycle fatigue properties of components by increasing the number of crack nucleation sites on the surface. Lüders deformation and Portevin-Le Chatelier (PLC) effect are the two instability phenomena commonly observed in such structural steels which are widely used in many industries including automobile and nuclear etc. Lüders instability occurs because of static strain ageing involving interaction of the interstitial solute atoms with the dislocations generated after initial plastic deformation resulting in locking up of dislocations. In carbon steels, carbon atoms act as solute atmospheres. On the other hand, PLC effect occurs as a result of dynamic strain ageing involving interaction between solute atoms and dislocations during plastic deformation. Of these, Lüders instability is of prime concern to industrial manufacturers as the associated strain ageing generally occurs during material storage, which may lead to production loss since maintaining surface quality is mandatory for many applications. Lüders phenomenon is characterized by discontinuous yield points in the load-elongation curve, namely upper and lower yield point followed by a load plateau involving strain localizations in the form of deformation bands called Lüders bands [1]. Lüders band is a band (collection) of slip lines representing the localized (inhomogeneous) plastic deformation exhibited by a

material. The upper yield point corresponds to the unlocking of the locked dislocations or generation of fresh dislocations and lower yield point corresponds to the propagation of the unlocked or fresh dislocations. The collective and self-organized behavior of these dislocations manifests on the surface of the material as band front propagation (band growth). Lüders deformation is then followed by uniform strain hardening.

Although Lüders instability has been studied intensively for more than three decades, kinematics of localization accompanying Lüders deformation and the corresponding macroscopic manifestations are yet to be fully understood. The need for better understanding of the Lüders phenomenon in materials through versatile characterization tools is in demand even today. Over the years, many techniques such as optical and electron microscopy [2-3], photography [4-5], extensometers [6], strain gauges [7-8], acoustic emission [9], magnetic Barkhausen noise emission [10] and speckle interferometry [11-12] etc., have been used to study nucleation and growth behavior of Lüders bands, spatiotemporal evolutions of strain localizations and the macroscopic band characteristics. Each of these techniques has its own advantages and limitations with respect to spatiotemporal characterization, magnitude of strain measurement, area of measurement and material to be studied etc.

The last two decades have seen extensive developments in the imaging, non destructive evaluation techniques, particularly in the field of infrared thermal imaging and digital image correlation. Infrared thermography (IRT) is a technique in which the surface temperature profile of the object is mapped through the infrared radiations emitted by it using a suitable infrared imaging system. Digital image correlation (DIC) is an optical method that maps the surface displacement and strain during deformation by correlating the undeformed image with the deformed one through gray scale matching. The main advantages of these techniques with respect to deformation studies are: 1. They are non

invasive, non contact, fast and reliable. 2. They can be applied on engineering components
3. They have large field of view 4. Spatiotemporal characterization of deformations is possible 4. Real time visualization of plastic strain evolutions is also possible. The limitations include thermal diffusion during deformation, which may affect the interpretation of strain localization. On the other hand, strain resolution in DIC is relatively low.

A detailed review of literature reveals that significant works have been reported on Lüders instability using IRT and DIC [13-16]. One of the earliest works in this domain is by Louche et al. [13], who have studied the Lüders band velocity using dissipative heat source. Wattrisse et al. [14] have estimated the Lüders band front orientation using DIC. Nogueira de codes et al. [15] have applied IRT and DIC simultaneously to study the spatiotemporal evolution of Lüders and PLC bands. Recently, Coer et al. [16] have applied DIC for measuring Lüders band width and velocity using shear strain and shear strain rate evolutions.

2. Motivation for the study

Review of literature reveals that both conventional and advanced imaging techniques have been primarily applied to study the macroscopic characteristics such as band front velocity, band width, band front orientation and propagation kinematics, Lüders stress and Lüders strain etc. However, there are still grey areas which have not been investigated / understood completely and need further study. These include areas such as pre-yield microstrain and its influence on band formation, band nucleation and growth mechanism, stress-strain-strain rate distributions across the band front, delayed localized yielding and influence of dissimilar microstructures on the Lüders yielding behavior etc. Also, the rate of energy conversions during strain localizations accompanying Lüders instability in the load plateau and uniform deformation remains unclear. Application of

IRT and DIC which can provide information on the spatiotemporal evolutions of strain localization is expected to provide enhanced understanding in the identified gap areas and that forms the motivation for this study. However, even with IRT and DIC there are few issues such as thermal diffusion in the thermal field and the track record of strain in the DIC strain field that may mask the manifestations of any small strain evolutions and hence should be taken care. Among the steels which undergo Lüders instability, IS 2062 grade E250 B mild steel is preferred as the primary structural material in many industries because of its good malleability, ductility and weldability. Therefore, a study on the Lüders deformation behavior in this steel using IRT and DIC techniques would generate a knowledge base not only for the companies involved in metal forming operations, but also for the industries employed with structural components made of this steel.

3. Objectives and Scope of the work

In this work Lüders instability phenomenon in IS 2062 grade E250 B mild steel is investigated by combined application of IRT and DIC techniques. It attempts to provide possible insights into the nature of Luders phenomenon by drawing relevant correlations of macroscopic thermal and strain evolutions to the dislocation activities underlying proposed earlier through models and experimental microscopic characterizations. The primary focus is on critical areas that had earlier lacked complete understanding such as microstrain localizations leading to band nucleation and the associated band formation behavior, deformations in the local zones within the Lüders band which constitutes to the band growth, stress-strain-strain rate distribution across the band front, occurrence of delayed localized during uniform strain hardening etc. The other important objective of this works is to estimate the heat power and strain rate evolutions during Lüders instability which is expected to reveal the associated kinematics of localization without the effect of signatures of prior plastic deformation. The difference in fractional dissociation of applied

mechanical power during Lüders band nucleation and growth in the load plateau and uniform strain hardening is also studied through estimation of dissipative heat and stored powers which would reveal the difference in hardening/softening behavior of materials during strain localizations associated with different Lüders bands. This work also aims to study the influence of dissimilar microstructures and the associated stress concentrations on the Lüders yielding behavior of welded mild steel. It also focuses on studying the rate of energy conversions on local zones to understand the hardening/softening behavior of the zones with dissimilar microstructures during Lüders instability and uniform strain hardening.

4. Description of the work

The present work discusses the inhomogeneous yielding behavior associated with Lüders instability in IS 2062 grade E250 B mild steel using IRT and DIC. It highlights the potential of combined application of IRT and DIC in providing an enhanced understanding on the Lüders deformation through visualization of spatiotemporal evolution of the associated strain localizations. For the first time, Lüders instability is studied in this steel using IRT and DIC techniques. *Studies on the occurrence of the delayed localized yielding, deformation behavior of local zones within the Lüders band constituting to band growth and discontinuous yielding behavior of welded mild steel with dissimilar microstructures accompanying Lüders instability are the major highlights of this dissertation. Also, for the first time, the difference in deformation behavior of local zones of welded mild steel during Lüders band kinematics in the load plateau and uniform deformation in the strain hardening region has been studied and quantified through characteristic variations of the thermomechanical parameters such as dissipative heat power, stored power and the energy conversion rate ratio.* The dissertation framework is as follows.

Chapter 1 - Introduction

Chapter 1 begins with an introduction to plastic instabilities with focused discussion on Lüders instability. Theory of Lüders deformation and the associated yield point phenomenon have been discussed in detail based on proposed dislocation concepts. Adverse effects of this phenomenon and the industrial need for an understanding on its deformation behavior has been briefed. Works reported on Lüders instability using conventional techniques such as optical and electron microscopy, photography, strain gauges, micrometers, extensometers, acoustic emission, magnetic Barkhausen noise and speckle interferometry etc., have been reviewed in detail. With brief introductions to infrared thermal imaging and digital image correlation, advantages of these techniques over other conventional techniques in studying strain localizations accompanying plastic instabilities are highlighted. A critical review of the works carried out up to date on Lüders instability using IRT and DIC is presented. The identified gap areas, motivation drawn out of them, objectives and scope of the present work are also discussed.

Chapter 2 - Infrared thermal imaging and Digital image correlation: Theory and experimental approach

In chapter 2, a detailed discussion on the principle, theory, advantages and disadvantages of experimental techniques employed such as IRT and DIC are discussed. The experimental setup and methodology adopted to study the inhomogeneous plastic deformation behavior are explained in detail. The parameters used with the testing machine, imaging techniques and the associated post processing procedures are outlined. The importance and practical significance to study the Lüders instability in IS 2062 grade E250 B mild steel based on its applications are also highlighted.

Chapter 3 - Studies on Lüders band formation and growth kinematics

The kinematics of localization accompanying Lüders band nucleation and growth based on temperature and strain evolutions is addressed in chapter 3. The characteristic evolution of microstrain, Lüders band nucleation and growth mechanism, band front propagation, stress-strain-strain rate distribution across the band front etc., are studied and compared with models and concepts proposed in these areas [6, 17]. The localization of microstrain on approaching close to macroscopic yield stress and their self organized nature has led to early visualization of zone of Lüders band nucleation. Strain is observed to be symmetrically distributed on either side of the nucleation zone and found to evolve much before the band front. Deformation behavior of local zones within the Lüders band, namely effective width and active zone constituting to the band growth are also discussed through strain and strain rate evolutions. A significant observation arising from this study is that the effective width varies during band growth and active zone grows irregularly representing the irregularity in the two stage band growth mechanism proposed earlier [6]. Strain rate is always found to peak in the effective width and vary in the active zone.

Chapter 4 - Heat power and strain rate based study on Lüders instability

Chapter 4 discusses the nucleation and growth kinematics of Lüders bands using heat power and strain rate evolutions highlighting their advantages over thermal and strain evolutions in revealing the associated strain localizations without the influence of signatures of prior plastic localizations. Estimation of the heat power from the experimentally observed temperature data using two dimensional heat equation has been attempted. The efficiency of this approach in revealing the occurrence of delayed localized yielding in the end of the load plateau and during the initial stages of uniform strain hardening has also been demonstrated. Strain localization associated with nucleation of

Lüders bands are observed in the heat power and strain rate fields much ahead of the thermal and strain fields. Theoretical approach to calculate thermomechanical parameters such as dissipative heat power, stored power and energy conversion rate ratios are also discussed in detail. Although stored power is mostly observed to be higher than heat power since the inception of plastic strain, fraction of heat power dissipated is found to be relatively more in the load plateau involving strain localizations than the uniform strain hardening region.

Chapter 5 - Discontinuous yielding behavior of welded mild steel accompanying Lüders instability

In chapter 5, discontinuous yielding behavior of TIG welded mild steel accompanying Lüders instability is studied based on spatiotemporal evolutions of temperature, heat power, strain and strain rate. The influence of dissimilar microstructures and the associated stress concentrations at the interfaces of dissimilar microstructures on the microstrain evolutions leading to initiation of Lüders band is examined. From thermal and strain fields, it is observed that Lüders band initially nucleates in the weld zone and later becomes unstable following which stable bands nucleates from the fillets and yields the gauge length. However, bands are found ceased to propagate in the weld and heat affected zones. On the other hand, heat power and strain rate evolutions revealed mild strain localizations in the weld and heat affected zones during growth of bands in the load plateau. The observed yielding behavior of base metal, weld and heat affected zones is discussed and validated with inputs from optical micrographs and hardness measurements. Estimated thermomechanical parameters such as dissipative heat power, stored power and energy conversion rate ratios on the local zones confirmed the mild yielding of weld and heat affected zones by both unstable and stable bands in the load plateau.

Chapter 6 - Summary, Conclusions, Contributions and Future directions

Chapter 6 summarizes the salient observations and highlights the major conclusions and contributions from this thesis. It also sheds light on the newer vistas and the directions in which the present work can be extended further. Thermal and strain evolutions accompanying microstrain localizations have led to early visualization of zone of Lüders band nucleation much before the macroscopic yield point. Strain distribution on either side of the strain hardened zone has been found to be symmetrical. The effective width of Lüders band varies in the load plateau and active zone increases with irregular magnitude confirming the irregularity involved in the two stage band growth mechanism. Strain rate is always found to peak in the effective width and vary in the active zone. The occurrence of delayed yielding during the initial stages of strain hardening has been successfully mapped through heat power and strain rate evolutions. The fraction of heat power dissipated is relatively more in the load plateau involving Lüders band formation and growth than the uniform strain hardening region. In welded mild steel, microstrain initially localizes in the weld zone leading to an unstable band nucleation although stable bands arise from the fillets of specimen. Weld and heat affected zones were observed to experience very less deformation through Lüders bands in the load plateau due relatively higher mechanical properties.

It is also felt that future work should focus on studying the thermomechanical response across the band at the grain scale by achieving high spatial resolution in a local region, which would provide an insight into the micro mechanisms of band growth involved. Study can be extended further on the effect of interrupted and biaxial loading conditions on the strain localization behavior accompanying Lüders instability.

References

- [1] E.O. Hall, *Yield Point Phenomena in Metals and Alloys*, Macmillan (1970).
- [2] J.C. Suits, B. Chalmers, *Acta. Metall.*, 9 (1961) 854-860.
- [3] S. Mahajan, D. Brasen, P. Haasen, *Acta. Metall.*, 27 (1979) 1165-1173.
- [4] V.S. Ananthan and E.O. Hall, *Acta. Metall. Mater.*, 39 (1991) 3153-3160.
- [5] H.B. Sun, F.Yoshida, M.Ohmori, X.Ma, *Mater. Lett.*, 57 (2003) 4535-4539.
- [6] G.T. Van Rooyen, *Mater. Sci. Eng.*, 3 (1968/1969) 105-117.
- [7] S. Kyriakides, J.E. Miller, *J. Appl. Mech.*, 67 (2000) 645-654.
- [8] J. Zhang , Y. Jiang, *Int. J. Plast.*, 21 (2005) 651-670.
- [9] T. V. Muravev, L. B. Zuev, *Tech. Phys.*, 53 (2008) 1094-1098.
- [10] Dhar, L. Clapham, D. L. Atherton, *J. Mater. Sci.*, 37 (2002) 2441-2446.
- [11] Q. Zhang, X. Wu, *Proc. SPIE*, 5058 (2003) 257-265
- [12] S.Yoshida, H. Ishii, K. Ichinose, K. Gomi, K. Taniuchi, *Trans. ASME*, 72 (2005) 792-794.
- [13] H. Louche and A. Chrysochoos, *Mater. Sci. Eng. A*, 307 (2001) 15-22.
- [14] B. Wattrisse, A. Chrysochoos, J.M. Muracciole, M. Nemoz-Gaillard, *Eur. J. Mech. A*, 20 (2001) 189-211.
- [15] R. Nogueira de Codes, O.S. De Hopperstad, O. Engler, O.-G. Lademo, J.D. Embury, A. Benallal, *Metall. Mater. Trans. A*, 42A (2011) 3358-3369.
- [16] J. Coer, P.Y. Manach, H. Laurent, M.C. Oliveira, L.F. Menezes, *Mech. Res. Comm.*, 48 (2013) 1-7.
- [17] J. Friedel, *Dislocations*, Pergamon Press Ltd (1967).

LIST OF FIGURES

Figure No.	Figure Caption	Page No.
2.1	Atmospheric transmission spectrum of infrared radiation	21
2.2	Spectral radiance of a black body	27
2.3	Displacement field $u(x, y)$ and $v(x, y)$ between initial image and a deformed image	29
2.4	Iterative procedure to obtain precise displacement field	31
2.5	Optical micrograph of IS 2062 grade B mild steel	34
2.6	Schematic of specimen dimension	35
2.7	Schematic of experimental setup	36
3.1	Load-time curve at 1.3×10^{-4} /s strain rate	39
3.2	Local zones of interest along the gauge length	40
3.3	Temporal evolutions of (a) temperature in various local zones, (b) temperature in zone 1 during initial stages of elastic loading, (c) strain in various local zones and (d) strain in zone 1 during initial stages of elastic loading	41
3.4	Thermal, strain fields and their axial profiles in the interval of 65s - 200s	44
3.5	Nucleation and formation of Lüders band	46
3.6	Nucleation and development of Lüders band - Friedel	47
3.7	(a) Stress and (b) Strain distribution across the Lüders band front - Van Rooyen	49
3.8	Thermal, strain fields and their axial profiles at 300 s	50
3.9	Thermal and strain fields revealing the second band formation and growth	53
3.10	Thermal, strain fields and their axial profiles in the interval of 360-405s	54

Figure No.	Figure Caption	Page No.
3.11	Thermal and strain fields in region III	55
3.12	Load vs. time curve for (a) specimen 1 and (b) specimen 2	56
3.13	Strain field, strain rate field and their axial profiles at 60 s and 94 s for specimen 1	57
3.14	Variation of effective width and active zone in the load plateau for (a) specimen 1, (b) band 1 of specimen 2 and (c) band 2 of specimen 2	59
4.1	Spatiotemporal evolutions of (a) temperature and (b) heat power accompanying Lüders instability	68
4.2	Temporal variations of different terms of heat diffusion equation accompanying Lüders Instability	69
4.3	Temporal evolutions of heat power and temperature	70
4.4	Thermoelastic regime and nucleation of Lüders band	71
4.5	Growth of Lüders bands in the load plateau	72
4.6	Delayed yielding in the end of the load plateau	73
4.7	Delayed localized yielding and uniform strain hardening in region III	74
4.8	Characteristic variations of the mechanical, elastic and plastic powers	75
4.9	Characteristic variations of the overall heat, thermoelastic coupling and dissipative heat powers	76
4.10	Characteristic variations of the plastic, dissipative heat and stored powers	77
4.11	Characteristic variations of the energy conversion rate ratios	78
5.1	Radiograph of the tensile specimen welded in the center of the gauge length	82

Figure No.	Figure Caption	Page No.
5.2	Hardness across the weld	83
5.3	Optical micrographs of (a) base metal, (b) heat affected zone and (c) weld zone in the TIG welded mild steel	84
5.4	Spatiotemporal evolutions of (a) temperature and (b) heat power accompanying Lüders instability in TIG welded specimen	84
5.5	Spatial distribution of temperature and heat power accompanying Lüders band nucleation and growth	85
5.6	Spatial distribution of strain and strain rate accompanying Lüders band nucleation and growth	87
5.7	Temperature and heat power fields in the initial stages of strain hardening	88
5.8	Strain and strain rate fields in the initial stages of strain hardening	89
5.9	Temporal evolutions of (a) temperature, (b) heat power, (c) strain and (d) strain rate on the local zones	90
5.10	Variation of thermomechanical parameters in (a) zone1, (b) zone 2 and (c) zone 3	93
5.11	Variations of β_{diff} in (a) zone 1, (b) zone 2 and (c) zone 3	95

LIST OF TABLES

Table No.	Table Caption	Page No.
1.1	Variation of effective width and active zone for different specimens studied	60

LIST OF ABBREVIATIONS

IRT	Infrared thermography
DIC	Digital image correlation
IR	Infrared
PLC	Portevin-Le Chatelier
FEM	Finite element method
DP	Dual phase
IRIC	Infrared image correlation
CCD	Charge coupled device
CMOS	Semiconductor metal oxide
RMS	Root mean square
QWIP	Quantum well infrared photo detectors
SSD	Sum of squared difference
NSSD	Normalized sum of squared difference
ZNSSD	Zero normalized sum of squared difference
CC	Cross correlation
NCC	Normalized cross correlation
ZNCC	Zero normalized cross correlation
EDM	Electro discharge machining
TIG	Tungsten inert gas welding
NDE	Nondestructive evaluation

LIST OF SYMBOLS

N	Spectral radiance of the black body
h	Planck's constant
c	Velocity of light
k	Boltzmann's constant
λ	Wavelength
λ_{max}	Peak wavelength
B	Wien's displacement constant
σ_B	Stefan-Boltzmann constant
C	Correlation coefficient
$f(x, y)$	Grey value of subset in reference configuration
$f^*(x^*, y^*)$	Grey value of subset in deformed configuration
x, y	Coordinates of subset in reference configuration
x^*, y^*	Coordinates of subset in deformed configuration
$u, v \text{ and } w$	Displacements of the subset center in x, y and z directions.
$\Delta x, \Delta y$	Directional components of distance of the subset center to the considered point x, y
$\varepsilon_{xx}, \varepsilon_{yy}, \varepsilon_{xy}$	Lateral, longitudinal and shear strain
V_m	Molar volume
α	Linear thermal expansion coefficient
E	Young's Modulus
T	Absolute temperature
C_v	Specific heat at constant volume

θ	Relative temperature
e_{yy}	Longitudinal strain
σ_1	Lower yield stress
σ_2	True upper yield stress
σ	True stress
ε	True strain
ρ	Material density
q	Heat flux vector
ψ	Helmholtz free energy
α_j	Set of internal state variables
$\dot{\varepsilon}$	Strain rate
W'_{tdis}	Thermal dissipation
k	Heat conduction tensor
r_e	External heat supply
$C_{\varepsilon,\alpha}$	Specific heat capacity at constant ε and α
δ	Identity tensor
λ_c	Isotropic conduction coefficient
τ	Time characterizing heat losses
W'_{hs}	Heat power
W'_{ext}	Mechanical power
W'_s	Stored power
W'_e	Elastic power
W'_p	Plastic power
W'_{ther}	Thermoelastic coupling power
W'_{dis}	Dissipative heat power

$\dot{\sigma}$	True stress rate
$\dot{\epsilon}$	True strain rate
β_{int}	Integral Taylor-Quinney coefficient
β_{diff}	Differential Taylor-Quinney coefficient
β_1	Fraction of plastic power converted into heat power
β_2	Fraction of plastic power converted into stored power
A	Instantaneous area of cross section
A_0	Initial area of cross section

CHAPTER – 1

INTRODUCTION

1.1 Materials and Deformation

Deformation is defined as the change in shape or size of the object under the influence of load. The deformation is elastic if the change in shape induced is reversible after removal of the load. If the material is permanently deformed by breakage of bonds between the atoms it results in plastic deformation. From the forming operations to erection as structural components, materials are subjected to plastic deformations by the nature of processing. The property of final product is dependent on the intensity and conditions of plastic deformation experienced by it during forming operations. Therefore, it becomes mandatory to study the plastic flow properties of materials in order to optimize the forming processes. After erection, based on the nature of design and loading conditions the component experiences plastic deformation while in service. Failure of structural components during their service cause production loss and may even subject the human life to risk. Hence it becomes important to study and understand the underlying deformation mechanism of materials and the influence exerted by the microstructural state of the material. There are several techniques for measuring deformations and study the mechanical behavior of materials such as optical and electron microscopy, photography, extensometers, strain gauges, acoustic emission, magnetic Barkhausen noise emission and speckle interferometry etc. Each of these techniques has its own advantages and limitations with respect to characterization of spatiotemporal evolutions of deformation, magnitude of strain measurement, area of measurement and material to be studied etc.

1.2. Infrared Thermography and Digital Image Correlation

The last two decades have seen extensive developments in the imaging, nondestructive evaluation techniques, particularly in the field of infrared thermal imaging and digital image correlation. Infrared thermography (IRT) is a technique that maps the surface temperature profile of the object based on the infrared radiations emitted by it using a suitable IR imaging system. Digital Image Correlation (DIC) is an optical method that maps the surface displacement and strain during deformation by correlating the undeformed image with the deformed one through gray scale matching. A single thermogram (thermal image) provides the information on the plastic deformation zone at any particular instant whereas a strain image from image correlation holds a track record of the history of deformation till the time of investigation. Therefore, performing simultaneous characterization using IRT and DIC has an added advantage of extracting information on both instantaneous deformation and history of deformation at any particular instant. The main advantages of these techniques with respect to deformation studies are: 1. They are non invasive, non contact, fast and reliable, 2. They can be applied on engineering components, 3. They have a fairly large field of view, 4. Spatiotemporal characterization of deformations can be carried out and 4. Real time visualization of plastic strain evolutions is also possible. The limitations include thermal diffusion during deformation, which may affect the interpretation of deformation zone. On the other hand, strain resolution in DIC is relatively low.

The efficiency of IRT and DIC in characterizing the mechanical behavior of various materials subjected to tension is well documented in the literatures [1-10]. Yi et al. [1] have determined the inflection point differentiating the thermoelastic and thermoplastic effects in aluminium specimens based on IR heating and cooling emissions. Venkatraman et al. [2-3] have indicated that it is possible to predict the zone of failure

using thermal imaging much ahead of the macroscopic stress characteristics. The authors have also observed that the slope of the temperature variations drastically increase after necking in 316 stainless steels [4]. Tong et al. [5] have studied the deformation heterogeneity in Al-Mg alloys subjected to tension in the form of non-stationary deformation bands using DIC. Kutin et al. [6] have observed an increase in the temperature on the root of the butt weld joint which is subjected to high stress under tension because of its asymmetrical geometry. The local constitutive behavior of different zones of friction stir welded aluminum alloy [7], laser welded 304 L stainless steel [8] and 316 H stainless steel [9] have also been estimated using DIC. Reynolds et al. [10] have reported that in friction stir welded 5054-O Al alloy, strain initially localizes in the weld nugget and then deforms uniformly in the base metal using DIC.

Considerable work on plastic instabilities such as PLC (Portevin-Le Chatelier) effect [11-20] and stress induced martensitic phase transformation [21-24] have also been carried out using IRT/DIC techniques. Louche et al. [11] have studied the kinematics of continuously propagating type A and hopping type B PLC bands using localized heat sources in AA 5086 Al-Mg alloy. Zdunek et al. [12] have reported that the stress drop in the serrated stress-strain curve coincides with the nucleation of PLC band using strain fields in Al-4.5%Mg-0.7% Mn alloy. Chen et al. [13] have observed that PLC band strain increases and band velocity decreases with increase in strain in TWIP steel. Activation of randomly oriented type C band during stress drops [14, 15] and nucleations of type A bands on the crests of stress wave [16] have also been reported based on the kinematic fields. Ait-Amokhtar et al. [17] have proposed that the intensity of strain rate localization is more for type B bands than type A based on the temperature and stress drops measurements. Similar observations have also been made in the same material by other authors using strain fields [18-19]. PLC band characteristics studied using strain fields

from DIC have also been modeled and validated using FEM [20]. Favier et al. [21] have applied IRT and DIC to study the stress induced martensitic phase transformation in thin walled Ni-Ti shape memory tube. Daly et al. [22] have reported high stress intensity factor in the phase transformation zone near the crack tip of NiTi shape memory alloy subjected to tension. Uniform strain over the gauge length in the load plateau has also been reported in the same material under shear loading conditions [23]. The inter-martensitic transformation path in NiMnGa single crystals has been characterized using strain fields by Hamilton et al. [24].

IRT and DIC have also been used to study the energy balances during plastic deformation of various materials. Farren and Taylor [25] and Taylor and Quinney [26] have experimentally proved that during deformation a part of expended mechanical energy is dissipated as heat leading to increase in temperature of the material and the remaining energy is stored in the material as strain energy associated with dislocations, commonly called as stored energy of cold work. The integral Taylor-Quinney coefficient denoted by β_{int} represents the fraction of mechanical energy converted into heat and stored energy. The differential Taylor-Quinney coefficient denoted by β_{diff} represents the fraction of plastic work rate (plastic power) converted into heat dissipation rate (heat power) and stored energy rate (stored power). Both these coefficients have been reported as function of plastic strain and strain rate for various materials using infrared radiometry [27-34]. Rittel [35] has reported that β_{diff} can take values even greater than 1 unlike β_{int} . With the advent of focal plane array based infrared cameras and their commercial availability in the recent years, variations in both the Taylor-Quinney coefficients for various materials exhibiting local and uniform deformations have been studied [36-43]. IRT and DIC have also been coupled together to explore the local variation in the conversion of applied

mechanical power into dissipated and stored powers by making use of the information on local strain evolutions from DIC [44-47].

Thermal imaging has also been used to study the fatigue behavior of various materials and estimation of fatigue limits. Although the method of empirically relating the drastic change in the temperature regime for a particular stress range to fatigue limit was reliable for some steels [48-49], it became questionable for materials like Al alloys [50] which has high thermal diffusivity. To address this issue, the fatigue limit estimation was later carried out using heat dissipation. Boulanger et al. [51] have indicated that the decrease in dissipation in the beginning of each block associated with high stress range during fatigue test of DP (dual phase) 60 steel is because of the non-uniform heat sources. Berthel et al. [52] have reported heterogeneous distribution of dissipation till the initiation of fatigue crack in DP 600 steel. However, the dissipation intensity and thermoelastic source amplitude have been observed to increase with increase in loading frequency. Morabito et. al [53] have reported that increase in stress amplitudes makes the thermal method to estimate the fatigue limit in close agreement with the mechanical test since the signal to noise ratio of dissipation will be more. The authors have also indicated that zones of high thermoelastic source amplitudes are the potential sites of fatigue crack initiation. Chrysochoos et al. [44] have observed that deformation energy rates during high cycle fatigue of DP steel are homogeneous but heat dissipation is heterogeneous because of the formation of persistent slip bands. Pastor et al. [54] have proposed a cumulative damage indicator, defined as the temporal integral of mechanical dissipation, to study the initial damage state of the specimen based on geometrical effects before being subjected to cyclic loading. Recently, Fedorova et al. [55] have proposed a methodology to estimate the J-integral and stress intensity factor associated with fatigue crack propagation using the associated heat dissipation estimated from thermal data.

Pottier et al. [56] have proposed a motion compensation technique to track the temperature evolution of a particular material point of the object subjected to large deformations. They have also developed an algorithm to track the displacement of a spot using a sine function and represent the temperature data in the reference geometry of the specimen. Similar to this, Saai et al. [57] have synchronized the thermal and kinematic data of few material points by tracking their displacement using DIC and using them in the developed numerical synchronization process. Maynadier et al. [58] have proposed a methodology called infrared image correlation (IRIC) for the extraction of thermal and kinematic data on the same specimen surface by using only infrared measurement. It involves application of speckle pattern on a part of the specimen surface and the remaining with black paint which ensures contrasted IR images enough to perform image correlation. Then temperature measurement is performed taking into account the variation in the gray level of the speckle with temperature changes of the specimen. Bodelot et al. [59] have used a special experimental setup to extract the thermal and kinematic data on the same surface of the specimen. The setup involves a dichroic mirror placed at an angle of 45° to the specimen surface which completely transmits the IR radiation towards the IR camera placed in front of the specimen surface and deflects the visible light towards the CCD camera of DIC setup placed at an angle of 90° to the specimen surface. The authors have developed a transformation algorithm between the infrared camera coordinate system and CCD camera coordinate system by using three reference points and their displacements from DIC computation for evaluating the coefficients of the transformations [60].

1.3 Plastic instabilities

Materials such as low carbon steels, mild steels and Al-Mg alloys due to strain ageing exhibit unstable elastic-plastic transition and plastic flow commonly called as plastic instabilities which deteriorate the formability and ductility of these materials.

Instability in the plastic flow is generally characterized by the appearance/formation of deformation bands on the material surface at the macroscopic scale. These deformation bands induce surface roughness thereby affecting the surface quality of sheet metal products during metal forming operations such as deep drawing, stamping and also during loading conditions while the component is in service. Because of this, deformation bands accompanying plastic instabilities are also called as stretcher strains, Hartmann lines, flow lines, worms, and strain figures etc. Also, the induced surface roughness affects the high cycle fatigue properties of components by increasing the number of crack nucleation sites on the surface. Lüders deformation and Portevin-Le Chatelier (PLC) effect are the two instability phenomena commonly observed in such structural steels which are widely used in many industries including automobile and nuclear etc.

Lüders instability occurs because of static strain ageing involving interaction of the interstitial solute atoms with dislocations generated after initial plastic deformation resulting in locking up of dislocations. In carbon steels, carbon atoms act as solute atmospheres. On the other hand, PLC effect occurs as a result of dynamic strain ageing involving interaction between solute atoms and dislocations during plastic deformation [61]. Of these, Lüders instability is of prime concern to industrial manufacturers as the associated strain ageing generally occurs during material storage, which may lead to production loss, since maintaining surface quality is mandatory for many applications. Lüders phenomenon is characterized by discontinuous yield points in the load-elongation curve, namely upper and lower yield point, followed by a load plateau involving strain localizations in the form of deformation bands called Lüders bands [62]. Lüders band is a band (collection) of slip lines representing the localized (inhomogeneous) plastic deformation exhibited by the material. The upper yield point corresponds to the unlocking of the locked dislocations or generation of fresh dislocations and lower yield point

corresponds to the propagation of the unlocked or fresh dislocations. The collective and self-organized behavior of these dislocations manifests on the surface of the material as band front propagation (band growth). There may be one or more band nucleations depending on the stress concentration zones in the material with the formation of each band accompanied by a load drop in the load plateau. Lüders deformation is then followed by uniform strain hardening.

1.3.1 Proposed theories and experimental works on Lüders instability - International scenario

There are three major theories put forward to explain the Lüders phenomenon based on the interactions of solute atoms with the dislocations namely, 1. Grain boundary theory, 2. Cottrell's theory and 3. Johnston and Gilman theory. According to grain boundary theory [63], the deformation of grains in α -iron is resisted by a thin film of cementite [64] at the grain boundaries up to upper yield point, at which the film breaks and deformation proceeds into the grains with a reduced stress called lower yield point. During strain ageing, this film gets reformed due to diffusion of carbon atoms resulting in recurrence of the yield point phenomenon. According to Cottrell's theory [65], interstitial elements such as carbon and nitrogen in low carbon steels diffuse to the position of minimum energy, i.e. below the extra plane of atoms in a positive edge dislocation, in order to reduce the total distortion energy thereby blocking the movement of dislocations. It was proposed that upper yield point corresponds to the unlocking of the dislocations locked by solute atoms and lower yield point corresponds to their movement. Certain experimental results were expected for the validation of the Cottrell's theory. They are, 1. Elimination of upper yield point by introduction of free dislocations, 2. Independent nature of upper yield point on the grain size and 3. Appearance of upper yield point in single crystals of iron. However, the experiments reported later showed that upper yield point in

single crystals is no way comparable to that in the fine grained polycrystalline materials, yield point is sensitive to the grain size and the introduction of free dislocations did not eliminate the yield point phenomenon. Based on these observations, Sylwestrowicz et al. [66] suggested that Cottrell's theory is unlikely and number of grain boundaries play major role in the occurrence of the yield point phenomenon in mild steel. Johnston and Gilman [67] proposed that dislocations present in the materials are strongly locked and the observed upper yield point is not the stress, at which locked dislocations are unlocked, but at which new dislocations are generated and lower yield point corresponds to multiplication of dislocations. G.T. Hahn [68] proposed a model, suggesting the presence of small numbers of mobile dislocation initially in the material. Rapid multiplication of dislocations and stress dependence of dislocation velocity are proposed as the reasons for the abrupt yield drop in a material.

Although Lüders instability has been studied intensively for more than three decades, kinematics of localization accompanying Lüders deformation and the corresponding macroscopic manifestations are yet to be fully understood. The need for better understanding of the Lüders phenomenon through versatile characterization tools is in demand even today. Over the years, many techniques have been employed to study nucleation and growth behavior of Lüders bands, spatiotemporal evolutions of strain localizations and the associated macroscopic band characteristics. They are as follows:

1.3.1.1 Microscopy

The evolutions of microstrain (strain of the order of 10^{-4} - 10^{-6}) before the macroscopic yield point in metals and their localization leading to nucleation of Lüders band have been studied extensively using optical and electron microscopy. According to Cottrell [69], pre-yield microstrain below the upper yield stress is caused by dislocations breaking from the impurity atmospheres (carbon, nitrogen) in the vicinity of stress

concentrators resulting in pileup of dislocations on the grain boundaries. Suits et al. [70] and Rosenberg [71] have observed the cluster of yielded grains with slip bands over the complete cross section in fine grained silicon iron before the upper yield point representing the formation of Lüders band using etch pitting. P.J. Petch [72] has proved through his model that only at upper yield stress slip band penetrates the grain boundary, what is called as slip breakthrough. But for intermediate grain sizes, slip line crossing a grain boundary before upper yield point [73] and sometimes less than the lower yield point for fine grained material [74] have also been reported. Moon et al. [75] and Worthington et al. [76] based on their observations have proposed that grain boundaries are the sources of stress concentration from which slip bands are formed. Carrington et al. [77] have observed that slip lines are present in more than one direction behind the band front, whereas at the band front only parallel slip lines are present. The same has also been observed using transmission electron microscopy [78]. Based on the electron microscopy observations in silver, Bonfield et al. [79] have proposed that dislocation substructure within the grains attained through various annealing treatments contribute more to the observed preyield behavior than the pile ups in grain boundaries. Ananthan et al. [80-81] have observed the presence of microscopic shear bands propagating in random crystallographic orientations ahead of the Lüders band front in polycrystalline mild steels. Kink angle at the band front has also been reported to decrease with increase in grain size of the material [82].

1.3.1.2 Photography

Studies carried out using photography have primarily focused on studying the macroscopic Lüders band characteristics such as physical form of the band, band front orientation and velocity etc. According to Lomer's [83] observation, heavy, stiff specimens produce complex bands and light, flexible specimens produce planar bands

while yielding. It has been reported that when grain size of the material is increased diffuse bands are produced [84]. Butler [85] has observed the increase in front velocity with increase in grain size. Ananthan et al. [86] have observed that increasing strain rate results in complex bands even with slender specimen. Also, the band front angle was reported to vary from 45° for fine grained to 70° for coarse grained specimen. Cross section of the specimen has also been observed to influence the angle of the band front [87]. Lüders band front velocity has been found to increase with increase in strain rate [88]. The power law dependence of the Lüders band velocity on stress has also been reported by few authors [89-90]. Fujita et al. [91] have observed an increase in magnitude of deformation by Lüders band front propagation with increase in strain rate during stress relaxation. Miyazaki et al. [92] have reported that spring constant of the testing system does not affect the band formation process, but its front propagation along the specimen axis. Prewo et al. [93] have estimated the effective stress required for propagation of Lüders band front during stress relaxation using photography.

1.3.1.3 Strain gauges and Extensometers

In low carbon steel, pre-yield microstrain is reported to be of the order of 30×10^{-6} and 140×10^{-6} in iron with 3% Si [94] using strain gauges. Based on the experimental investigation in iron, Brown et al. [95] have proved that pre-yield microstrain increases with increase in grain size (D) as D^3 . B. L. Shaw et al. [96] have reported that the number of dislocations available for flow before macroscopic yield point is a function of loading rate. Lining et al [97] have experimentally verified that microstress increases during the initial stage of microstrain, because of depletion of free dislocations and in later stages increases with generation of new dislocations. Lüders strain has been reported to increase with increase in strain rate, decrease in grain size, increase in yield drop and decrease in temperature using strain gauges [88, 98]. Empirical equations relating Lüders stress,

Lüders strain and front velocity have also been developed by some authors [85, 99]. Ananthan and Hall [86] have demonstrated the increase in shear and flow components of Lüders strain with decrease in grain size, in both rectangular and hexagonal cross-sectional specimens. Zhang et al. [100-101] have reported the occurrence of continuation of strain localization after Lüders band front propagation at the end of the load plateau and initial stages of work hardening using strain gauges arranged in longitudinal and shear (45°) fashion in AISI 1045 steel. Inhomogeneity in strain distribution across the band front was first proposed by Van Rooyen [102] based on the observations using extensometer. Later, it was also studied by other authors using strain gauges and clip gauge extensometers [103-105]. Strain has been reported to increase from the band front and saturate within the band with the plastic flow through creep deformation under constant stress [106].

1.3.1.4 Acoustic emission

Acoustic emission has been primarily employed to relate the macroscopic stress-strain response to the microscopic dislocation activities associated with Lüders instability. Scruby et al. [107] have observed that each load drop is accompanied by a significant burst of acoustic emission in Al-Mg alloy. With increase in impurity concentration, the RMS voltage has been reported to decrease due to grain refinement which in turn resists the motion of dislocations [108]. It has been shown that maximum acoustic emission energy is observed during the yield drop, whereas during the band front propagation it is relatively less. Power spectral density has been reported to shift towards lower frequency with increase in emission energy [109]. Muravev et al. [110] have estimated the velocity of the Lüders band front based on the time difference in the evolution of signal in various sensors fixed along the specimen. Han et al. [111] have observed two types of acoustic emissions; namely, burst type in the load plateau involving Lüders band growth and continuous type in the stress levels close to yield point and strain hardening region. It was

also found that acoustic energy of notched specimens is more than that of the unnotched ones. Shibkov et al. [112] have proposed that the first acoustic pulse is the precursor of the loss of deformation stability, which is associated with the nucleation of Lüders band.

1.3.1.5 Magnetic Barkhausen noise and Flux leakage

Campos et al. [113] have studied the localized deformations accompanying Lüders bands in ANSI 1050 steel and observed that for samples cut in the transverse direction no MBN energy is observed confirming that no bands evolve. The angular dependency of the MBN energy on the applied stress in revealing the plastic deformation zone of Lüders bands has also studied [114]. Using magnetic flux leakage technique, it has been reported that leakage flux emanates from one edge of the band and end at the other edge due to decrease of magnetic permeability of the deformed region thereby revealing the zone of Lüders band [115]. Stupakov et al. [116] have observed the magnetic anisotropic behavior in carbon steel induced by deformation associated with the Lüders bands. The region of Lüders band was identified by the change in the RMS value of Barkhausen noise.

1.3.1.6 Speckle pattern interferometry

Similar to photography, speckle interferometry has also been primarily employed to study the macroscopic Lüders band characteristics. Yoshida et al. [117] have estimated the Lüders band velocity in structural steel using specklegrams. The authors were able to identify the band nucleation zone much before the digital image captured using CCD camera. Guelorget et al. [118] have observed the decrease in strain localization band width with increase in strain. However, the authors have reported that it increases to five times the shear band width before fracture. Using laser speckle interferometry, it is also reported that with increase in ageing time, band multiplicity increases and band characteristic such as width, orientation and angle are not much affected [119].

1.3.1.7 Studies on Lüders deformation using IRT and DIC

A detailed review of literature reveals that significant works have been carried out in studying Lüders instability on various materials using IRT and DIC. One of the earliest works in this domain is by Louche et al. [120] on European grade steel S355MC. The authors have deduced the dissipative heat sources associated with Lüders band front propagation from the heat diffusion equation to estimate the band front velocity and orientation. The band front orientation and velocity are reported as $70 \pm 5^\circ$ and 1 ± 0.1 mm/sec respectively. Wattrisse et al. [121] have worked on image processing based on digital image correlation for studying Lüders band propagation, necking and the effect of pre-strain on SOLDUR 355 and HR55 steels using lateral, longitudinal and shear strain fields. The band orientation measured (70°) was reported to be in agreement with the measurement made on polished specimen. Lukin et al. [122] have mapped the nucleation of Lüders bands from a circular hole (stress concentrator) using thermal imaging in 18G2S steel. Similar to this, Moiseichik [123] has reported in low carbon steel that heat is not generated in the whole of the plastic deformation zone near the crack tip but in the Lüders band which occupies small part of this zone. For notched specimens, bands have been observed to develop in the plane of maximum shear stress.

Dumoulin et al. [124] have studied the variation of the fraction of plastic power dissipated as heat and stored power during Lüders deformation in Weldox series high strength, high ductility steels. Fraction of heat dissipated has been reported to continuously decrease with increase in plastic strain. Using dissipative heat source, Willink et al. [125] have observed that 0.3% temper rolled carbon steels never develops Lüders bands when subjected to loading. Nogueira De Codes et al. [126] have applied IRT and DIC simultaneously to study the spatiotemporal evolution of Lüders and PLC bands in Al-Mg alloy AA5182. The authors have observed the nucleation of PLC bands at the end of the

load plateau with jerky stress flow all along the load plateau to strain hardening representing the absence of critical strain for nucleation of PLC bands. X. Feng et al. [127] have observed that at low strains PLC bands nucleate on the trailing edge of the Lüders bands which is not accompanied by a load plateau in Al alloy AA5754. Very recently, Coer et al. [128] have applied DIC to study the kinematics of Lüders band in Al-3%Mg alloy subjected to shear stress state using shear strain and shear strain rate fields. The authors have observed the increase in band width and front velocity with increase in crosshead speed. The effect of stress concentrators such as sharp and blunt notches on the Lüders yielding behavior and the associated plasticity development in regions of stress concentrations have been studied experimentally and modeled by Beardsmore et al. [129]. It has been reported that in sharp notched specimens plastic zone is more constrained and stress intensification is higher in the presence of Lüders behavior. However, all these works have primarily focused on determining Lüders band characteristics such as band front velocity, band width, band front orientation and propagation behavior.

1.4 Motivation for the study

Lüders deformation has been an interesting and intriguing phenomenon in itself as can be seen by the number of works that have been published internationally. At this stage, the author is reminded of a quote by Charles Morgan “As knowledge increases, wonder deepens”. Review of literature and analysis of the results reported on Lüders deformation apart from widening the knowledge in it also raises a lot of inquisitive queries indicating that there are grey areas which are not fully explored and need further investigation. Some of these areas include evolutions of pre-yield microstrain and its influence on Lüders band nucleation, band formation and growth mechanism, stress-strain-strain rate distributions across the band front, delayed localized yielding and the influence of dissimilar microstructures and the associated stress concentrations on the Lüders yielding behavior of

welded material etc. Hitherto, both conventional and advanced imaging techniques have been primarily applied to study the macroscopic Lüders band characteristics such as band front velocity, band width, band front orientation and the propagation behavior. Conventional techniques have their own limitations in characterizing and visualizing the strain localizations, which is crucial to gain insights into the Lüders yielding behavior. Application of IRT and DIC, which can provide quantitative information on the spatiotemporal evolutions of strain localization accompanying Lüders band nucleation and growth, would lead to an enhanced understanding in the areas lacking understanding.

However, the thermal diffusion in the temperature field and the effect of track record of strain in the DIC strain field have to be overcome for quantitative analysis of the spatiotemporal evolutions of strain localization in the material. The heat losses due to thermal diffusion, which blur the manifestation of strain localizations in the thermogram can be overcome by addressing the deformations using heat dissipation as it is inherent to the plastic deformation of materials. On the other hand, the effect of track record of strain in the DIC strain field to reveal strain evolutions of lower magnitude can be overcome by addressing the kinematics of localization using strain rate maps. Also, a study on the fractional dissociation of acting plastic power into stored and dissipated powers would help in understanding the thermomechanical couplings underlying the nucleation and growth of Lüders bands and predicting the associated hardening/softening behavior in both plain and welded steels.

Among the steels which undergo Lüders instability, IS 2062 grade E250 B mild steel is preferred as primary structural material in various industries because of its excellent ductility, malleability and weldability. Also, this steel is used in bridges, buildings, durable storage containers, pressurized storage tanks, gears, shafts, etc. Among these applications, there are some surface critical applications of this steel which need

good and sustained surface finish, particularly the structural products of automobile industries. Therefore, application of IRT and DIC techniques for studying the Lüders deformation behavior in this steel would generate a knowledge base not only for the companies involved in metal forming operations, but also for the industries employed with structural components made of this steel.

1.5 Objectives and Significance of the work

In this thesis, the Lüders instability phenomenon is investigated in IS 2062 grade E250 B mild steel by combined application of IRT and DIC techniques for the first time. The emphasis is primarily on the areas that had earlier lacked understanding such as microstrain localization leading to Lüders band nucleation and the associated band formation behavior, deformations in the local zones within the Lüders band which constitutes to the band growth, stress-strain-strain rate distribution across the band front and the occurrence of delayed localized during uniform strain hardening etc. Macroscopic observations in all these areas are correlated to microscopic events established based on experiments and proposed models. This is one of the major highlights of this dissertation. It also focuses on the estimation of heat power and strain rate evolutions accompanying Lüders band nucleation and growth for quantitative analysis of the kinematics of localization without the influence of signatures of prior plastic deformation. The other important objective of this work is to study the difference in fractional dissociation of plastic power during Lüders band kinematics in the load plateau and uniform strain hardening through estimation of dissipative heat and stored powers, which again is unique to this dissertation. This would help in understanding the hardening/softening behavior of the material during nucleation and growth of Lüders bands. This thesis also aims to study the influence of dissimilar microstructures and the associated stress concentrations on the nucleation and growth behavior of Lüders bands in welded mild steel. The focus is on the

estimation of thermomechanical parameters and differential Taylor-Quinney coefficient in various local zones which would quantify the strain localization behavior observed using thermal, heat power, strain and strain rate fields. This attempt is again a first of its kind.

1.6 Outline of the dissertation

This dissertation is structured as follows. Chapter 2 dwells on the principle, theoretical background, advantages and disadvantages of the infrared thermal imaging and digital image correlation techniques. It also describes the importance of the chosen material for study, experimental setup and methodology adopted to perform the full field measurements of the deformation. In chapter 3, Lüders band nucleation and growth kinematics are studied based on the associated thermal and strain evolutions. The evolutions of microstrain and their localization leading to Lüders band formation, stress-strain-strain rate distribution across the Lüders band, nucleation and growth behavior of Lüders band, kinematics of localization accompanying the band front propagation etc., are discussed. The results obtained in all these areas are also compared with the proposed models and established concepts taking into account the limitations of the techniques employed. Chapter 4 highlights the advantages of studying the Lüders phenomenon based on the heat power and strain rate evolutions without the influence of signatures of prior plastic localizations. The kinematics of localization and the difference in magnitude of deformation during growth of different bands is also quantitatively studied based on the variations of plastic, dissipative heat and stored powers. The difference in the rate of energy conversions during strain localizations in the load plateau and uniform strain hardening is also addressed through the estimation of energy conversion rate ratio (β_{diff} - differential Taylor-Quinney coefficient). In Chapter 5, the influence of dissimilar microstructures and the associated stress concentrations on the deformation behavior of welded mild steel during Lüders band kinematics and uniform strain hardening is studied

based on the associated thermomechanical couplings. The fractional conversion of plastic power in the local zones of welded mild steel with dissimilar mechanical properties is also discussed using the energy conversion rate ratio. Chapter 6 concludes the thesis highlighting the significant outcome of the work carried out (contributions) and discusses the scope for further investigation.

CHAPTER – 2

INFRARED THERMAL IMAGING AND DIGITAL IMAGE CORRELATION: THEORY AND EXPERIMENTAL APPROACH

In this chapter a detailed discussion on the principle, theory, advantages and limitations of experimental techniques employed such as IRT and DIC are discussed. The experimental setup and procedure adopted to study the inhomogeneous plastic deformation behavior are explained in detail. The parameters used with the testing machine, imaging systems and associated post processing procedures are outlined. The importance and need for studies on the Lüders instability behavior in IS 2062 grade E250 B mild steel based on its applications are also highlighted.

2.1 Infrared thermal imaging

Infrared thermal imaging or infrared thermography (IRT) is a nondestructive, noninvasive and non contact method in which the surface temperature distribution of the object is imaged based on the IR radiations emitted by it using a suitable IR imaging system. Any object above zero Kelvin (absolute zero) emits electromagnetic radiations (associated with molecular motions). If the temperature of the object is at and/or above room temperature, the emitted radiations fall predominantly in the infrared band of the electromagnetic spectrum. Using an appropriate IR detector, the radiations can be converted into suitable electrical signals, processed and displayed on a monitor as a grey level or RGB image in which each grey level or hue represents a temperature range. Nondestructive testing, condition monitoring, gas detection, automation, medical diagnostics and security are the major fields of application of this technique.

2.1.1 Infrared imaging system

Infrared camera consists of three major elements, namely, optical system consisting of lenses, detector and cooling system. The optical lens focuses the infrared radiations reaching the camera on to the detector which in turn generates an electrical signal proportional to the intensity of radiation. Since certain materials are opaque or partially transparent to infrared rays, lens materials commonly used for converging light cannot be used for IR radiations. Therefore, materials such as quartz, CaF_2 , Ge, and Si which are infrared transparent are generally used according to the wavelengths. Since the object to be studied is placed at a distance from the infrared camera, infrared radiations are likely to be absorbed by the atmospheric constituents such as water vapor and natural gases (e.g. CO, CO_2 , NO and CH_4 etc) in the intervening medium [130]. While this is not of concern in laboratory experiments where distances are small, this factor needs to be accounted in field applications such as monitoring of electrical transmission lines and mechanical installations etc.

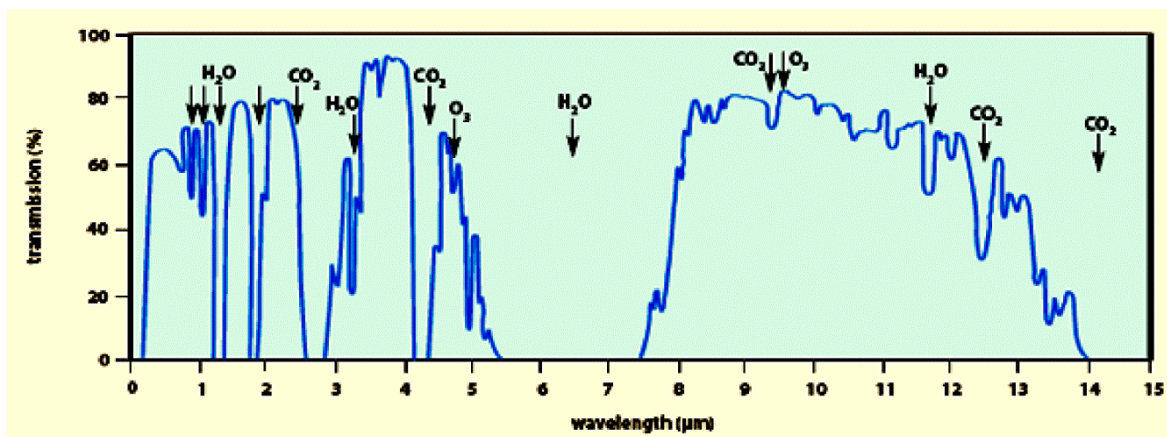


Figure 2.1 Atmospheric transmission spectrum of infrared radiation [131]

Figure 2.1 depicts the IR transmittance of the atmosphere. It can be observed that there are strong absorptions in the wavelength range of 5.5 - 7.5 μm , because the corresponding frequency range matches with the natural vibrating frequencies of gas

molecules in the atmosphere. It is for this reason; infrared detectors are designed to work typically in the wavelength range of 3-5 μm (mid wave infrared) and 8-14 μm (long wave infrared), where the infrared transmittance is maximum.

2.1.1.1 Detectors

Detector is the heart of the infrared camera. The quality of the detector determines the efficiency with which temperature profiles can be mapped with sensitivity. Detectors are generally classified as thermal detectors and photon detectors.

Thermal detectors

Thermal detectors work on the principle of change in any physical properties like electrical resistance due to temperature rise as a result of incident radiation. They in general have a flat spectral response. Some important thermal detectors are explained below.

Bolometer: Bolometer is a thermal infrared detector with a very high temperature coefficient of resistance and less heat capacity. Hence, when radiation is incident on the absorber material, temperature increases and a large change in resistance is produced as a result of increase in kinetic energy of the free electrons. Bolometers are not self-powered, unlike thermocouples and hence need an external power supply to have a reference voltage. Vanadium oxide and amorphous silicon are examples of bolometer detectors. Inspection/maintenance, medical, remote sensing and fire fighting are the major fields of application of this detector.

Pyroelectric detectors: Pyroelectric detectors work on the principle of pyroelectric effect, according to which, when a pyroelectric crystal (which has spontaneous polarization at a particular temperature) is heated, the orientation of the electric dipoles changes resulting in an imbalance in the charges between the two larger sides of the crystal. This imbalance is

removed by flow of charges through the electrodes on the surface of the detector with load resistors, thereby generating a voltage proportional to the incident energy. Pyroelectric detectors have flat response ranging from UV to the microwave region with good detectivity. Lithium tantalate (LiTaO_3) and triglycine sulphate (TGS) are examples of pyroelectric detectors. These detectors are commonly used in security devices, computers and web cameras.

Photon detectors

In photon detectors, a change in the charge carrier concentration of the material is introduced as a result of incident infrared radiations, thereby changing the electrical properties like electrical conductivity. These detectors have high thermal sensitivity and short response time. There are different types of photon detectors as follows.

Photovoltaic detectors: Photovoltaic detectors work on the principle of photovoltaic effect, according to which, when a semiconductor is exposed to radiation, electron hole pair is produced. The internal electric field (built in potential) at the p-n junction separates the electron-hole pair and moves the electron into the n-type region and the hole into the p-type region resulting in an open circuit voltage which can be measured externally. The main advantage of this detector is that the voltage generated can be measured without any bias voltage or load resistor. Mercury cadmium telluride (HgCdTe), Indium arsenide (InAs), Indium antimonide (InSb) and platinum silicide (PtSi) are the examples of photovoltaic detectors. These detectors are commonly employed for Infrared measurement, heterodyne filtering and metrology applications.

Photoconductive detectors: This type of detector works on the basis of photoconductive effect, according to which, when photons incident the semiconductor (p-n junction under reverse bias condition), there will be an increase in the number of electrons or holes

(deviation from the equilibrium concentration) and hence its electrical conductivity increases. Therefore, if a load resistor is connected in series across the detector with a bias voltage, any voltage drop across the resistor will be due to change in electrical conductivity which in turn is due to incident radiation. Lead sulphide (PbS) and lead selenide (PbSe) are the examples of photoconductive detectors. Photoconductive detectors are commonly used in thermal imaging, laser beam diagnostics and spectroscopy.

Photoemissive detector or Schottky barrier detectors: Photoemissive detectors work on the basis of photoemissive effect, according to which, when a light of wavelength greater than the cut-off wavelength incidents a photocathode, it emits photoelectrons. In these detectors, a semiconductor (e.g. silicon) is laid over a metallic compound (e.g. platinum silicide) and hence when a photon incidents, it bounces an electron or hole out of the metallic compound into the semiconductor. The Schottky barrier is nothing but the electron or hole barrier created between the metal and semiconductor under equilibrium conditions due to distribution of electric dipoles. Schottky barrier detectors are commonly used in electronics industry as diode rectifiers.

Quantum well infrared photo detectors (QWIP): A quantum well is nothing but a potential well with discrete values of energy, which are generally formed by sandwiching a semiconductor material between two materials that have wider band gap. Here, the added impurities (dopants) are concentrated in microscopic regions, creating quantum wells, thereby altering the band structure. When photons incident the detector, it removes an electron or hole out of the quantum well and places in the neighboring band generating an electrical signal. For example, gallium arsenide sandwiched between layers of aluminium arsenide forms a quantum well. QWIPs are generally employed for space borne applications such as monitoring the atmospheric temperature and relative humidity profiles, cloud characteristics and the distribution of minor constituents in the atmosphere.

2.1.1.2 Cooling systems

To limit the noise induced in the measurement by heating of the detector the following cooling methods are employed. Cryogenic cooling uses a liquefied gas (e.g. H₂, N₂ and He) stored in a dewar vessel attached to the detector. Closed Stirling cooling, yet another effective method, involves repetitive expansion and compression of gas (nitrogen or argon) by a piston. Thermoelectric cooling based on Peltier effect which involves generation of cooling through flow of current from one side of the Peltier element to other side is also employed. Thermoelectric devices do not generate any vibrations and hence suitable for thermal detectors. On the other hand, photon detectors need to be cooled to less than 77 K and hence can be cooled only through thermodynamic cycle such as Stirling cooling. In general, Stirling cooling system is the most widely used method for cooling infrared detectors because of the lower temperature that can be attained with its reduced size and weight.

2.1.2 Advantages of IR imaging

1. Non contact, fast and reliable
2. Full field vision of temperature profiles
3. Dynamic thermal transients over a wide range of temperatures can be measured and hence suitable for online condition monitoring of structural components
4. Can be employed to measure/observe areas inaccessible for other techniques

2.1.3 Disadvantage

Thermal losses (due to conduction, convection and radiation) can induce spurious thermal contrast thereby affecting the reliability of the interpretation of thermogram.

2.2 Approaches in Infrared thermography

There are two basic approaches in this technique, namely, 1. Passive thermography and 2. Active thermography [132]. Passive thermography involves imaging the object surface based on natural thermal contrast in it. In active thermography, an external heat stimulus is fed into the object to generate a thermal contrast, after which its thermal distributions are imaged. All major applications of infrared thermography are basically on a passive approach. According to the first law of thermodynamics and law of entropy, heat is released by any process consuming energy. Likewise, during deformation of materials a part of the expended mechanical energy is dissipated as heat. Heat evolutions cause temperature variations on the surface of the material. Using this information on the temperature variation associated with the deformation of materials, infrared thermal imaging on a passive approach has been a proven, indispensable experimental tool over the years for studying the plastic flow behavior and fracture properties of materials.

2.3 Theory of IR imaging

The basic laws of radiation which govern the relationship between the spectral radiance and temperature are explained as follows. The spectral radiance (power radiated) of a black body in thermal equilibrium at a temperature T per unit surface area per unit of solid angle is defined by Planck's law as

$$N_{\lambda}(T) = \frac{2hc^2}{\lambda^5 \exp\left(\frac{hc}{\lambda kT} - 1\right)} \quad - (2.1)$$

where, N is the spectral radiance of the black body in $\text{W m}^{-2} \mu\text{m}^{-1} \text{sr}^{-1}$, h the Planck's constant ($= 6.626 \times 10^{-34} \text{ J s}$), c the velocity of light ($= 3 \times 10^8 \text{ m/s}$), k the Boltzmann constant ($= 1.381 \times 10^{-23} \text{ J/K}$), λ the wavelength of the emitted radiation. Fig. 2.2 shows the characteristic variation of the spectral radiance of a black body at various

temperatures. Planck's law signifies that the peak emission corresponds to a particular wavelength.

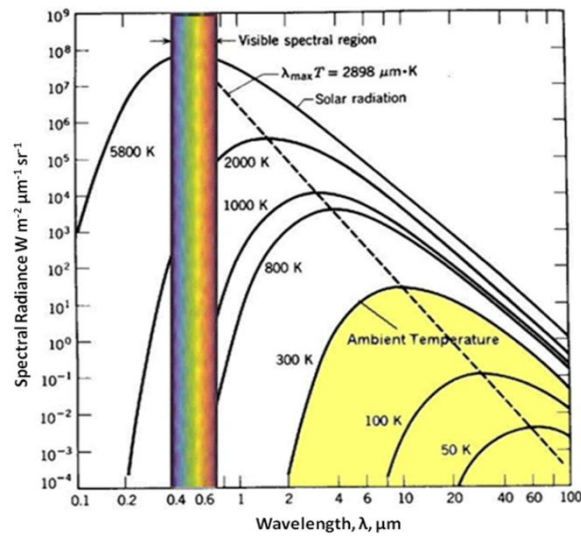


Figure 2.2 Spectral radiance of a black body [133]

It can also be observed that with increase in temperature, the peak emission shifts towards shorter wavelength. Wien's displacement law defines this inverse relation between the wavelength and the peak emission or maximum spectral radiance through the trace of the locus of maximum spectral radiance as

$$\lambda_{max} = \frac{B}{T} \quad - (2.2)$$

where, λ_{max} is the peak wavelength and B the Wien's displacement constant ($= 2897.7 \mu\text{m K}$).

The total radiant power (radiant power for all wavelengths) from the surface of a black body at temperature T is defined by Stefan-Boltzmann law through the integration of Planck's law for the complete range of wavelengths ($0 \leq \lambda \leq \infty$) as

$$M = \sigma_B T^4 \quad - (2.3)$$

Where σ_B is the Stefan-Boltzmann constant ($= 5.67 \times 10^{-8} \text{ W m}^{-2} \text{ K}^{-4}$). Eq. (2.3) indicates that hotter is the object more the infrared radiation it emits.

2.4 Digital image correlation

Digital image correlation (DIC) is an optical technique that correlates two images (deformed and undeformed) based on the grey value matching of small neighborhoods called subsets to measure the surface displacement and strain. Typical size of the subset is of the order of 20 x 20 or 30 x 30 pixels. The probe used to trace the displacement in this technique is the random dot pattern which is nothing but the random distribution of black dots on a contrasting white background or vice versa applied to the specimen surface. This pattern ensures random intensity distribution on the specimen surface when illuminated. However, the intensity of light reflected from a particular subset becomes unique to it even when it is subjected to displacement under loading. For each unique intensity level, a grey value is assigned through which displacement of a subset is identified in the deformed configuration. Typically for an 8 bit resolution camera, grey values range from 0 - 255, with the lowest value 0 representing black, highest value 255 representing white and any value in between represents different shades of grey. In cameras with 10 bit and 12 bit intensity resolution, digitized intensity (grey) values in the range of 0 - 1024 and 0 - 4096 respectively are achievable [134]. Therefore, it is worth mentioning that random dot pattern is the carrier of displacement information in image correlation.

2.4.1 Theory of DIC

Determination of displacement and strain using image correlation involves two steps of procedure namely, 1. Simple search procedure and 2. Iterative procedure [135]. In simple search procedure the displacement of the chosen subset in the reference image is determined by comparison of its grey value (intensity) to the grey values of all subsets in deformed image. Deformation of the object may introduce non integer displacements of subsets in the deformed image. Therefore, in order to achieve sub pixel displacement

accuracy, discrete intensity pattern recorded for each deformed image is converted into continuous intensity pattern (grey values) over the entire image plane using suitable interpolation schemes such as bilinear, bicubic and B-spline interpolations.

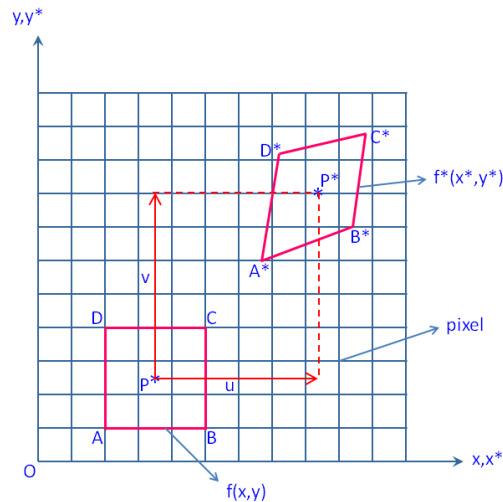


Figure 2.3 Displacement field $u(x, y)$ and $v(x, y)$ between initial image and a deformed image [135]

The grey value matching is then carried out by using suitable correlation coefficients such as sum of squared difference (SSD), normalized sum of squared difference (NSSD), zero normalized sum of squared difference (ZNSSD), cross correlation (CC), normalized cross correlation (NCC) and zero normalized cross correlation (ZNCC) etc., [136]. The most commonly used correlation coefficient is the normalized sum of squared differences given by:

$$C = \sum \left[\frac{f(x, y)}{\sqrt{[f(x, y)]^2}} - \frac{f^*(x^*, y^*)}{\sqrt{[f^*(x^*, y^*)]^2}} \right]^2 \quad - (2.4)$$

Here, $f(x, y)$ and $f^*(x^*, y^*)$ represent the grey value of the chosen subset in the undeformed and deformed images respectively as seen in Fig. 2.3, x and y are the coordinates of a point on the chosen subset in the undeformed image and x^* and y^* are their homologous in the deformed image. If $C = 0$, it means perfect correlation is achieved and any value in between 0 to 1 represents imperfect correlation.

The coordinates x^* and y^* in the deformed image are related to coordinates x and y in the undeformed image by:

$$\begin{aligned} x^* &= x + u + \frac{\partial u}{\partial x} \Delta x + \frac{\partial u}{\partial y} \Delta y, \\ y^* &= y + v + \frac{\partial v}{\partial x} \Delta x + \frac{\partial v}{\partial y} \Delta y \end{aligned} \quad - (2.5)$$

where, u and v are the displacements of the subset center in x and y directions, Δx and Δy are the x and y directional components of the distance of center of the subset to the considered point x, y . The displacement gradients, $\frac{\partial u}{\partial x}, \frac{\partial u}{\partial y}, \frac{\partial v}{\partial x}$ and $\frac{\partial v}{\partial y}$ provide information about the expansion, contraction and shear of the subset. The correlation coefficient is therefore a function of displacement components and displacement gradients. In 2D DIC, the correlation coefficient is a function of six independent variables, namely, $u, v, \frac{\partial u}{\partial x}, \frac{\partial u}{\partial y}, \frac{\partial v}{\partial x}$ and $\frac{\partial v}{\partial y}$. The displacement is determined by minimizing the correlation coefficient C . With this process, displacements are estimated with an accuracy of ± 0.5 to 1 pixel. Accurate displacement of subsets in the subpixel range is obtained by the following the iterative procedure.

The iterative procedure involves computation of rotations and strains in addition to the displacements. In the first iteration, the approximate displacement value obtained using simple search procedure is considered as the initial value of displacement of each deformation pattern (square zone) centered at subset element points namely A, B, C and D as seen in Fig. 2.4. The correlation procedure described earlier is carried out in the pattern A initially. The point A_0^* is not the actual representative of A in the deformed image. The optimal position $x_{A_1^*}, y_{A_1^*}$ of the deformed pattern is the one that minimizes the correlation coefficient. This is achieved after a certain number of iterations when a stable value of displacement from one step to another is obtained.

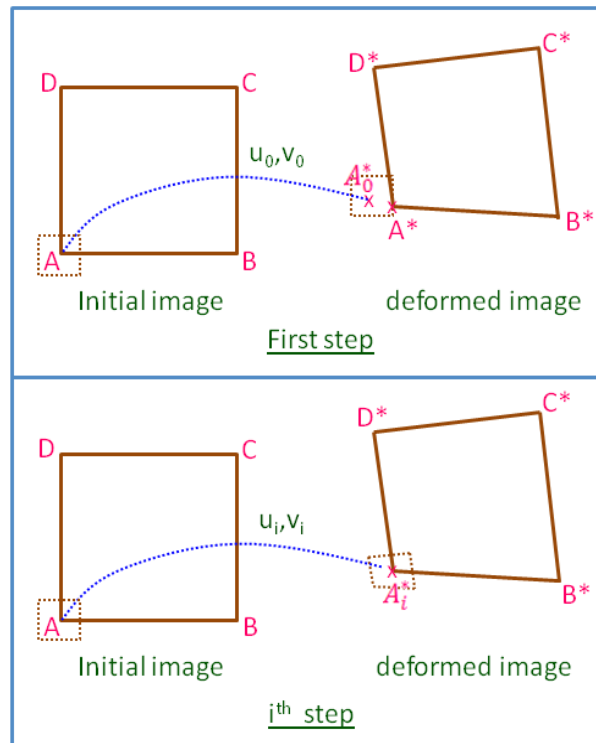


Figure 2.4 Iterative procedure to obtain precise displacement field [137]

The procedure is then carried out for other patterns, namely, B, C and D. The new coordinates A_1^* , B_1^* , C_1^* and D_1^* of the subset will be close to the real displacement value. For the next iteration of the subset, the displacement value obtained is used as an initial value. The procedure is repeated until stable displacement field of the subset is obtained which is the real displacement. This displacement is used as the first approximate displacement of the next subset. The procedure is then followed for all other subsets. Since displacements and their gradients are considered as independent variables in the iterative procedure, displacement accuracy of about ± 0.01 pixels and strain accuracy of $\pm 100 \mu\epsilon$ can be achieved, provided a good estimate of the initial value is given.

The convergence of the calculation process and the accuracy of the measured result depend mainly on the iterative method used. Iteration is generally performed using methods such as steepest descent, Newton-Raphson or a combined approach like Levenberg-Marquardt. In 3D DIC involving stereo vision, apart from in plane

displacement and strain, out of plane displacement (w) and strain $\left(\frac{\partial w}{\partial x}, \frac{\partial w}{\partial y} \text{ and } \frac{\partial w}{\partial x}\right)$ are also estimated. Hence, for all the following 12 variables, correlation coefficient has to be minimized to find the displacements [135].

$$W_{3D} = \left(u, v, w, \frac{\partial u}{\partial x}, \frac{\partial u}{\partial y}, \frac{\partial u}{\partial w}, \frac{\partial v}{\partial x}, \frac{\partial v}{\partial y}, \frac{\partial v}{\partial w}, \frac{\partial w}{\partial x}, \frac{\partial w}{\partial y}, \frac{\partial w}{\partial x}\right) \quad - (2.6)$$

The strain fields are calculated through derivatives of displacement using following Lagrangian formulations,

$$\begin{aligned} \varepsilon_{xx} &= \frac{\partial u}{\partial x} + \frac{1}{2} \left[\left(\frac{\partial u}{\partial x} \right)^2 + \left(\frac{\partial v}{\partial x} \right)^2 \right] \\ \varepsilon_{yy} &= \frac{\partial v}{\partial y} + \frac{1}{2} \left[\left(\frac{\partial u}{\partial y} \right)^2 + \left(\frac{\partial v}{\partial y} \right)^2 \right] \\ \varepsilon_{xy} &= \frac{1}{2} \left(\frac{\partial u}{\partial y} + \frac{\partial v}{\partial x} \right) + \frac{1}{2} \left[\frac{\partial u}{\partial x} \frac{\partial u}{\partial y} + \frac{\partial v}{\partial x} \frac{\partial v}{\partial y} \right] \text{ or} \\ &= \frac{1}{2} \left(\frac{\partial u}{\partial y} + \frac{\partial v}{\partial x} \right) + \frac{1}{2} \left[\frac{\partial^2 u}{\partial x \partial y} + \frac{\partial^2 v}{\partial x \partial y} \right] \quad - (2.7) \end{aligned}$$

where, ε_{xx} , ε_{yy} and ε_{xy} represent lateral, longitudinal and shear strains respectively.

2.4.2 Practical considerations for minimization of errors in 2D DIC

1. The specimen surface must be flat and parallel to the sensor plane. This is because, existence of non-parallelism would introduce out of plane displacements leading to change in magnification of the recorded images thereby introducing additional in plane displacements.
2. Fluctuations in the illumination should be avoided as it will introduce errors in the intensity values registered.
3. Increased contrast of the random dot pattern is recommended as this will help in choosing a smaller subset, which in turn increases the spatial resolution of the strain measurement.

2.4.3 Advantages of DIC

1. Simple experimental setup.
2. Does not need specimen preparation if the specimen naturally has random grey intensity distribution or it can be artificially created using paint.
3. Micro to nanoscale deformation measurements can be performed using DIC by coupling it with optical microscope, laser scanning confocal microscope, scanning electron microscope, atomic force microscope, and scanning tunneling microscope.

2.4.4 Disadvantage

Accuracy of strain measurement is comparatively low.

2.5 Thermal and optical imaging systems used in the present study

The focal plane array based infrared camera used in the present study is Cedip Silver 420 with 320 x 256 detector elements. The pixel size is 25 μm x 25 μm with pitch as 30 x 30 μm . This camera has Indium antimonide (InSb) photovoltaic semiconductor detector with spectral sensitivity in the mid infrared range of 3.6 -5.1 μm . The detector is cooled through internal closed Stirling cooling system which leads to 25 mK thermal sensitivity. The incoming IR radiations are focused onto the detector using a germanium lens. The maximum frame rate achievable with this system at full window size is 176 Hz, which can be varied in steps of 1 Hz. The integration time of this camera can be varied from 3 μs to 20 ms in steps of 1 μs . A CMOS digital fire wire camera, Marlin - F131 with 1380 x 1035 pixel elements is used for optical imaging associated with digital image correlation system. The pixel size is 6.7 μm x 6.7 μm . The maximum frame rate achievable is 25 Hz at full window size which can be varied in steps of 1 Hz. The camera operates at 10 bit mode with a shutter speed of 10 μs . With high contrast speckle pattern,

and uniform illumination throughout the test, a displacement resolution of 0.01 pixels and strain accuracy of $\pm 100 \mu\epsilon$ can be achieved.

2.6 Material and Qualification

The material used in this study is prepared from as received IS 2062 grade-E250 B mild steel sheet with the chemical composition of 0.22 wt.% C, 1.5 wt.% Mn, 0.045 wt.% S, 0.045 wt.% P and 0.4 wt.% Si ascertained through optical emission spectroscopy. The microstructure of this material has two phases, namely, ferrite and pearlite as shown in Fig. 2.5.

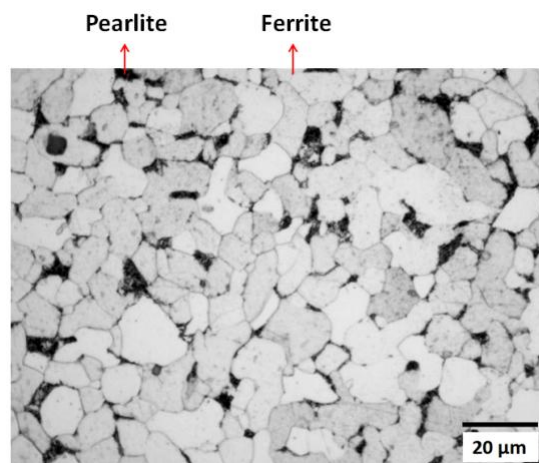


Figure 2.5 Optical micrograph of IS 2062 grade B mild steel

Among the steels which undergo Lüders instability, IS 2062 grade E250 B mild steel has wide range of applications because of which it is also called as general purpose steel. Since this steel has good malleability, ductility and weldability it is preferred as the primary structural material in many industries, particularly as pipes, storage tanks, plates, angles and hydraulic press structures etc. Also, this steel is used in bridges, buildings, durable storage containers, pressurized storage tanks, gears, screws, bolts, shafts, rivets, hydraulic clamps, rolls, cylinders, rams, spindles and pipes. Plates made of this material is considered ideal for use as base plates to provide anchoring for supports, thereby acting crucial to the integrity and strength of the structure. There are some surface critical

applications of this steel which need good and sustained surface finish, particularly the structural products of automobile industries.

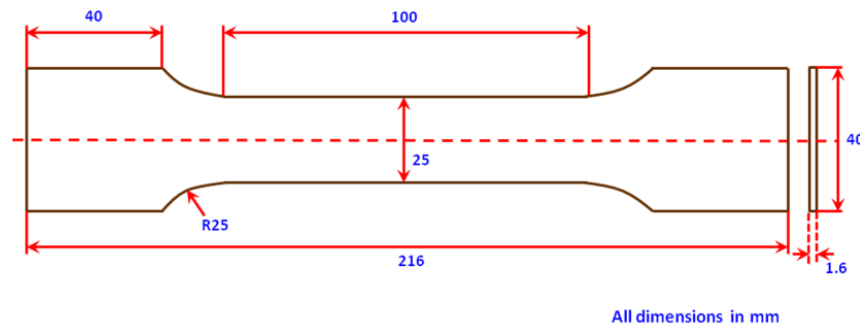


Figure 2.6 Schematic of specimen dimension

The geometry and dimension of the specimen used in this study are as per the ASTM standard E8/8m - 13a, Standard Test Method for Tension Testing of Metallic Materials. The dimensional tolerances of the specimen are as per the standard. All specimens before being tested are radiographed and ensured to be defect free. The schematic sketch of specimen is shown in Fig. 2.6. The surface variations were observed to be less than 50 μm using height gauge. The length of the tensile specimen was cut parallel to the rolling direction of the sheet metal to favor the formation of Lüders band.

2.7 Experimental setup and Methodology

The experimental setup involved a 100 kN displacement controlled, electromechanical, screw driven tensile testing machine, infrared camera and CMOS camera associated with DIC system as shown in Fig. 2.7. Infrared and CMOS cameras were focused on opposite sides of the flat surface of the specimen. A thin coat of black matt paint was applied over the specimen surface facing infrared camera to maximize the emissivity and make the temperature measurements absolute. The surface of the specimen facing CMOS camera was coated with random dot pattern (random black dots on a contrast white back ground) to achieve varying grey levels and perform image correlation.

This is done by first coating the specimen surface with matt white paint followed by manual marking of fine random black dots using a marker pen.

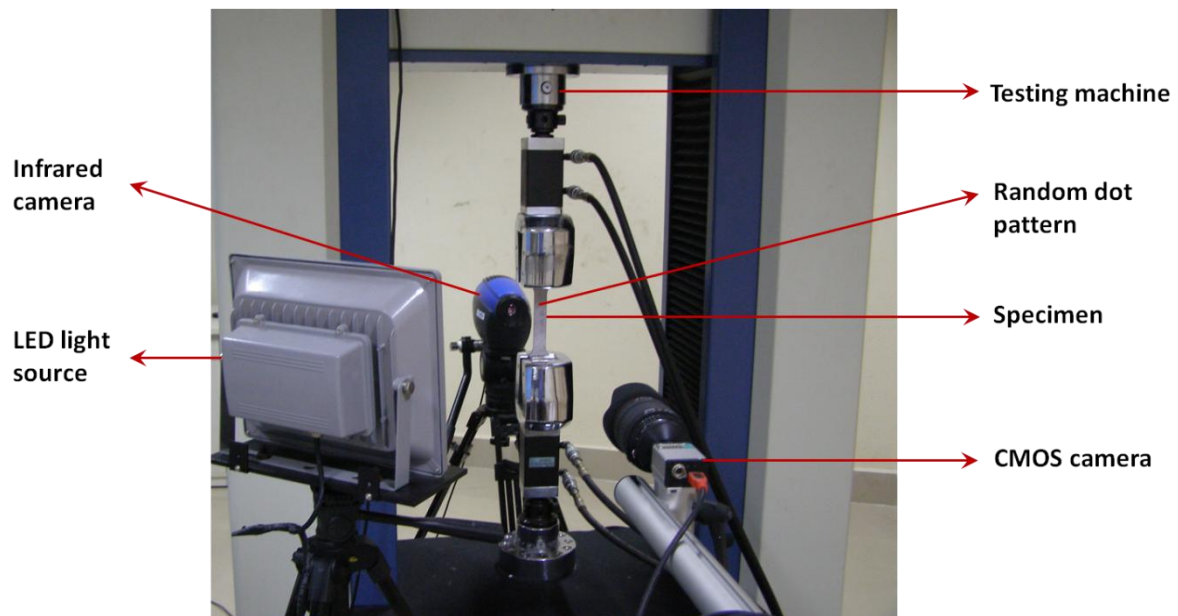


Figure 2.7 Schematic of experimental setup

The experimental procedure involves recording the thermal and digital images simultaneously during quasi static, monotonic, uniaxial tensile testing of the specimen. Though the field of view covered in both the cameras was sufficient enough to study even the fillet region of the specimen, the studies carried out focus only onto the thermal and strain evolutions on the reduced section (covering 100 mm in Fig. 2.6) of the tensile specimen. The infrared camera, digital imaging system and the testing machine are simultaneously triggered manually. With careful experimentation, the error in the synchronization is estimated to be less than 1s. The non-uniformity correction for the detector elements in the infrared camera (with non uniform gains and signal offsets for the same incident radiant power) is carried out by exposing a rough (nonreflecting) grey body (emissivity > 0.9) with homogeneous temperature directly in front of the detector or camera. The deviation of the gains and signal offsets of the detector elements is then corrected electronically. The infrared camera is calibrated by comparing the intensity of

infrared signal measured (in the form of voltage) from a black body (with thermocouple attached) at various desired temperatures in a controlled environmental conditions leading to a temperature-voltage calibration plot. The calibration procedure is repeated for a significant number of times in order to have reliable temperature-voltage plot. The variation in the emissivity induced by deformation is assumed to be negligible. Temperature variations observed during deformation (T) were subtracted from the reference temperature of the specimen (T_0) and are provided in terms of change in temperature θ ($= T - T_0$). The analysis of temperature variations of the specimen is performed with commercially available Altair Software from Cedip Systems.

Strain and strain rate fields were obtained by performing image correlation using commercially available Vic-2D digital image correlation processing software from Correlated Solutions. The correlation coefficient used in the present study is the normalized sum of squared differences (NSSD). To avail displacements in scales of real world other than pixels, calibration is carried out during the experiment by imaging a calibration grid (placed in the position of the sample) with black spots on a contrast white background separated at a defined distance. The distance between two chosen spots (preferably at longest possible distance) is then defined in the real scale (e.g. mm) while performing image correlation. Care is taken to avoid unnecessary objects in the surroundings, emission of IR rays from which can induce noise in the temperature measurement. Ambient temperature is ensured to be constant (298 K) throughout the test and the movement of air currents between the infrared camera and specimen is avoided.

CHAPTER – 3

STUDIES ON LÜDERS BAND FORMATION AND GROWTH KINEMATICS

This chapter discusses the combined application of IRT and DIC for visualizing and understanding the nucleation and growth kinematics of Lüders bands through the associated thermal and strain evolutions. Simultaneous characterization using IRT and DIC has an advantage of extracting information on both, the region undergoing plastic deformation at a particular instant by means of temperature localization and the track record of strain evolution till that time of investigation. The primary focus of this work is on the areas such as microstrain evolutions in the elastic region and their localization leading to Lüders band nucleation, band formation mechanism, kinematics of localization accompanying band front propagation, stress-strain-strain rate distributions across the band front etc. It also dwells upon the changes in the magnitude of local zones within the band width which constitutes to the band growth, thereby providing an insight into the band growth behavior. The results obtained in all these areas are compared with published experimental results, proposed models and concepts on Lüders instability.

3.1 Experimental

All experiments have been performed at room temperature (298 K). The spatial resolution achieved with infrared and optical imaging systems are 646 μm and 181 μm respectively, for the combination of lenses used and focal distances set in this study. Frame rate used in thermal imaging varied from 10-50 Hz, while in case of DIC, it varied from 5-10 Hz respectively. Although different frame rates were used in IRT and DIC

systems with recording time resolution in the range of 0.02 s to 0.1 s for different experiments, the analysis is performed only in units of a second, since experiments were carried out at low strain rates in the range of $1-5 \times 10^{-4}/s$. The subset sizes in the range of 21 x 21 pixels to 29 x 29 pixels are used for performing image correlation ensuring sufficient number of black spots within the subset. Since IR and DIC cameras were placed on opposite sides of the flat surface of the specimen, a feature that appears on both thermal and strain field was found to hold a mirror effect.

3.2 Spatiotemporal evolutions of temperature and strain accompanying Lüders instability

Figure 3.1 presents the load-time characteristics of the specimen deformed at a strain rate of $1.3 \times 10^{-4}/s$. No significant difference of upper and lower yield point is observed. The suppression of upper yield point is because of the stress raiser due to gripping and bands are nucleated in the zone close to grip region of the specimen at stress levels close to lower yield stress as explained by G.T. Van Rooyen [102].

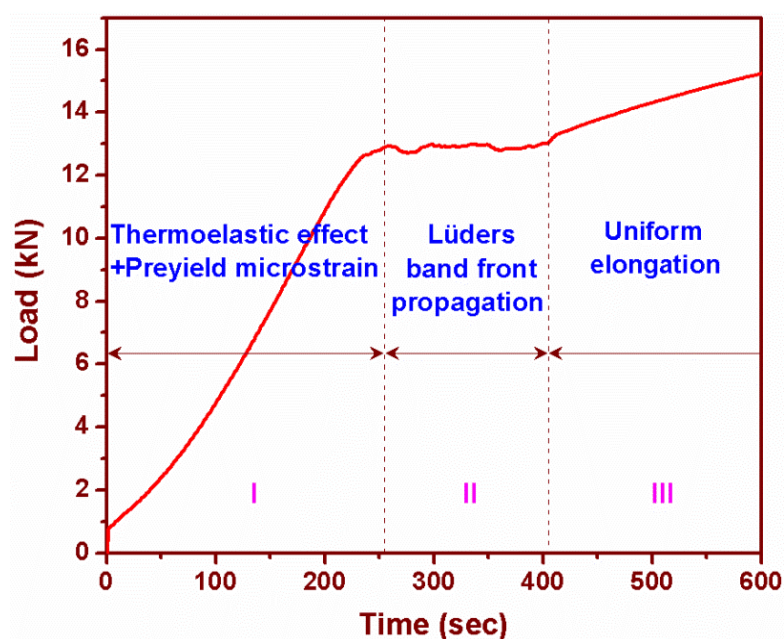


Figure 3.1 Load-time curve at $1.3 \times 10^{-4}/s$ strain rate

The load variations can be demarcated into three different regions based on the nature of the deformation behavior. Region I is where two phenomena namely thermoelastic effect and pre-yield microstrain occur. Thermoelastic effect refers to a small decrease in temperature of the material due to adiabatic expansion under elastic loading. This effect becomes negligible in the plastic regime. Small plastic strains of the order of 10^{-4} - 10^{-6} that occurs due to unlocking of dislocations from the Cottrell's atmospheres before the onset of macroscopic yield point are referred to as pre-yield plastic microstrain. In region II, inhomogeneous plastic deformation takes place accompanying the growth of Lüders bands (propagation of band fronts) over the entire gauge length followed by uniform strain hardening in region III.

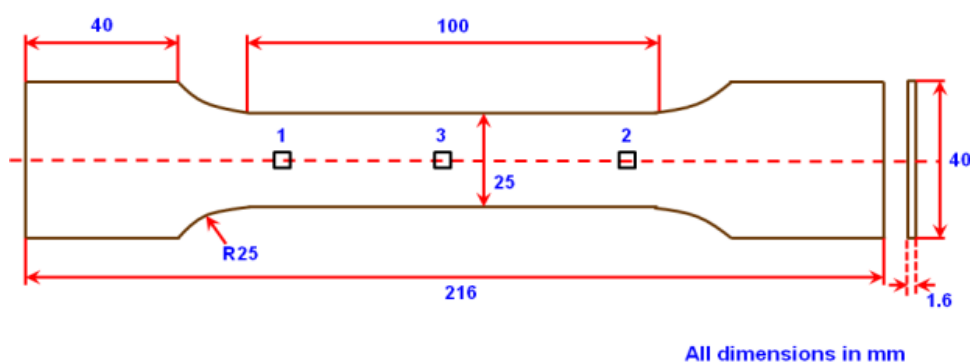


Figure 3.2 Local zones of interest along the gauge length

In this study, temporal evolutions of temperature and strain in various local zones of the specimen gauge length are studied using small square zones as shown in Fig. 3.2. A line profile over the central axis of the gauge length from top to bottom end is used for studying the axial distributions of temperature and strain. Figure 3.3 represents the temporal evolutions of temperature and strain in the considered local zones (zones 1, 2 and 3) and over the entire gauge length as average variations in all the three regions of the load-time curve.

3.2.1 Region I - Microstrain evolutions, Thermoelasticity and Lüders band formation

In region I, the average temperature decreases by 0.17 K at 200 s as shown in Fig. 3.3(a). Figure 3.3(c) reveals that the strain variations in all local zones in this region are very less till 200 s. After 200 s, both temperature and strain increase rapidly in zone 1 by 0.2 K and 12500×10^{-6} at the end of this region. No significant change in temperature and strain are observed in other zones of the specimen in this region.

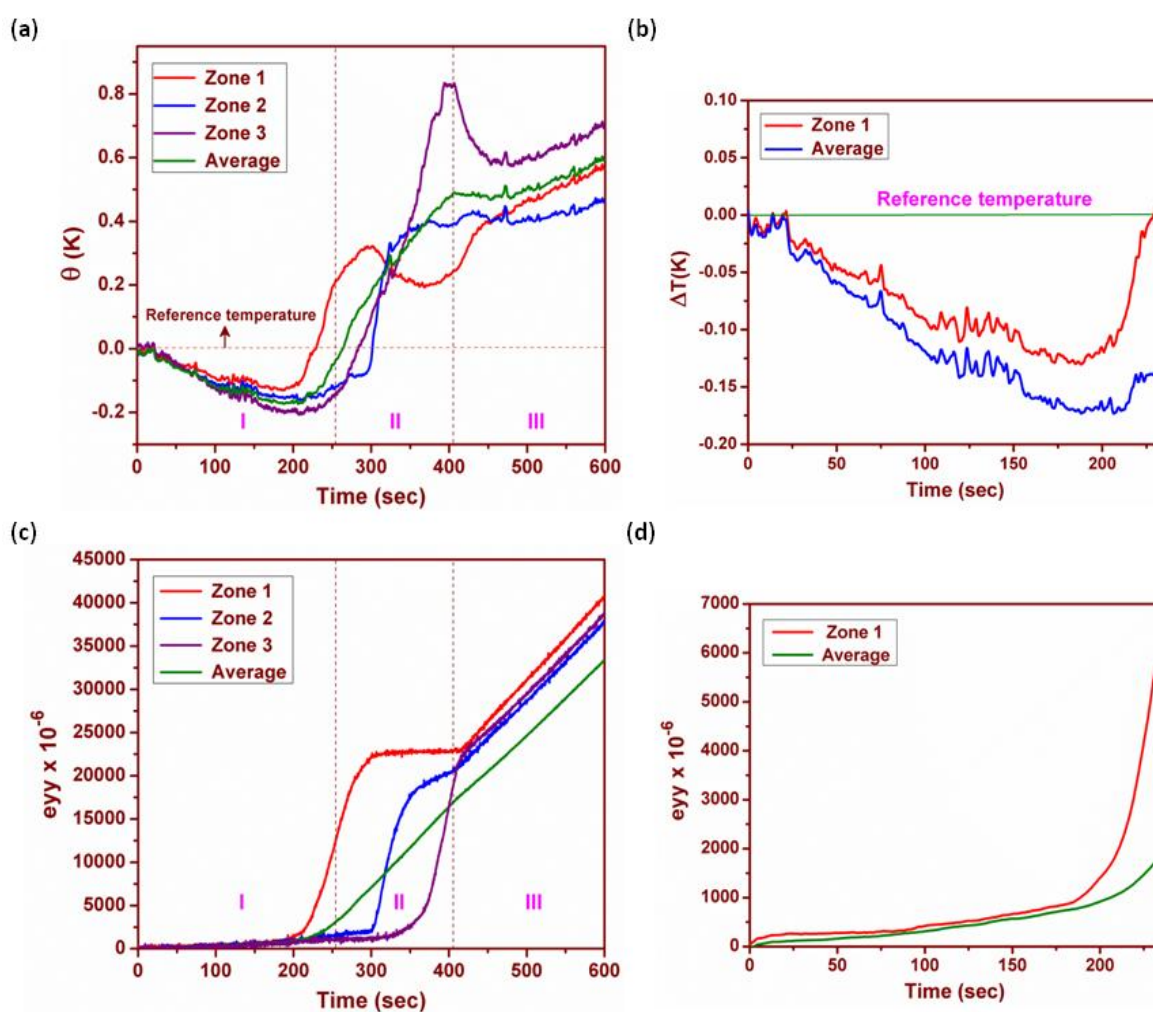


Figure 3.3 Temporal evolutions of (a) temperature in various local zones, (b) temperature in zone 1 during initial stages of elastic loading, (c) strain in various local zones and (d) strain in zone 1 during initial stages of elastic loading

Temperature and strain evolutions in zone 1 (upper end of gauge length close to fillet where band nucleation takes place) and their average over the entire gauge length of the specimen are plotted as a function of time till 234 s in Figs. 3.3(b) and (d) to study the behavior of microstrain evolutions before the lower yield stress and their influence on Lüders band nucleation.

From Fig. 3.3(b) it is evident that there is a drop in the temperature and this is attributed to the phenomenon of thermoelastic effect [138]. It is well known that there exists an interrelationship between the stress and strain (mechanical work done on a material) in the elastic region and changes in thermodynamic properties i.e. the temperature and entropy. In the elastic range, when stress is applied rapidly to a tensile specimen such that the maximum stress is reached before the specimen can exchange any thermal energy with the surroundings, the heat transferred to or from the specimen is negligible. So the change in internal energy is caused only by the mechanical work done on the material and the stressing is isentropic i.e. at constant entropy. For uniaxial adiabatic straining, the change in temperature of the specimen with strain is given by [139],

$$\frac{\delta T}{\delta \varepsilon} = \frac{-V_m \alpha E T}{C_v} \quad \text{-(3.1)}$$

where, $\delta T/\delta \varepsilon$ represents the change in temperature with strain at constant entropy, V_m is the molar volume of the specimen, α the linear thermal expansion coefficient of the specimen, E the isothermal Young's Modulus, T the temperature in Kelvin and C_v the specific heat at constant volume. Since α is positive and V_m, T, E and C_v are all positive, adiabatic elastic tension lowers the temperature of the material. It has been reported that this temperature change would be very small of the order of about 0.2 K [138] which also depends on strain rate.

Temperature drop in zone 1 of the gauge length due to thermoelastic effect is less when compared to that of the average decrease in temperature of the gauge length as seen in Fig. 3.3(b). Curves overlap till 23 s and as applied load increases with time, the difference between temperature of zone 1 and average temperature also increases. This confirms the existence of non-uniform plastic deformation in zone 1 before the onset of macroscopic yield point. After 200 s, temperature increases rapidly in this zone. The same can also be noticed by observing rapid increase in difference between the temperature of zone 1 and average temperature after 200 s. A similar behavior is observed in Fig. 3.3(d) where strain in zone 1 initially increases incrementally and after 200 s this rise is drastic reaching 6200×10^{-6} at the end close to upper yield point. This is because the rate at which dislocations are generated is a function of local stress at the dislocation source which in turn is a function of the applied stress. This observation is in line with the microstrain measurements in low carbon steel using strain gauges by T. Vreeland et al. [140]. Hence, after 200 s, microstrain rate increases rapidly in zone 1 (stress concentration zone because of gripping) as applied stress increases and approaches close to the upper yield point.

3.2.1.1 Thermoelastic effect and Microstrain evolutions

Figure 3.4 shows the thermal fields θ (K), strain fields ϵ_{yy} (of the order of 10^{-6}) of complete gauge length of the specimen and their axial profiles at different time instants in the interval of 65-200 s. At 65 s, the temperature at the center of gauge length decreases by 0.08 K, whereas in the upper and lower ends the decrease is only about 0.04 K and 0.06 K respectively. This confirms the adiabatic expansion of the material along gauge length. Relatively higher temperature at the ends of gauge length is due to the fact that the grips of the machine which is in physical contact with the specimen ends act as a source of heat to these specimen ends to maintain thermal equilibrium. The decrease in temperature of the center zone of the gauge length which is far away from the grips is more when compared

to the ends. On the other hand, strain in the gauge length is not uniform (with temporary wave pattern) with the peak strain of magnitude of about 350×10^{-6} localized at 376th pixel as seen in the corresponding strain field. This is nothing but the plastic microstrain which generally occurs in zones with favorable orientation of grains possessing the maximum of resolved shear stress at a particular load level. It is also to be highlighted that strain in the upper end (zone 1) is comparatively significant being about 250×10^{-6} .

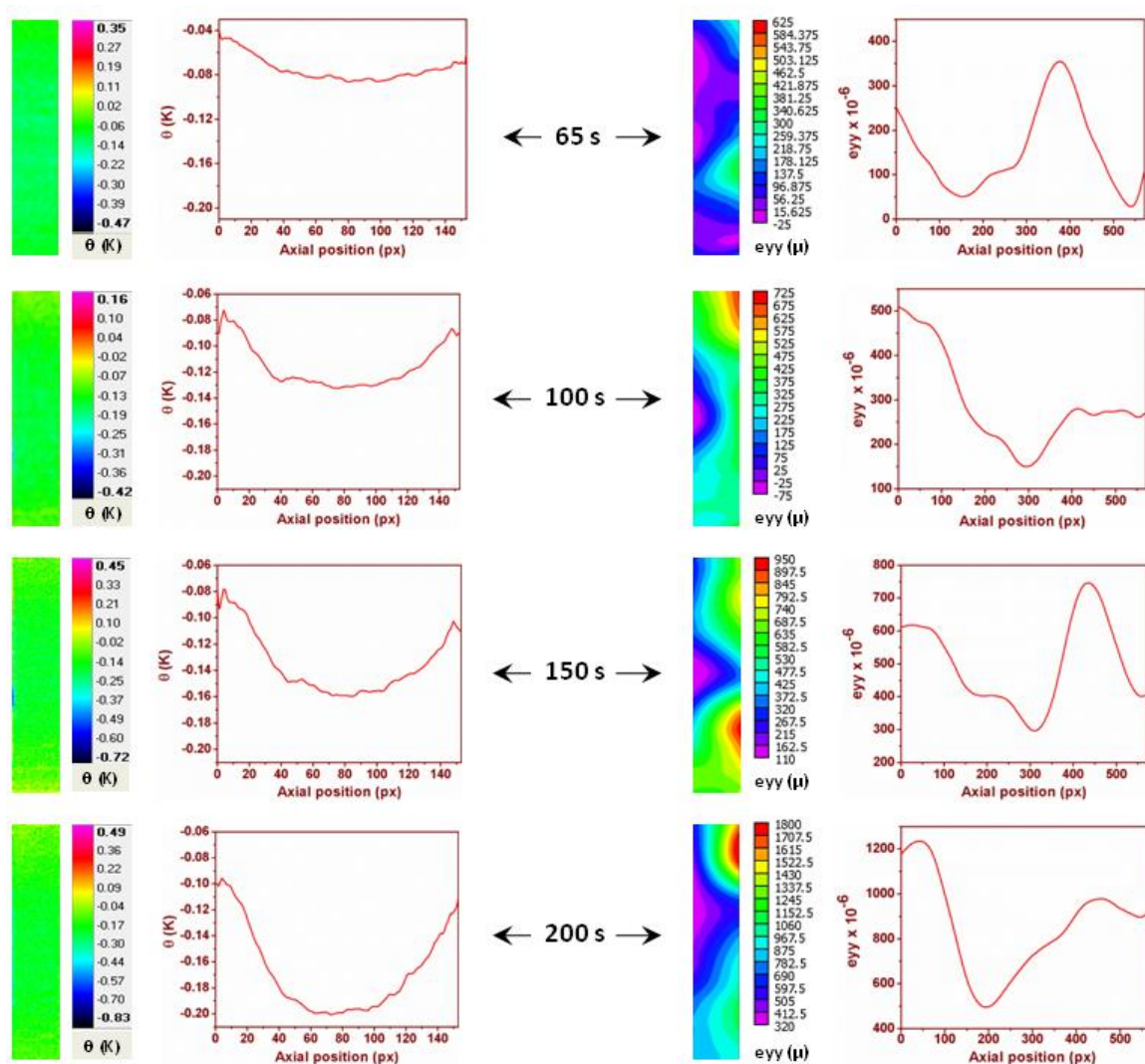


Figure 3.4 Thermal, strain fields and their axial profiles in the interval of 65s - 200s

In the time interval of 100-200 s, within the elastic limit, the specimen exhibits relatively intense localized plastic microstrain in various zones along the gauge length as seen in the strain fields and their axial profiles in Fig. 3.4. In all these zones which exhibit

localized microstrain, temperature evolution and localization is expected in the corresponding thermal profiles. But, temperature decreases over the entire gauge length as revealed by the thermal profiles in this interval. It is felt that the magnitude of temperature increase as a result of microstrain evolutions is quite small compared to the decrease in temperature due to thermoelastic effect and hence temperature localization accompanying localized microstrain gets masked and does not manifest in the thermal profiles. It is to be highlighted that in this interval, though relatively intense microstrain localizations occurred in various zones, upper end (zone 1) exhibits continuous straining confirming that considerable dislocation activity in this zone continues to occur. The fluctuations in the microstrain patterns observed in the strain fields are found to be in line with the fluctuations in the strain rate pattern reported by Mudrock et al. [141] in Al-Mg alloy. Such type of fluctuations in the localized microstrain is because of the variation of maximum resolved shear stress with the corresponding applied load level. Although microstrain localizations fluctuate, they are found to be self organized in the respective local zone, which is also in line with the observations of Mudrock et al. [141].

As the applied load approaches close to macroscopic yield point, stress concentrations induced in the fillet (close to upper end of gauge length) due to gripping develops and results in comparatively higher values of strain. At 200 s, where thermoelastic effect becomes negligible and load level (10.8 kN) is close to upper yield point (12.8 kN), strain in the upper end increases enormously to about 1200×10^{-6} as seen in Fig. 3.4. The temperature at the ends and the center of gauge length decreases and at the center the decrease is about 0.2 K (Fig. 3.4).

3.2.1.2 Lüders band formation

Figure 3.5 reveals that the temperature and strain increases locally in the upper end of gauge length (zone 1) in the time interval of 210-230 s. This is attributed to the drastic

increase in slip activity in this zone. No considerable change in the strain pattern of other zones of the specimen is noticed. Therefore, one can conclude that in this interval, with increase in applied stress, stress concentration builds up considerably in zone 1 enhancing the slip activity thereby creating a cluster of yielded grains. Hence upper end (zone 1) becomes a favorable zone for nucleation of Lüders band. In other words, the temporary strain wave pattern observed in Fig 3.4 becomes stable in the zone 1 leading to the nucleation of Lüders band with the aid of the stress concentration. Lüders nucleus is observed in both thermal and strain fields at 210 s itself. In this interval, thermoelastic effect is negligible and hence dislocation activities leading to microstrain evolutions have significant temperature rise as observed in the thermal fields.

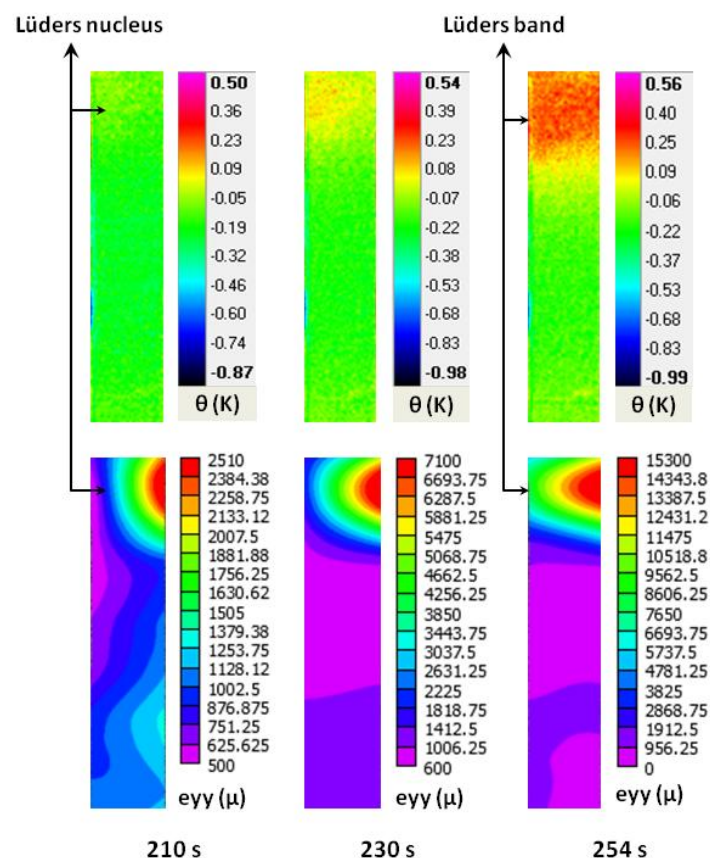


Figure 3.5 Nucleation and formation of Lüders band

After the nucleation of Lüders band in the upper end, the nucleus traverses the cross section of the specimen developing as fully grown Lüders band with flat, sharp front

at 254 s corresponding to the upper yield point as revealed by the thermal and strain fields. Thermal and strain fields also indirectly reveal that 100% grains in the upper end (nucleation zone) are yielded at upper yield stress matching with microstructural observation of Suits et al. [70]. Some authors define upper yield stress as nucleation stress [62, 72, 85] but have not investigated the physical form of the band at this point except Miyazaki et al. [92] who found that band structure (in the form of a crack) traverses the specimen cross section at upper yield stress using digital camera which is in line with the present observations based on thermal and strain evolutions.

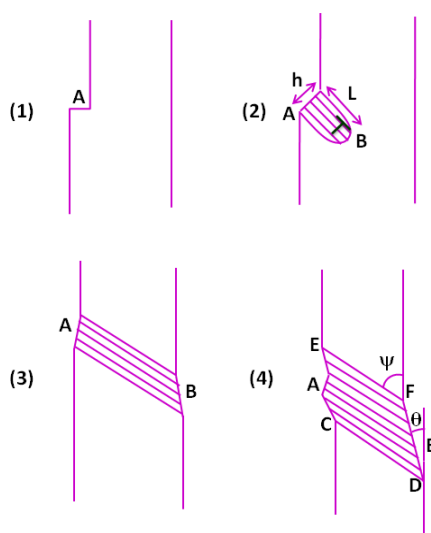


Figure 3.6 Nucleation and development of Lüders band - Friedel [142]

Friedel [142] has proposed a model explaining the mechanism of Lüders band formation which is depicted in Fig. 3.6. According to this model, nucleation occurs from surface step A (zone of stress concentration), traverses the cross section in the plane of maximum resolved shear stress and then propagates along the gauge length of the specimen. During tensile deformation, stress concentration is induced in the shoulders (fillet) of the tensile specimen because of gripping, resulting in dislocation pileups in the plane of maximum resolved shear stress in this zone. In the present study, nucleation occurs in the upper end of gauge length (zone 1 close to top fillet of tensile specimen

which develops stress concentration with increase in load) at 210 s, traverses the cross section at 230 s at an angle and then develops as a fully grown band with sharp band front at 254 s corresponding to macroscopic upper yield point as seen in Fig. 3.5. Macroscopic thermal and strain fields observed in Fig. 3.5 experimentally demonstrate the microscopic dislocation activities explained by the Friedel's band formation model.

3.2.2 Region II - Kinematics of Lüders band front propagation

In region II, the Lüders band front propagates along the entire gauge length of the specimen. From the beginning of this region, there is a drastic rise in average temperature and average strain reaching 0.49 K and 17400×10^{-6} at the end as shown by Figs. 3.3(a) and (c). Temperature and strain evolutions in local zones are also rapid and highly inhomogeneous clearly reflecting the deformation localization associated with the band front propagation. Temperature and strain in the zone 1 increases by 0.3 K and 22356×10^{-6} respectively at 300 s, where band front traverses almost half the gauge length of the specimen. No appreciable variations in temperature or strain are observed in the other local zones till 300 s. This confirms that yielding occurs only in the upper half of the gauge length in the interval of 254-300 s.

3.2.2.1 Stress-strain distribution across the band front

A model explaining the inhomogeneity in stress-strain distribution across the band front proposed by Van Rooyen [102] is shown schematically in Fig. 3.7. According to this model, the region within the band front (marked as B) which is yielded but not work hardened when compared to full Lüders strain will have flow stress less than the material adjoining it. In other words, load carrying capacity of this yielded zone, marked as C, decreases when compared prior to yielding. Therefore, most of the applied load is carried by the zone which has not yielded, i.e. elastic region close to band front where stress

varies from lower to upper yield stress (σ_1 to σ_2). From C to D, stress increases because of strain hardening and reaches saturation at D. This makes the stress-strain distribution across the band front (elastic-plastic boundary) highly inhomogeneous resulting in macroscopic stress concentrations in addition to the microscopic stress concentrations due to slip bands resisted by grain boundaries.

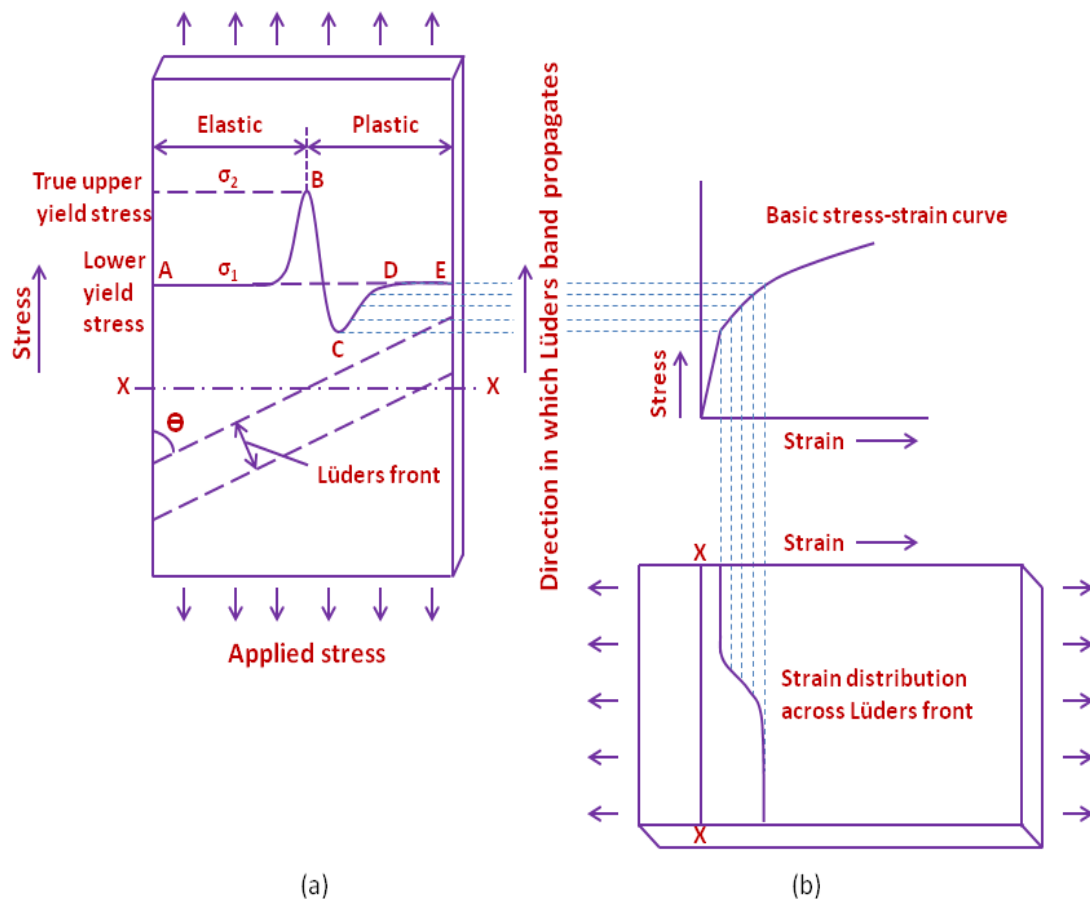


Figure 3.7 (a) Stress and (b) Strain distribution across the Lüders band front
- Van Rooyen [102]

Figure 3.8 represents the thermal-strain distribution measured across the band front at 300 s using IRT and DIC as a manifestation of inhomogeneity in stress-strain distribution, where the band front traverses almost half the gauge length of the specimen. Figures 3.8(b) and (d) represent the axial temperature and strain profiles from the top end of the gauge length to the bottom end along the line marked in the corresponding thermal

and strain fields shown in Figs. 3.8(a) and (c). The band front is identified from the strain field and its axial position is marked as B on the axial profiles of temperature and strain. The zones A and E representing elastic and plastic ends are marked as such in the axial profiles. The other local zones in the axial profiles, namely, C and D are marked with the understanding of the band deformation mechanism proposed by the model and its manifestation on the thermal and strain evolutions.

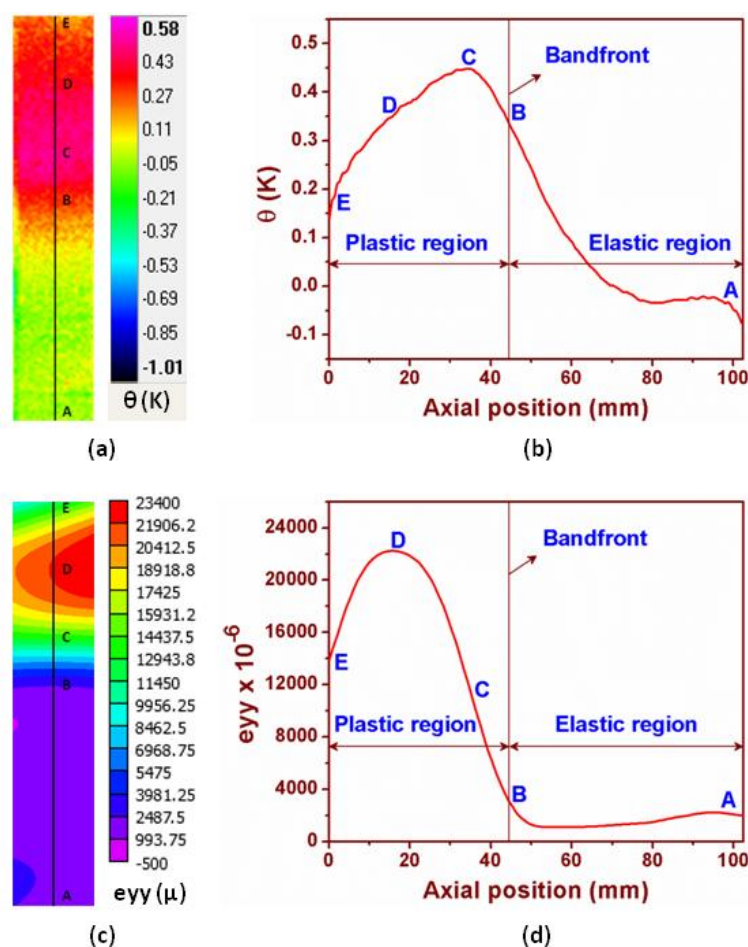


Figure 3.8 Thermal, strain fields and their axial profiles at 300 s

Comparing Fig. 3.7(a) with Fig. 3.8(b), it can be realized that there exists a good relation between stress and temperature distribution across the Lüders band front. From Van Rooyen's model shown in Fig. 3.7(a), stress is constant in the elastic region and on the approaching band front it increases drastically reaching upper yield stress. Similar to

this, in the elastic region, the temperature is constant initially to about 0.04 K as seen in Fig. 3.8(b) and on the approaching band front it increases and reaches 0.33 K at the band front. Increase in temperature observed here, despite having a major contribution by diffusion from the heat generated within the band, includes temperature rise from the plastic microstrain ahead of the band front under the influence of stress variation from lower to upper yield stress (σ_1 to σ_2). According to the model, strain is constant in the elastic region till the band front as shown in Fig. 3.7(b). In the strain distribution measured across the band front using DIC, strain is constant in the elastic region from the end marked as A and on approaching the band front B it increases slightly because of the microstrain evolutions associated with stress variation from lower to upper yield stress (σ_1 to σ_2) as shown in Fig. 3.8(d).

According to the model, in the plastic region, there is a drop in the stress initially reaching a minimum C less than the lower yield stress and then increases followed by saturation to lower yield stress at D as shown in Fig. 3.7(a). On the other hand, strain increases from a zone corresponding to C in the stress profile and then reaches saturation at D as shown in Fig. 3.7(b). From Fig. 3.8(b) it can be observed that temperature increases from B, reaches a peak C and then drops down to D. The peak C in the axial thermal profile corresponds to the dip C depicted by the model, where dislocations are mobile. These mobile dislocations are generated through the yielding of the material in the zone close to the band front under the influence of stress variation from lower to upper yield stress. Such a process leads to temperature variation from B to C as shown in Fig. 3.8(b). Using the axial position of C in the axial thermal profile, its corresponding position in the axial strain profile is identified. Similarly, using the axial position of D (where strain saturates) in the strain profile its corresponding position in the axial thermal profile is identified. Such identifications of points C and D in both the profiles and field

images have been possible only because of the simultaneous characterization using both the IRT and DIC.

The region from C to D is where material strain hardens and therefore it is expected to show considerable thermal evolutions. But due to thermal diffusion from zone C which has the peak temperature associated with the presence of mobile dislocations, thermal evolutions due to strain hardening gets masked leaving a decreasing nature from C to D in the temperature profile. Constant value of stress from D to E in the model corresponds to the zone where the band front started propagating with initiation from the end E. The drop in temperature observed in the axial thermal profile from D to E as shown in Fig. 3.8(b) is because of the diffusion losses associated with this prior plastic deformation to the gripping ends (which acts as heat sink). In the plastic region, strain increases gradually from B to C (where the material has yielded but not strain hardened) and reaches maximum in D (where the material is strain-hardened) as shown in Fig. 3.8(d). It is to be highlighted that unlike the model, C does not correspond to the start of increase of strain in the axial profile and the band front B identified from the strain field itself is found to be in the increasing path of strain. This observation depicts the actual strain profile in a practical case. Also, from D to E strain decreases contradicting the model. This decrease in strain observed from D to E is associated with symmetrical decrease of strain on either side of the intense strain hardened zone of the band.

Strain field in Fig. 3.8(c) also clearly depicts the symmetrical strain distribution on either side of the strain hardened zone within the band. In other words, there exists a region above the strain hardened zone, which is yielded comparable to that of zone C. Also, nucleation of band in the present case starts from the zone close to the top end of the reduced section at an angle and not from the exact end E of the gauge length as assumed in the model. From these observations, it is clear that the temperature-strain distributions

measured across the band front using IRT and DIC in this study not only experimentally correlate with the theoretical predictions of Van Rooyen's model [102] for inhomogeneity in stress-strain distribution across the band front but have also revealed some additional features that were not predicted by the model.

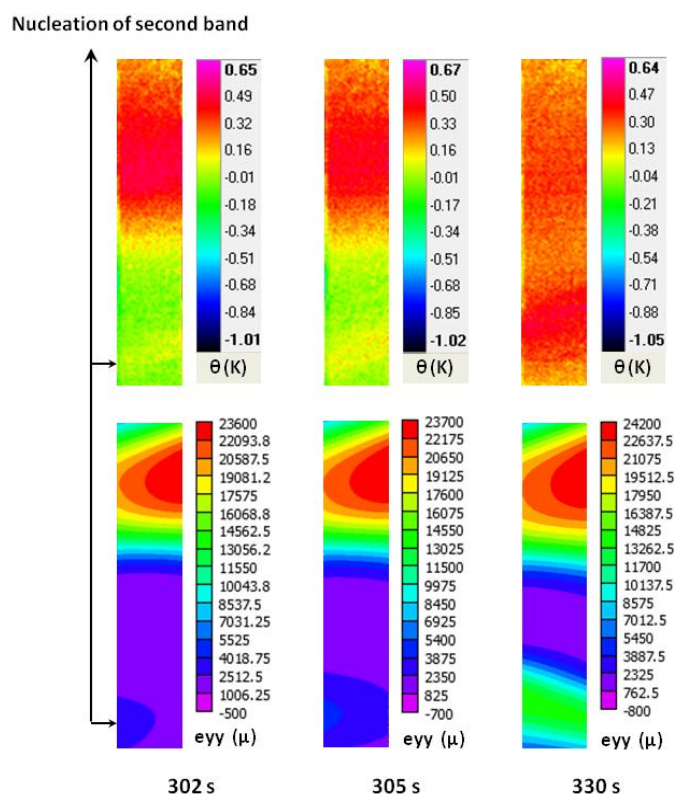


Figure 3.9 Thermal and strain fields revealing the second band formation and growth

In the interval of 300 s to 405 s, yielding occurs in the lower half of the gauge length, which is manifested with increase in temperature and strain on zones 2 and 3 in Figs. 3.3(a) and (c). This yielding is associated with the formation of the second band from the lower end of gauge length in the short interval of 302-305 s following the same nucleation mechanism proposed by Friedel [142] as revealed by thermal and strain fields in Fig. 3.9. Nucleation of the second band occurs at 302 s, traverses the cross section at 305 s thereby developing as a fully grown band which then propagates towards the center of the gauge length. A considerable decrease in the temperature and constant value of strain in zone 1 in this interval as observed from Figs. 3.3(a) and (c) reveal that material

yields no more in the upper half of the gauge length and the existing temperature starts to diffuse.

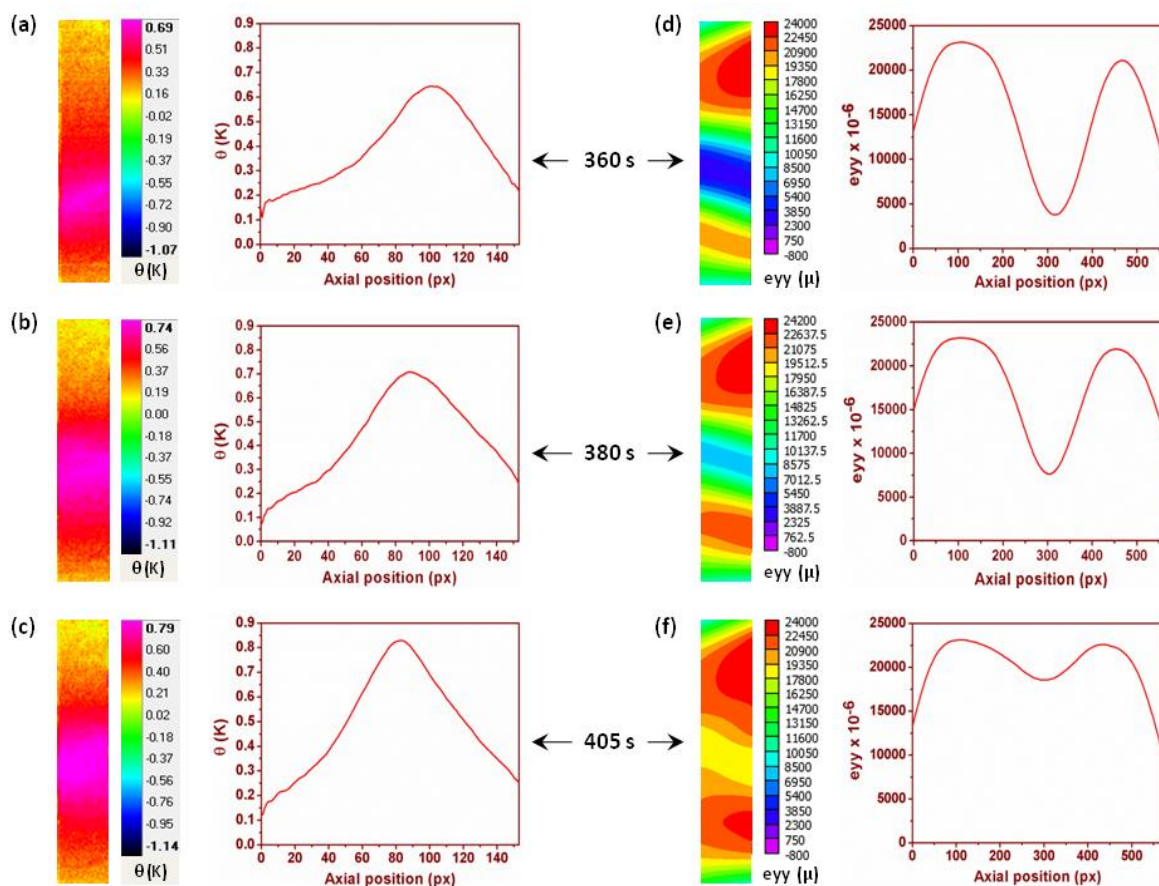


Figure 3.10 Thermal, strain fields and their axial profiles in the interval of 360-405s

At 360 s, second band front covers the lower half of the gauge length as shown in Figs. 3.10(a) and (d). One can visualize the difference in the magnitude of strain between the upper and lower half of the gauge length from Fig. 3.10(d). It can be inferred from Figs. 3.3(a) and (c) that even after the band fronts completely cover the entire gauge length (i.e. after 360 s), temperature and strain variations are localized in the zones 2 and 3 till 405 s. The same observation can also be visualized from the thermal and strain fields and their corresponding axial profiles in Fig. 3.10 in the form of temperature and strain localization from lower end to center. Such deformation after the band front propagation is because, strain rate at the band front is high and some dislocations unable to move at

higher strain rate continue to move at a lower velocity after band front crosses as explained by Kyriakides et al. [143]. Therefore within the band front, some grains yield further and some undeformed grains undergo delayed yielding. Such delayed yielding appears in the axial thermal profiles as a shift in the temperature peak (which represents a zone of deformation at particular instant) from lower end to center as seen in Figs. 3.10(a)-(c). In the axial strain profiles, delayed yielding is reflected as broadening of the peak strain with increase in their magnitudes as observed in Figs. 3.10(d)-(f). However, this interpretation on delayed localized yielding can be quantified only when the diffusion effect in the thermal fields and track record of strain associated with prior localization in the strain fields are avoided.

3.2.3 Region III - Uniform strain hardening

In region III, uniform strain hardening takes place and therefore uniform increase in temperature and strain are observed in Figs. 3.3(a) and (c).

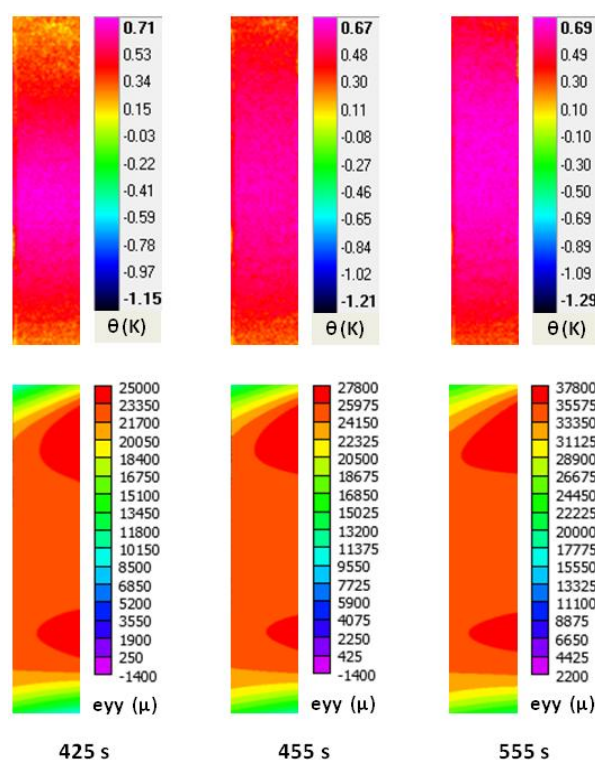


Figure 3.11 Thermal and strain fields in region III

The initial decrease in temperature in zone 3 is because the initial temperature rise due to uniform strain hardening in this zone will be less than the intense temperature evolution that took place after band front propagation in the end of the load plateau (i.e. in the near previous instant). This can also be visualized from the thermal and strain fields in Fig. 3.11. The strain hardened zones however possess relatively higher strain since they have undergone deformation much earlier than other regions of the gauge length.

3.3 Local zones of Lüders band and band growth behavior

In order to study the deformation behavior of local zones within the Lüders band width, namely, effective width and active zone (band growth parameters) which constitutes to the band growth, two specimens namely, specimen 1 and specimen 2 are considered. Optical images of specimens during deformation were captured at 10 Hz frame rate during the entire testing period followed by image correlation with 21 x 21 pixels subset size to estimate the strain and strain rate fields. Strain rate fields were computed by performing time derivatives of strain fields.

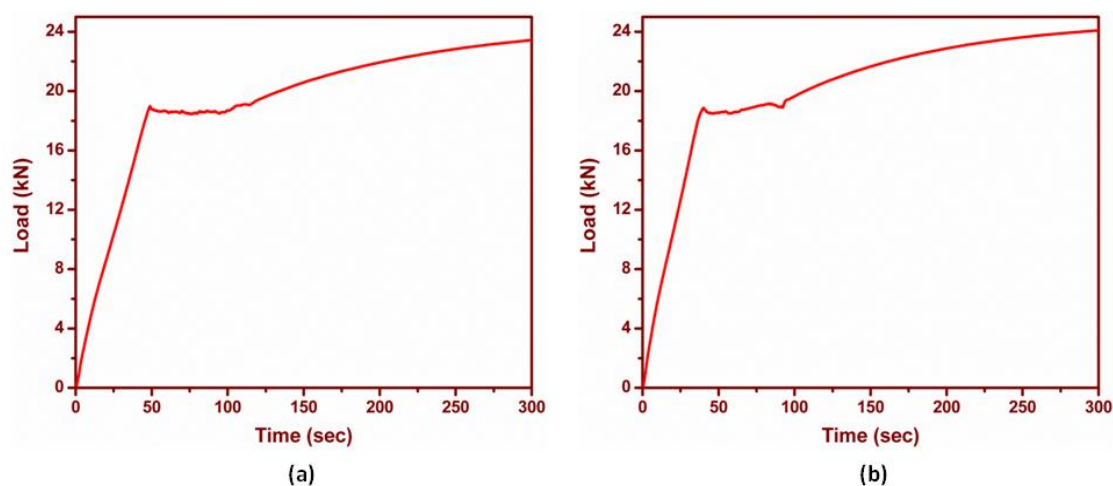


Figure 3.12 Load vs. time curve for (a) specimen 1 and (b) specimen 2.

Figures 3.12(a) and (b) represent the load-time curve obtained from specimens 1 and 2 with the load plateau involving band front propagation ranging between 49 - 115 s

for specimen 1 deformed at $4.16 \times 10^{-4}/s$ and 40.5 - 92.5 s for specimen 2 deformed at $5 \times 10^{-4}/s$. The difference in strain rate of both the specimens may influence only the magnitude of variation of the local zones and not their characteristic variation. Hence, the small difference in strain rate of two specimens is immaterial for the considered scope of the study. The primary aim of the study on specimen 2 is to check for the repeatability of observed variation of the magnitude of local zones of Lüders band in a situation when two band fronts propagate.

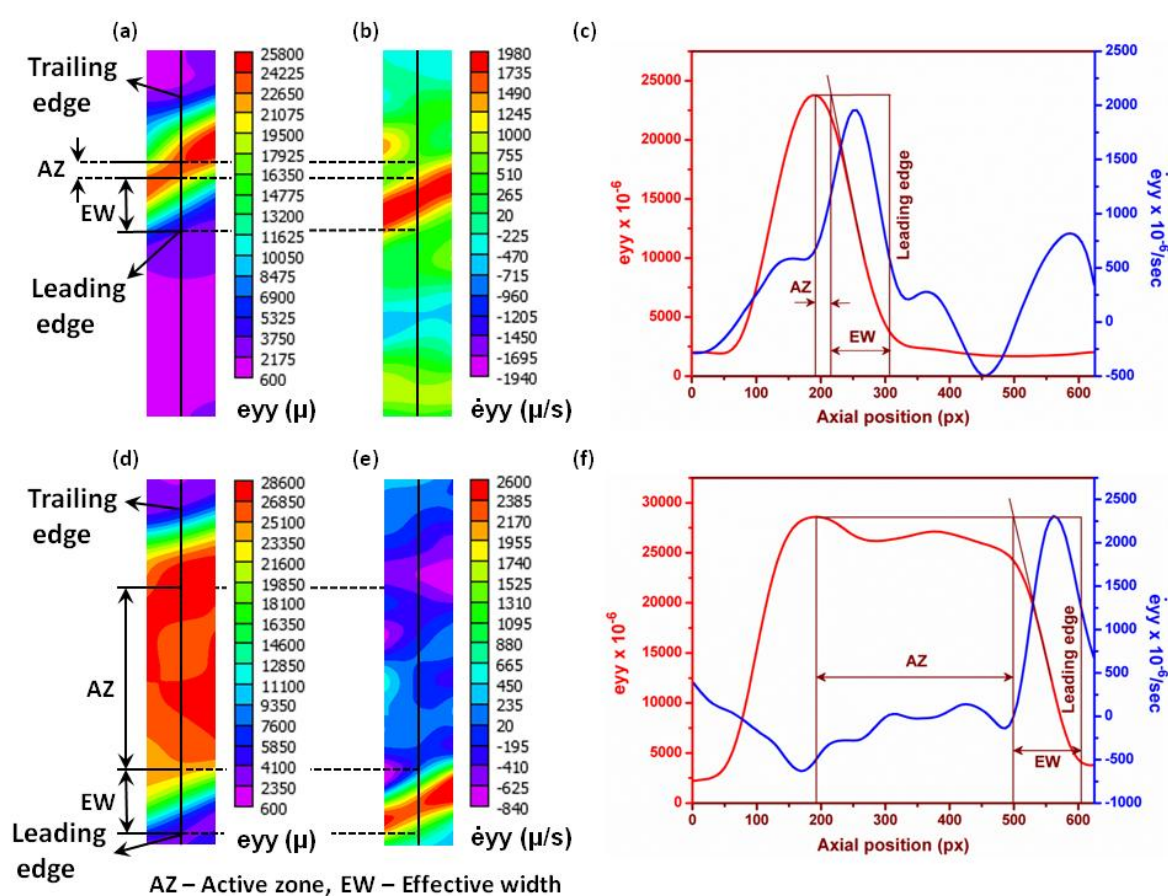


Figure 3.13 Strain field, strain rate field and their axial profiles at 60 s and 94 s for specimen1

Figure 3.13 depicts the strain, strain rate fields and their axial profiles along the axis of the gauge length of specimen 1 at 60 s and 94 s which are almost at the beginning and end of band front propagation in the load plateau. It can be observed from the strain

fields, that a single band with nucleation from the top end of the gauge length deforms the specimen through its front propagation towards the bottom end. Zone of linear variation of strain from the band front to within the band is called as effective width and the region following this effective width where strain approaches a constant value is referred as an active zone of Lüders band [102, 144]. Effective width and active zone are determined from the axial strain profiles obtained using DIC. Unlike the saturation of strain after linear variation from the band front predicted by Van Rooyen's model [102], in a real case strain reaches a peak in the strain hardened zone and then decreases. In other words, strain symmetrically decreases from the strain hardened zone towards the leading edge (band front which moves) and the trailing edge (band front which remains stationary) of the band as revealed by the strain field at 60 s and its axial profile in Figs. 3.13(a) and (c).

From Figs. 3.13(c) and (f), it is observed that the peak strain rate is localized in the effective width of Lüders band. The same can also be visualized from the strain rate fields in Figs. 3.13(b) and (e). This is indicative of the fact that deformation at any instant in the load plateau is mostly concentrated in the effective width. According to Van Rooyen's model [102], deformation mechanisms involved in Lüders band growth are of two stages, namely 1. yielding of material in the elastic region close to the band front (resulting in growth of effective width) and 2. work hardening of material within the effective width (resulting in growth of active zone). These two stages were proposed to be continuous and simultaneous resulting in constant effective width and increasing active zone (with constant magnitude) in the load plateau. But from Figs. 3.13(c) and (f) it can be observed that both effective width and active zone increase with the progress of deformation by band front propagation.

In order to confirm this observation, the magnitude of effective width and active zone is measured at various instances during the interval of band front propagation (band

growth) in the load plateau as shown in Fig. 3.14(a). It is observed that the effective width varies with oscillations contradicting its constancy proposed earlier [102] and active zone increases continuously with irregular magnitude in the load plateau. This shows that the above discussed two stages of deformation mechanism, namely, yielding and workhardening do not compensate each other exactly to the same magnitude of region within the band.

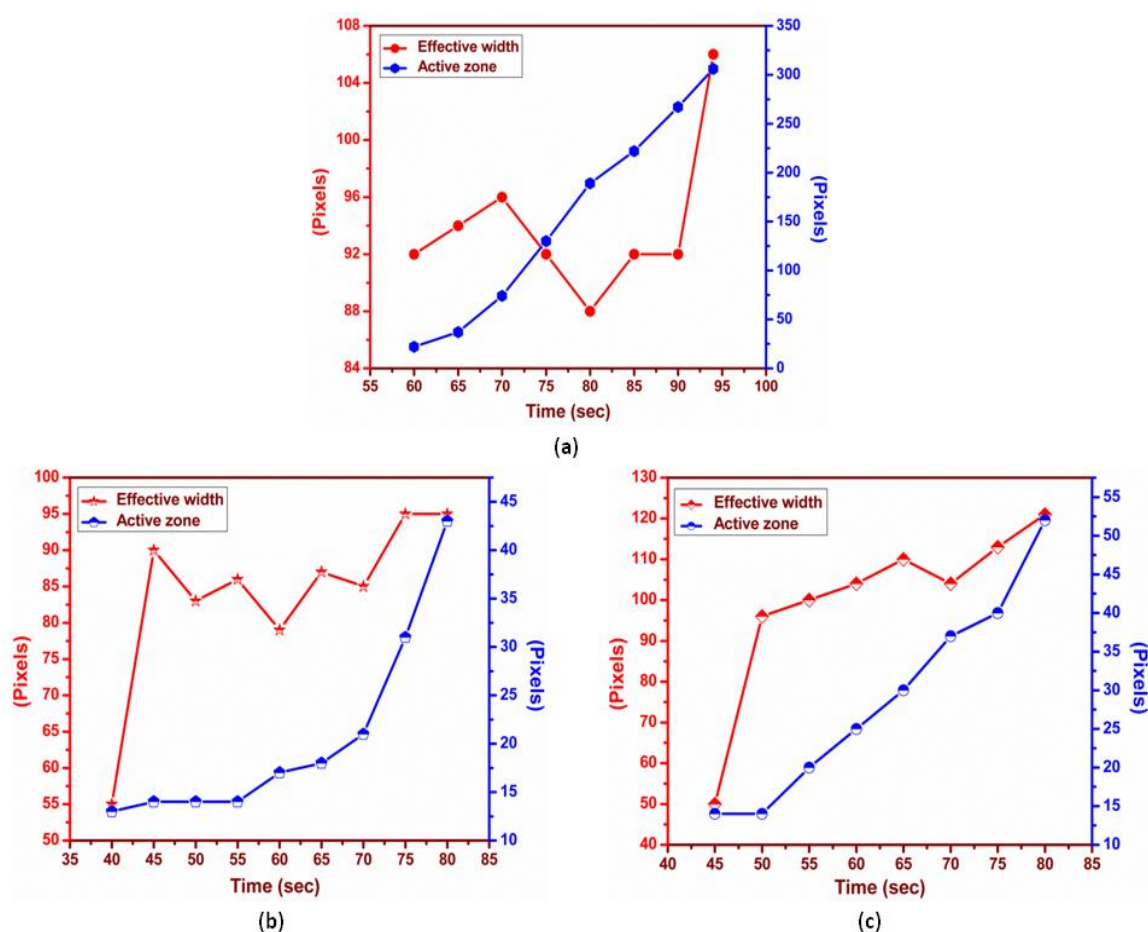


Figure 3.14 Variation of effective width and active zone in the load plateau for (a) specimen 1, (b) band 1 of specimen 2 and (c) band 2 of specimen 2

In other words, the entire yielded zone in the effective width is not work hardened immediately following the movement of the leading edge of the band. Finite value of strain rate on the trailing edge of the band and bottom end of the gauge length reflects mild deformations in these zones as observed in Figs. 3.13(c) and (f). Strain rate also varies

significantly in the active zone contradicting the assumption of constancy of strain rate in it [144]. The negative value of strain rate in some local region within the active zone is because of load relaxation of grains in these zones that are subjected to elastic straining in the near previous instant, which has also been observed earlier using DIC [141].

Figures 3.14(b) and (c) represent the variation of effective width and active zone of two bands, namely, band 1 and band 2 emanating from either ends of the gauge length of specimen 2. It is to be noticed that the effective width of two bands nucleating from the same specimen 2 are not the same at any particular instant. From Fig. 3.14(a) it can be observed that the effective width does not change in the interval of 85-90 s for specimen 1, whereas active zone increases. Similarly, for band 2 in specimen 2, active zone is constant but effective width increases in the interval of 45-50 s as seen in Fig. 3.14(c). These observations confirm that two stages of band growth mechanism involved, namely, yielding and work hardening need not be even successive. The observed variation in the effective width and active zone during the growth of the Lüders bands has been confirmed with many specimens. Table 1 shows the variation in the effective width and active zone of Lüders band in the load plateau for different specimens tested at same strain rate and thickness.

Specimen	EW variation in the load plateau	AZ variation in the load plateau
3.	70 to 147 pixels (25 mm)	13 to 104 pixels
4.	61 to 105 pixels (17.8 mm)	13 to 54 pixels
5.	75 to 175 pixels (18 mm)	14 to 42 pixels

Table 1.1 Variation of effective width and active zone for different specimens studied

No two specimens can have same magnitude of variations in EW or AZ since the dislocation arrangement and extent to which there are pinned vary. In fact, two bands

fronts in the same specimen propagating from the gauge ends will not have same magnitude of variations of the EW as shown in the case of specimen 2.

In this study, IRT and DIC have been applied simultaneously to experimentally investigate the kinematics of Lüders band nucleation and growth. Decrease in temperature due to thermoelastic effect and fluctuating but self organized microstrain evolutions are observed in the initial stages of elastic region. Following the end of influence of thermoelasticity, temperature and strain evolutions were localized and rapid in the stress concentration zone reflecting the rapid generation of dislocations. It is also confirmed through visualization that at upper yield stress, nucleus is no more a nucleus, but traverses the complete cross section at an angle developing as a fully grown band following the same mechanism proposed by Friedel [142]. The zone of band nucleation has been observed much ahead of the upper yield point using thermal and strain evolutions. Inhomogeneity in thermal-strain distribution across the Lüders band front demonstrated the inhomogeneity in stress-strain distribution proposed by Van Rooyen [102] with some additional features such as symmetry in strain distribution on either side of the strain hardened zone and strain evolutions much before band front which were not predicted by the model. It has been observed that the effective width of Lüders band varies and active zone increases irregularly in the load plateau reflecting the irregularity involved in the two stages of band growth. It is also found that strain rate always peaks in the effective width of Lüders band and varies in the active zone.

CHAPTER – 4

HEAT POWER AND STRAIN RATE BASED STUDY ON LÜDERS INSTABILITY

IRT and DIC have been widely preferred for studying plastic instabilities in the past two decades since the visualization of associated strain localizations is possible without any complicated experimental setup or procedures. In thermal imaging, the thermal transients accompanying deformation and the associated diffusion effects (particularly for metals which have relatively higher thermal diffusivity) blur the temperature localization zone accompanying plastic localization, if any. Therefore, quantitative information on the kinematics of localization cannot be extracted based on thermal fields. Since heat is inherent to plastic deformation, a methodology to estimate it from the experimental temperature data has been proposed earlier [145-146] and reported to be successful in revealing the strain localization associated with the necking phenomenon quantitatively without the effects of diffusion. On the other hand, the track record of strain in the DIC strain field associated with prior plastic deformation makes the interpretation and identification of the zone of strain localization difficult at any particular instant. To overcome this, strain rate evolutions have been used and were found successful in mapping the plastic localizations associated with Portevin-Le Chatelier effect [141].

This chapter focuses on the estimation of heat power and strain rate evolutions for quantitative analysis of the kinematics of localization accompanying the Lüders deformation. The advantage of heat power and strain rate variations over the thermal and strain variations in revealing the plastic localization associated with the nucleation and growth of Lüders bands without the influence of signatures of prior plastic localization is

highlighted. It also dwells on characterizing the delayed localized yielding using heat power and strain rate evolutions, the occurrence of which at the end of the load plateau was doubtful based on thermal and strain fields as discussed in chapter 3. The other important objective of this work is to study the characteristic variations of thermomechanical parameters such as dissipative heat power, stored power and energy conversion rate ratios during nucleation and growth of Lüders bands which is expected to provide an insight into the associated hardening/softening behavior based on the information on fractional conversion of the acting plastic power into stored and dissipated heat powers.

4.1 Background Theory

4.1.1 Thermomechanical frame work

According to classical thermodynamics of irreversible process, the thermodynamic equilibrium state (thermal, mechanical and microstructural) of a volume element at any particular instant is characterized by a set of $n+1$ state variables [147]. They are: the strain tensor ε , the absolute temperature T and a set of internal variables α_j ($j = 1, \dots, n-1$) which completely describe the microstructural state of the material. Considering the Helmholtz free energy $\psi = \psi(T, \varepsilon, \alpha_j)$ as the thermodynamic potential, the dissipation d from the Clausius-Duhem inequality [145] is defined as,

$$d = (\sigma - \rho\psi_{,\varepsilon}) : \dot{\varepsilon} - \rho\psi_{,\alpha_j} \cdot \dot{\alpha}_j - \frac{q}{T} \cdot \text{grad}T \geq 0 \quad - (4.1)$$

where, σ denotes the stress tensor, ρ the material density and q the heat flux vector. The dots stand for the time derivative of the respective state variables. It is assumed that intrinsic or mechanical dissipation W'_{dis} and thermal dissipation W'_{tdis} are individually positive as follows:

$$W'_{dis} = (\sigma - \rho\psi_{,\varepsilon}) : \dot{\varepsilon} - \rho\psi_{,\alpha_j} \cdot \dot{\alpha}_j \geq 0 \quad \& \quad W'_{tdis} = -\frac{q}{T} \cdot gradT \geq 0 \quad - (4.2)$$

The local heat diffusion equation by combining both principles of thermodynamics is then given by:

$$\rho C_{\varepsilon,\alpha} \dot{T} + div(-k gradT) = (\sigma - \rho\psi_{,\varepsilon}) : \dot{\varepsilon} - \rho\psi_{,\alpha_j} \cdot \dot{\alpha}_j + \rho T \psi_{,T,\varepsilon} : \dot{\varepsilon} + \rho T \psi_{,T,\alpha_j} \cdot \dot{\alpha}_j + r_e \quad - (4.3)$$

where, k represents the heat conduction tensor, r_e the external heat supply from the surroundings and $C_{\varepsilon,\alpha}$ the specific heat capacity at constant ε and α . The term $\rho C \dot{T}$ stands for the heat rate and $div(-k gradT)$ denotes the volumetric heat loss by conduction. The mechanical (intrinsic) dissipation term W'_{dis} denotes the irreversible transformation of mechanical energy into heat, the Kelvin's term $W'_{ther} = \rho T \psi_{,T,\varepsilon} : \dot{\varepsilon}$ represents the volumetric heat rate as a result of thermoelastic couplings and the internal coupling sources term $\rho T \psi_{,T,\alpha_j} \cdot \dot{\alpha}_j$ stands for the volumetric heat rate as a result of interaction between temperature and other microstructural state variables.

4.1.2 Heat power estimation

Estimation of heat power from the infrared thermal data is based on the following hypotheses:

1. The density, specific heat capacity and heat conduction tensor remain constant and are independent of the thermodynamic state.
2. k is assumed to be isotropic, i.e. $k_{ij} = \lambda_c \cdot \delta_{ij}$ where, δ is the identity tensor and λ_c the isotropic conduction coefficient.
3. The convective terms in the temperature time derivative are neglected, since gradients of temperature and displacement velocity amplitudes are very small during a quasi-static process.

4. Temperature variations during the tensile test does not affect the microstructural state and hence the internal coupling sources are neglected (i.e. $\rho T \psi_{T, \alpha_j} \cdot \dot{\alpha}_j = 0$). However, the associated thermoelastic coupling effects are considered. The thermoelastic sources in comparison with that defined by classical thermoelastic model can then be modified as $W'_{ther} = -\alpha_d T_0 \text{Tr } \dot{\sigma}$ [44]. Here, α_d is the thermal expansion coefficient, T_0 the absolute temperature and Tr stands for the trace operator.
5. The external heat supply r_e by radiation is time independent. These hypotheses reduce Eq. (4.3) to the following two dimensional diffusion equation.

$$\rho C \left(\frac{\partial \theta}{\partial t} + \frac{\theta}{\tau} \right) - k \left(\frac{\partial^2 \theta}{\partial x^2} + \frac{\partial^2 \theta}{\partial y^2} \right) = W'_{dis} + W'_{ther} \quad - (4.4)$$

$$\rho C \left(\frac{\partial \theta}{\partial t} + \frac{\theta}{\tau} \right) - k \left(\frac{\partial^2 \theta}{\partial x^2} + \frac{\partial^2 \theta}{\partial y^2} \right) = W'_{hs} \quad - (4.5)$$

where, $W'_{hs} = W'_{dis} + W'_{ther}$ is the overall heat power. Here, $\theta = T - T_0$ is the temperature variation averaged over the specimen thickness (T_0 is the reference temperature). The constant τ denotes the time characterizing heat losses perpendicular to the surface of the specimen due to convection and radiation. Diffusion effects as a result of heat conduction in a plane are taken into account by the Laplacian term in the heat equation. Therefore, heat power evolutions provide quantitative information on the plastic strain localization by taking into account the heat losses due to conduction, convection and radiation.

4.1.3 Estimation of plastic, dissipated heat and stored powers

During deformation, a part of the expended mechanical energy is dissipated as heat and the remaining is stored in the material. The mechanical power per unit volume acting on the material is given by:

$$W'_{ext} = W'_{hs} + W'_s \quad - (4.6)$$

where, W'_s is the stored power. The mechanical power per unit volume is decomposed into elastic and plastic parts as follows:

$$W'_{ext} = W'_e + W'_p \quad - (4.7)$$

where, W'_e and W'_p represent the elastic and plastic powers respectively. The mechanical and elastic powers are defined as, $W'_{ext} = \sigma \cdot \dot{\epsilon}$ and $W'_e = \sigma \cdot (\dot{\sigma}/E)$ respectively. Here, E is the modulus of elasticity, σ the true stress, $\dot{\sigma}$ the true stress rate and $\dot{\epsilon}$ the true strain rate.

Therefore, the plastic work rate or plastic power per unit volume is deduced as:

$$W'_p = W'_{ext} - W'_e \quad - (4.8)$$

The heat power per unit volume estimated using the heat diffusion equation is given by:

$$W'_{hs} = W'_{dis} + W'_{ther} \quad - (4.9)$$

where, W'_{ther} denotes the thermoelastic coupling power per unit volume defined as

$W'_{ther} = -\alpha_d T_0 Tr \dot{\sigma}$. Dissipative heat power per unit volume is then deduced as:

$$W'_{dis} = W'_{hs} - W'_{ther} \quad - (4.10)$$

After correcting the heat power for thermoelastic coupling power and mechanical power for elastic power, Eq. (4.6) becomes:

$$W'_p = W'_{dis} + W'_s \xrightarrow{yields} W'_s = W'_p - W'_{dis} \quad - (4.11)$$

Hence, stored power or rate at which energy is stored in the material can be estimated using Eq. (4.11). The measure of fraction of plastic work rate (plastic power) converted into heat dissipation rate (heat power) is given by:

$$\beta_1 = W'_{dis} / W'_p \quad - (4.12)$$

The fraction of plastic work rate converted into stored energy rate is then given by:

$$\beta_2 = 1 - \beta_1 \quad - (4.13)$$

4.2 Methodology adopted for heat power and strain rate estimation

The thermal and strain field data used for heat power and strain rate estimation in this study are from the same specimen (Fig. 3.1) discussed in chapter 3. Since heat equation involves differential operators which in general amplify the noise in the thermal images, the temperature data obtained experimentally are subjected to spatial and temporal filtering before being used for heat power estimation. Noisy temperature fields in both the spatial and temporal terms of heat diffusion equation are smoothed using a 2D convolution product involving a Gaussian low pass filter performed with the `filter2` Matlab function. Heat powers associated with the experimentally determined temperature fields are then estimated by evaluating the left hand side of the heat equation (Eq. 4.5). Finite difference centered scheme is used for both temporal and the spatial terms of heat equation. Heat power estimation from the 2D heat equation and associated image processing has been explained in detail in [145,148]. Strains rate fields are estimated by performing time derivative of the Lagrangian strain fields obtained using DIC.

4.3 Spatiotemporal evolutions of temperature and heat power

Figure 4.1 depicts the spatiotemporal evolutions of temperature and heat power accompanying Lüders instability with the load-time plot superimposed on them. Y axis of the plots represents the complete gauge length of the tensile specimen, the temperature and heat power evolutions over which are averaged along the gauge width and X axis represents time. Temperature evolutions shown in Fig. 4.1(a) reveal the strain localizations accompanying band nucleation in the upper end of gauge length at about 230 s, its growth till 75th pixel covering upper half of the gauge length and the nucleation of the second band from the lower end of the gauge length at 302 s which then covers the lower half of the gauge length. However, at any particular instant in the load plateau (254 s - 405 s),

thermal profiles are highly diffusive with temperature distributed over the entire gauge length thereby blurring the actual zone of strain localization.

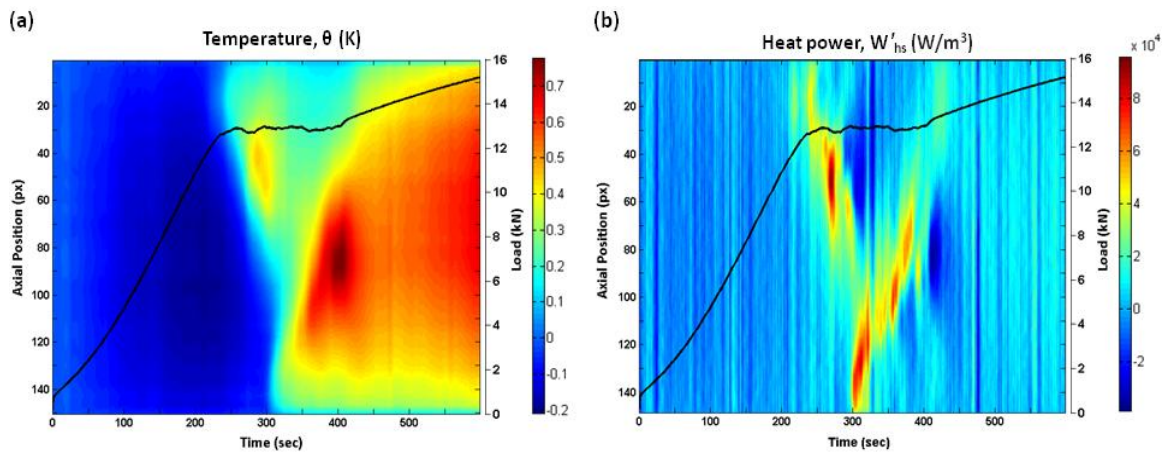


Figure 4.1 Spatiotemporal evolutions of (a) temperature and (b) heat power accompanying Lüders instability

Heat power evolutions estimated using heat equation shown in Fig. 4.1(b) precisely reveal the zones of strain localization associated with both the Lüders bands at any particular instant without the effect of diffusion. Nucleation of the first band is in fact clearly revealed by heat power evolutions much before the thermal evolutions at about 210 s itself. It can also be observed that the magnitude of heat evolutions in the load plateau is higher than in the strain hardening region. This is because, the load plateau involves very less plastic deformation during Lüders band nucleation and growth (associated with unlocking or generation of fresh dislocations) compared to the intense plastic deformation in the strain hardening region. Hence, the fraction of mechanical power dissipated as heat is relatively more in the load plateau.

The temporal variations of different terms of heat diffusion equation accompanying localized deformations during Lüders instability is shown in Fig. 4.2 from which it is observed that $d\theta/dt$ term contributes to the major portion of overall heat

power. The Laplacian term possesses significant magnitude, but the θ/τ term reflecting the heat losses due to convection and radiation is very less and almost negligible.

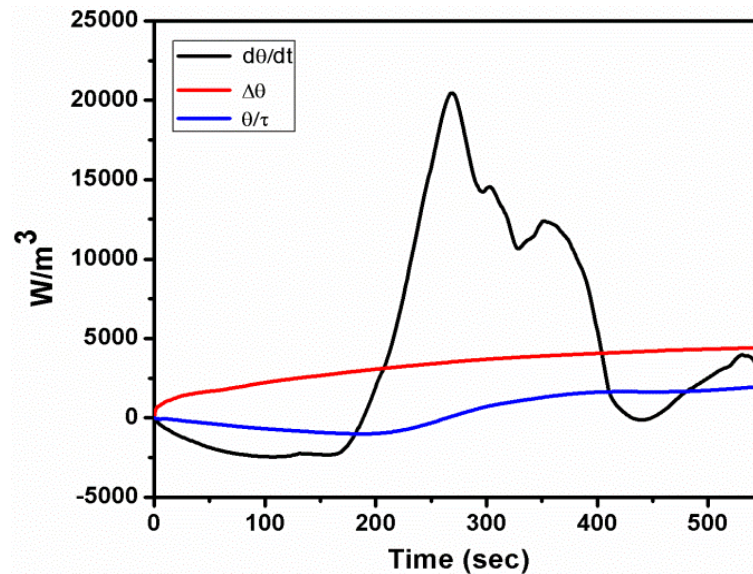


Figure 4.2 Temporal variations of different terms of heat diffusion equation accompanying Lüders Instability

Temporal evolutions of the average of heat power and temperature over the entire gauge length are shown in Fig. 4.3. Temperature initially decreases and reaches to a minimum at about 200 s due to thermoelastic effect, after which it increases rapidly in the load plateau involving Lüders band front propagation. In uniform strain hardening region, although increasing trend is followed, the slope of temperature decreases. Similar to temperature, heat power also increases rapidly from 200 s following the end of influence of thermoelasticity. In the load plateau, heat power clearly unravels the strain localization associated with the growth of two bands with two peaks. The first peak at 270 s is associated with the first band which deforms (yields) the upper half of gauge length and the second peak at 360 s is associated with the second band which deforms the lower half of the gauge length. It is to be noted that these heat power peaks do not correspond to the time of nucleation of the respective bands, but to a time instant where the average of heat

power over the gauge length is maximum during their growth. Such information on the strain localizations associated with the growth of two Lüders bands in the load plateau is not reflected in the temperature variations. This is because, at any instant of time, the thermal field not only possesses the temperature evolution corresponding to the strain localization at that instant, but also the thermal signatures of the previous strain localizations and the associated diffusion effects.

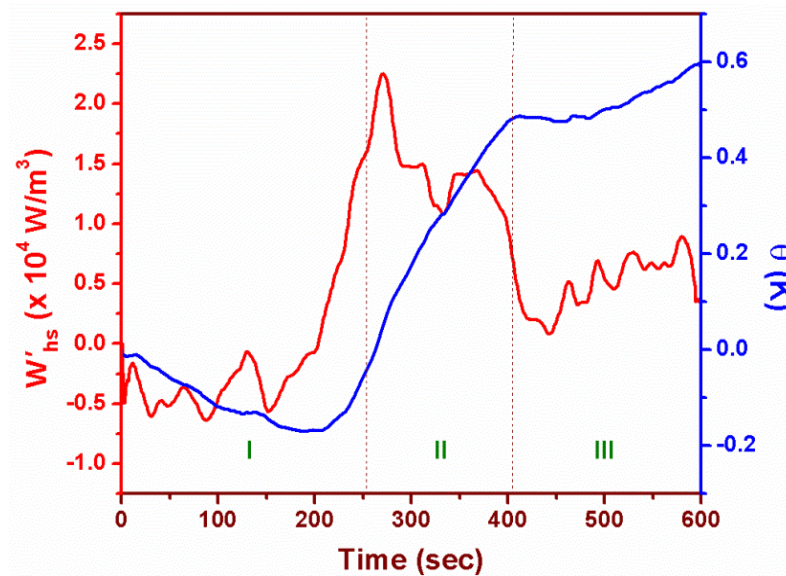


Figure 4.3 Temporal evolutions of heat power and temperature

4.4 Lüders band formation and growth in regions I and II

Figure 4.4 depicts the temperature, heat power, strain and strain rate fields of the complete gauge length of the specimen in region I of the load-time curve involving thermoelastic effect and microstrain evolution. At any particular time instant, images on the left of the first row are the thermal fields, θ with units as Kelvin K, and those on the right are the heat power fields, W'_{hs} with units as W/m^3 . In the second row, images on the left are the longitudinal strain fields, ϵ_{yy} (of the order of microns, μ) and those on the right are the strain rate fields, $\dot{\epsilon}_{yy}$ (μ) with units as per second. Temperature decreases due to thermoelastic effect and strain pattern fluctuates over the entire gauge length. On the other

hand, heat power is distributed over the entire gauge length representing uniform elastic deformation and negative manifesting the thermoelastic effect. Similar to strain, strain rate also fluctuates over the entire gauge length representing elastic deformation.

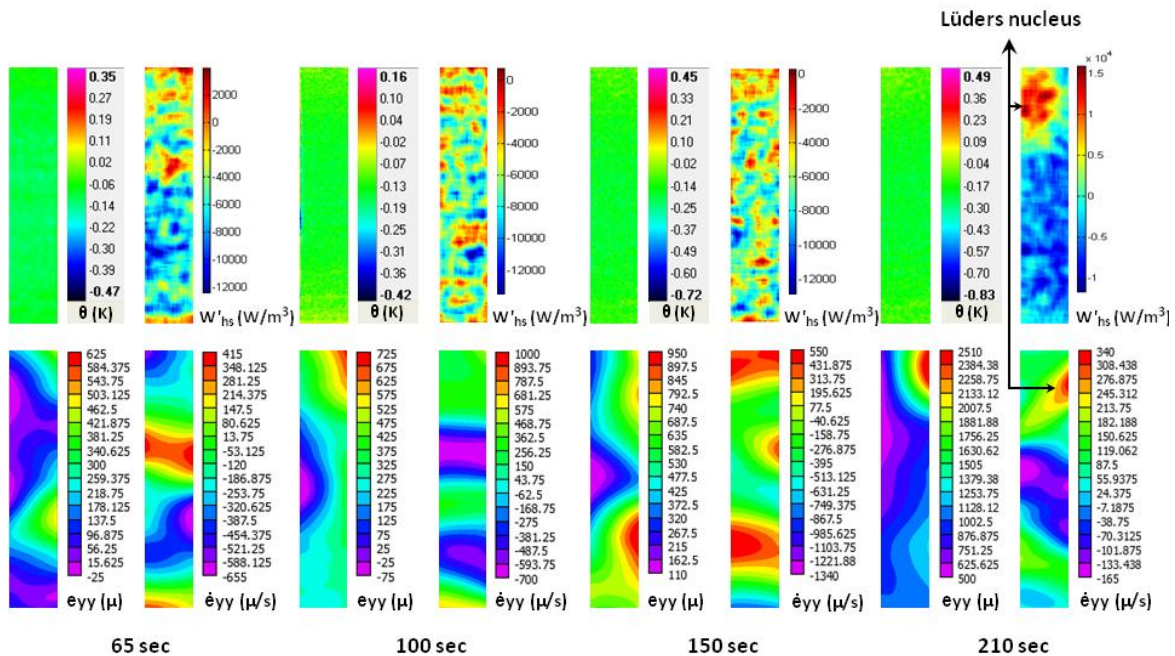


Figure 4.4 Thermoelastic regime and nucleation of Lüders band

With further increase in the load, at about 210 s, strain localization occurs in the upper end of the gauge length leading to nucleation of Lüders band as revealed by the corresponding heat power field in Fig. 4.4. It is from this instant that distributed heat powers and fluctuating strain rates become localized. Retrieving this information on band nucleation from the corresponding thermal field is difficult because of the effect of thermoelasticity that occurred in the immediate past. Although strain field reflects the Lüders band nucleation in the form of strain localization, it is only the strain rate field that clearly reveals the precise zone of plastic localization.

At 254th s where the macroscopic yield point is attained, fully developed Lüders band is formed as shown by the thermal, strain, heat power and strain rate fields in Fig. 4.5. Following the band formation, the band front propagates and covers the upper

half of the gauge length. This is then followed by the nucleation of second band from the lower end of the gauge length at 302 s and its growth along the gauge length as shown by the heat power fields in Fig. 4.5. On the other hand, the thermal imprint in the upper half of the gauge length left by the first band and the sustained effect of thermoelasticity in the lower half of the gauge length blurs the thermal information corresponding to the second band nucleation in the corresponding thermal field. Although strain field at this instant depicts the second band nucleation, associated plastic localization over the complete cross section of the specimen is revealed only by the strain rate field. Following this, second band front propagates towards the center of the gauge length in the interval of 330 s-360 s as shown by the thermal and strain fields in Fig. 4.5.

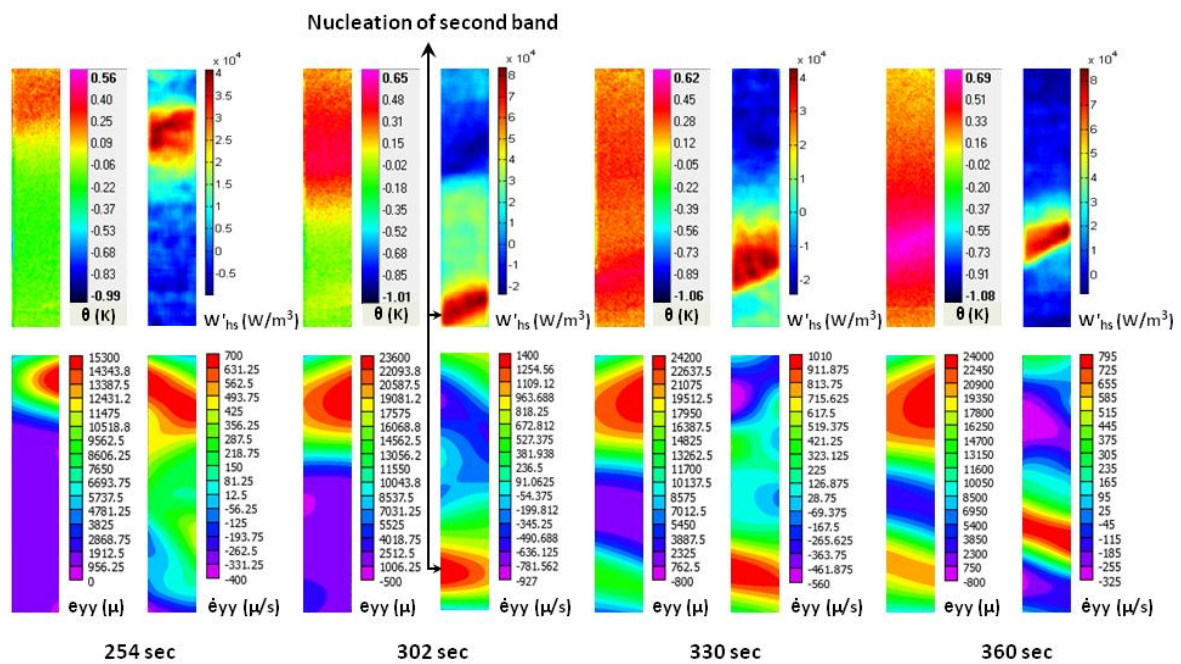


Figure 4.5 Growth of Lüders bands in the load plateau

Heat power and strain rate evolutions which are direct manifestations of deformation (and in turn the associated dislocation activities) are localized at the band front at any instant of time during the band growth (band front propagation). This is clearly in line with the mechanism of band growth proposed by Van Rooyen [102] that

elastic region in the immediate vicinity of the band front is yielded and included as a part of the band thereby leading to growth of the band or band front propagation. However, during nucleation and formation of the band (before band front propagation) heat power and strain rate are localized within the band admitting the deformation inside the band.

4.5 Delayed localized yielding in regions II and III

From the strain field at 375th s in Fig. 4.6 it can be deduced that although both the Lüders band fronts completely traversed the gauge length, zones close to either side of the center of the gauge length are not relatively yielded when compared to other zones. This indicates that these zones are not strained to the extent of full Lüders strain.

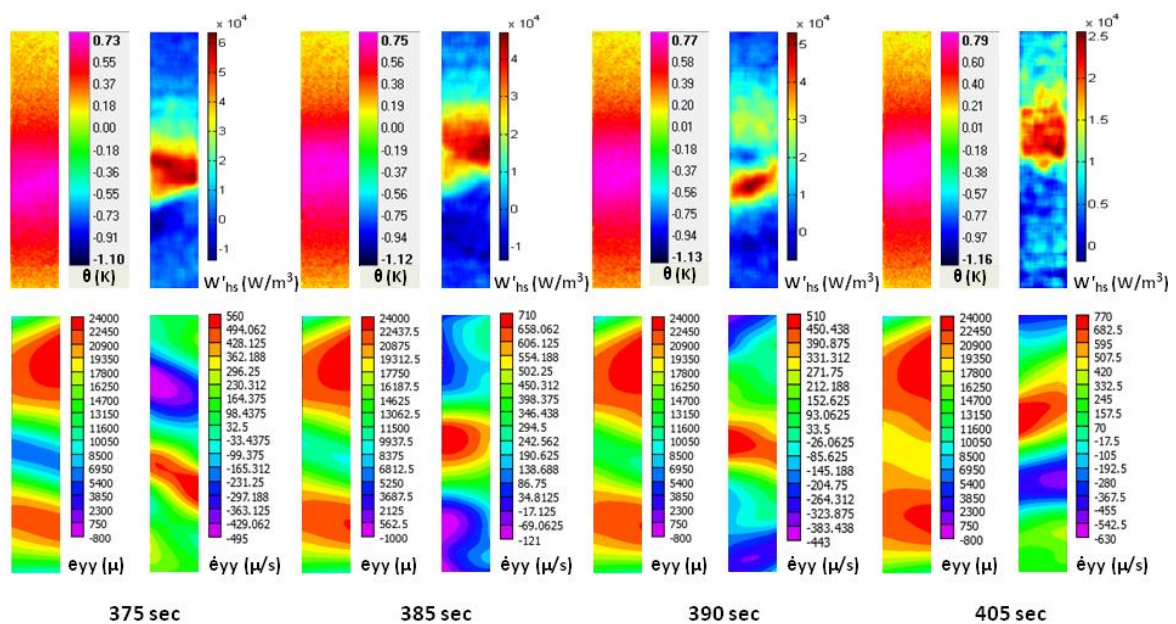


Figure 4.6 Delayed yielding in the end of the load plateau

Such difference in the magnitude of yielding experienced by the zones close to the center of the gauge length is not disclosed by the corresponding thermal field because of the diffusion effect associated with the temperature evolutions during band front propagations. From then onwards till the end of the load plateau, deformation is localized only in these zones close to the center of the gauge length as revealed by the localization of heat power

and strain rate in the interval of 375 s - 405 s in Fig. 4.6. The same can also be visualized from Fig. 4.1(b) where heat power evolutions are localized in the region covering 70th pixel to 85th pixel in the same interval. Such continuation of yielding in a region where band front has already propagated is referred to as delayed yielding. This is because some grains may yield and some may not or may undergo partial yielding when the band front propagates. Those grains, which have not yielded or partially yielded, undergo yielding to the extent of full Lüders strain after the band front propagation [143].

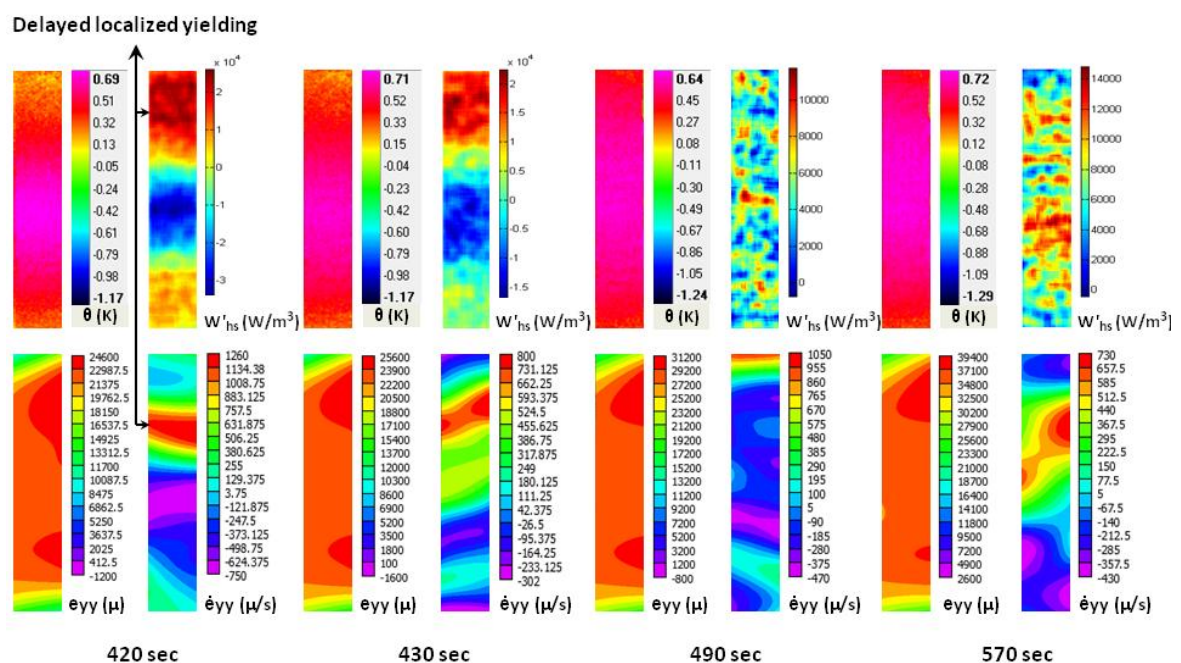


Figure 4.7 Delayed localized yielding and uniform strain hardening in region III

In the present study, it is also observed that such strain localization after band front propagation continues even during the initial stages of uniform strain hardening. The upper end of the gauge length where first band nucleated undergoes such delayed yielding as revealed by the localization of heat power and strain rate at 420 s and 430 s in Fig. 4.7. Strain localizations during the initial stages of strain hardening after Lüders band front propagation has also been reported earlier using strain gauges by Zhang and Jiang [101]. Such strain localizations during the initial stages of strain hardening are not reflected in

the thermal and strain fields because of the thermal and strain imprints associated with prior plastic localizations. The occurrence of delayed localized yielding can be also be visualized from Fig. 4.1 by comparing the thermal and heat evolutions in the first 35 pixels of the gauge length during the initial stages of strain hardening (region III).

As the load increases in the uniform strain hardening region, the specimen starts to deform uniformly with the manifestations of uniform temperature and strain distribution over the entire gauge length as shown in Fig 4.7. Reporting the occurrence of uniform deformation, heat powers are distributed and strain rate fluctuates over the entire gauge length of the specimen. However, unlike the elastic region, heat powers are positive with higher magnitudes representing plastic deformation. It is to be highlighted that strain rate evolutions complement the heat power evolutions in revealing both strain localizations and uniform deformation at any particular instant in the load-time curve.

4.6 Plastic, dissipated heat and stored powers accompanying Lüders instability

Figure 4.8 shows the variations of the externally applied mechanical, elastic and plastic powers in different regions of the load-time curve.

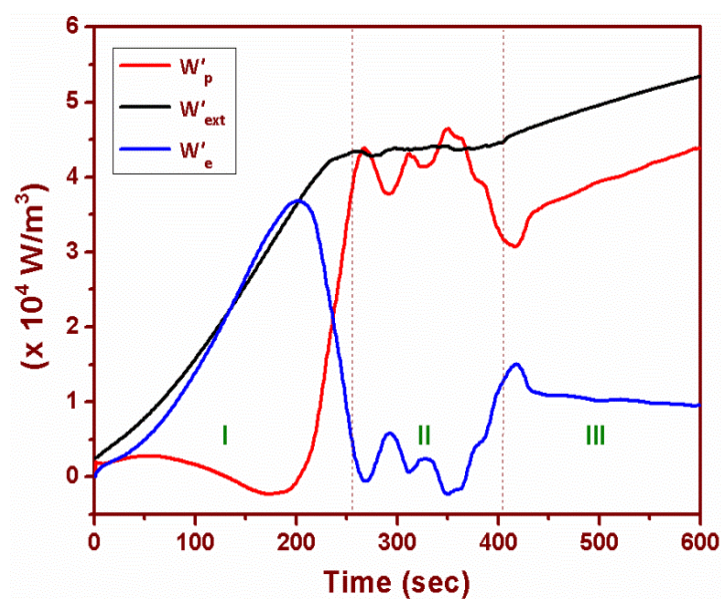


Figure 4.8 Characteristic variations of the mechanical, elastic and plastic powers

Applied mechanical power clearly reflects the elastic, yield plateau and the strain hardening region of the specimen. The nucleation of first and second band is revealed by the plastic power peaks at 254 s and 302 s respectively. Another peak at 350 s corresponds to the intense plastic localization accompanying the growth of the second band. Such localizations manifest with rapid drops in the elastic power variations. It is to be pointed out that although macroscopic yield point corresponds to 254th s, plastic power increases rapidly from 200th s itself following the end of thermoelasticity. In the uniform strain hardening region, plastic power increases and elastic power decreases as expected.

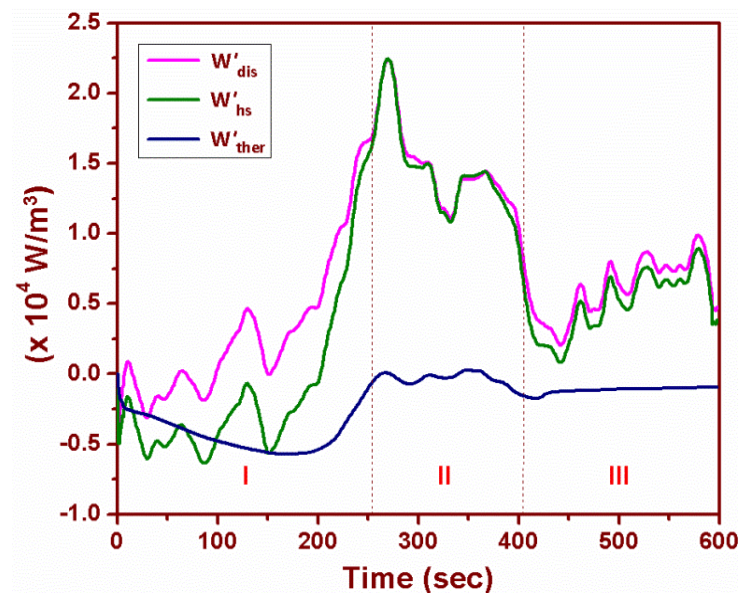


Figure 4.9 Characteristic variations of the overall heat, thermoelastic coupling and dissipative heat powers

Figure 4.9 shows the evolutions of heat power, thermoelastic coupling power and the dissipative heat power associated with external, elastic and plastic powers. The thermoelastic coupling power is relatively more in the load plateau than region III with a clear reflection of the localizations accompanying nucleation and growth of Lüders bands. Dissipative heat power is almost zero during the initial stages of the elastic region and on approaching 200th s (where thermoelastic effect becomes negligible and plastic power

evolves) it increases drastically following the same characteristics of the overall heat power in regions II and III. This conveys that the dissipative heat power estimated is purely a manifestation of the plastic deformation induced by Lüders bands without the elastic effects.

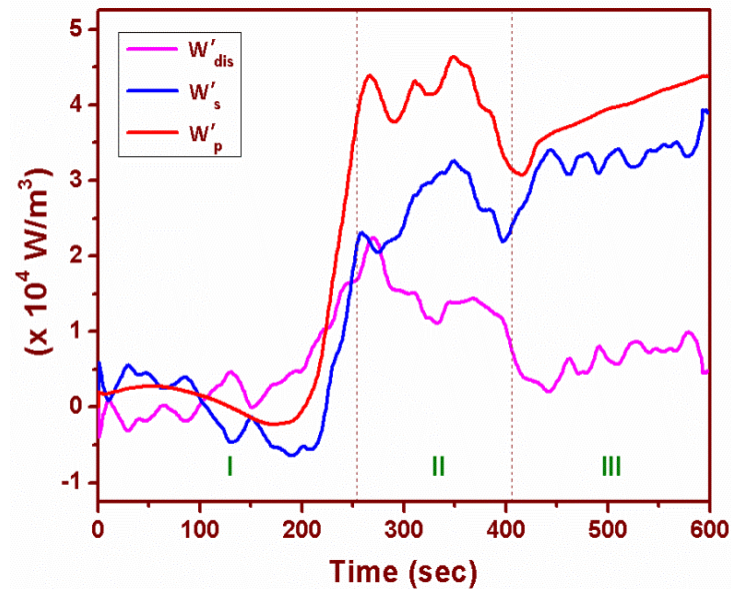


Figure 4.10 Characteristic variations of the plastic, dissipative heat and stored powers

Thermomechanical couplings accompanying Lüders instability investigated in the present work is shown in Fig. 4.10 through variations in the plastic, dissipative heat and the stored powers. Stored power which represents the rate of energy storage in the specimen is estimated as the difference between the plastic power and dissipative heat power as defined by Eq. (4.11). Since being a manifestation of the strain energy associated with dislocations, stored power decreases in the elastic region till 200 s, after which it increases rapidly representing the onset of plastic deformation. The stored power is found to be relatively higher during the growth of second band when compared to that of the first, trending opposite to that of the heat power variations. This conveys that plastic deformation experienced by the specimen during the growth of first band is less than that of the second band. In region III involving uniform strain hardening, stored power

increases since intense plastic deformation takes place. Having estimated the three thermomechanical parameters, calculation of energy conversion rate ratios can provide an insight into the fractional variation in the rate of energy conversion during strain localizations and uniform deformation.

4.7 Energy conversion rate ratios

Figure 4.11 depicts the variation of energy conversion rate ratios namely β_1 (fraction of plastic power converted into dissipated heat power) and β_2 (fraction of plastic power converted into stored power) from 225 s where the plastic power increases drastically. Both the ratios confess the strain localization associated with the growth of the two Lüders bands.

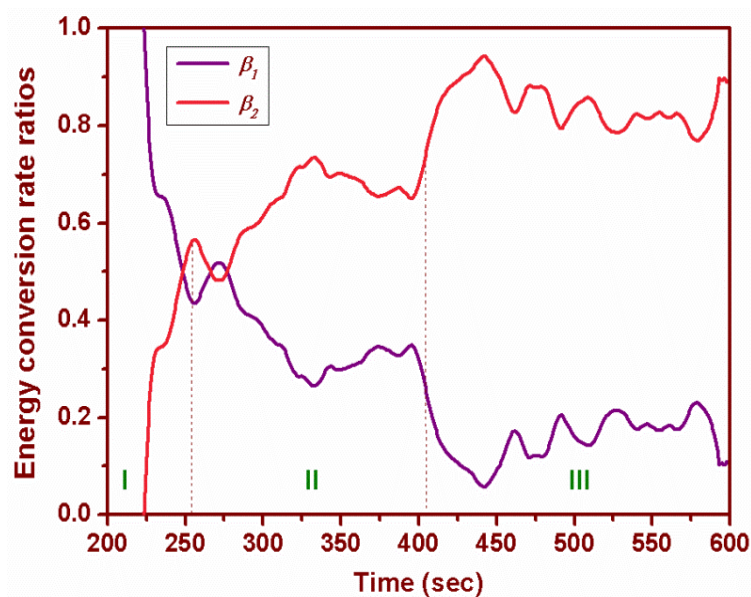


Figure 4.11 Characteristic variations of the energy conversion rate ratios

β_1 decreases with increase in plastic strain (or time) with slight increases at some instants depending on the intensity of plastic localizations in the load plateau and β_2 trends in an opposite manner. Initially β_1 drops to a small minimum at 254 s where β_2 peaks corresponding to nucleation of the first band. At this instant, 56 % of plastic power is converted into stored power and the remaining 44 % is dissipated as heat power.

Following this, intense heat dissipation takes place during the growth of the first band till 272 s at which 52 % of plastic power is dissipated as heat and the remaining 48 % is stored in the material. With further growth of the first band and formation of the second band, intense strain localization takes place until 330 s at which 26 % of acting plastic power is dissipated as heat and the remaining 76 % is stored in the material. From then on to till the end of the load plateau, β_1 increases and β_2 decreases although β_2 is greater than β_1 . Overall in the load plateau, fraction of plastic power stored in the specimen during second band formation and propagation is more than that of the first.

In region III, approximately 82 % of plastic power is stored and the remaining 18 % is dissipated as heat power conveying that most of the applied power is used in deforming the specimen plastically and very less is dissipated as heat. Although fraction of plastic power stored is mostly higher than the dissipative heat power, heat power dissipated is relatively more in the load plateau than the strain hardening region. It is to be noted that only in the interval of 266 s - 276 s involving strain localizations associated with the growth of first band, β_1 is more than β_2 .

The studies discussed in this chapter demonstrate the advantage of studying the strain localizations using heat power and strain rate variations without the influence of signatures of prior plastic localization. The Lüders band nucleation zones have been visualized in the heat power and strain rate fields much ahead of the thermal and strain fields. Heat power and strain rate evolutions accompanying the formation of Lüders band are localized within the band representing the deformation inside the band, whereas during band growth they are localized at the band fronts reflecting the occurrence of yielding in the elastic region close to the band front thereby experimentally validating the band growth mechanism proposed by Van Rooyen [102]. Heat power and strain rate evolutions also revealed the continuation of strain localization due to delayed localized yielding in the

end of load plateau and initial stages of uniform strain hardening which were not depicted by the thermal and strain evolutions. The difference in the magnitude of plastic deformation experienced by the specimen during the growth of different Lüders bands was clearly reflected by the variations in the stored power. Fraction of heat power dissipated is observed to be relatively more in the load plateau than the strain hardening region manifesting the lesser deformation experienced by the specimen through Lüders band development.

CHAPTER – 5

DISCONTINUOUS YIELDING BEHAVIOR OF WELDED MILD STEEL ACCOMPANYING LÜDERS INSTABILITY

Although significant works have been reported on various aspects of Lüders instability, studies on Lüders yielding behavior in a welded material involving stress concentrations at the interfaces of various local zones with dissimilar microstructures are very limited [149]. Romanova et al. [149] have simulated the yielding behavior of welded low carbon steel using finite difference method and observed that Lüders bands cease to propagate in the heat affected and weld zones. In other words, weld and heat affected zones have been reported to be undeformed (not yielded) by Lüders bands in the load plateau. Since weld and heat affected zones have microstructures that are dissimilar from that of the base metal, it is expected that the associated stress concentrations at the interfaces would strongly influence the microstrain evolutions in the elastic region and their localization leading to nucleation of Lüders band. Also, the dissimilar microstructures of welded mild steel would lead to differences in the deformation behavior of local zones in other regions of the load-time curve.

While the earlier chapters have focused on the application of IRT and DIC to study the Lüders phenomenon in plain specimens, this chapter would discuss the discontinuous deformation behavior of TIG welded mild steel accompanying Lüders deformation based on the associated thermomechanical couplings. Spatiotemporal evolutions of temperature, heat power, strain and strain rate are studied addressing the influence of stress concentrations at the interfaces of different zones with dissimilar microstructures on the

microstrain localization and Lüders band nucleation, band growth kinematics and the strain localization following band front propagation associated with delayed localized yielding. The difference in the deformation behavior of local zones of welded mild steel during Lüders band kinematics in the load plateau and uniform strain hardening is also quantified through characteristic variations of the thermomechanical parameters such as dissipative heat power, stored power and the energy conversion rate ratio.

5.1 Experimental

The tensile specimen used in this study was machined from TIG (Tungsten inert gas also called as Gas tungsten arc) welded IS 2062 grade E250 B mild steel using electro discharge machining (EDM) with weld direction perpendicular to the gauge length. Quasi static, monotonic, uniaxial tension test of the specimen (100 mm x 25 mm x 2.6 mm) with weld in the center of gauge length was performed at 8.3×10^{-4} /s strain rate with deformation being recorded simultaneously at 10 Hz frame rate using infrared and digital cameras. Prior to experimentation, the specimen is qualified through radiography to ensure absence of welding or machining induced defects as shown in Fig. 5.1.

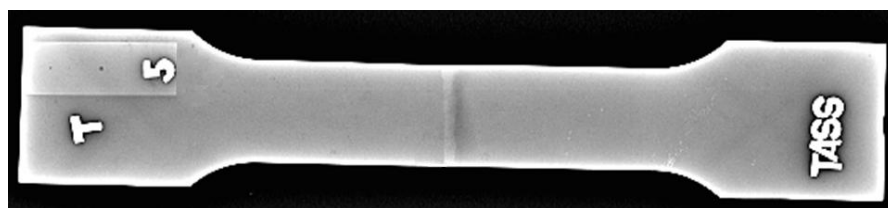


Figure 5.1 Radiograph of the tensile specimen welded in the center of the gauge length

The experimental setup, procedure for estimation of heat power and other thermomechanical parameters are the same as discussed in chapter 4. The spatial resolution achieved with the infrared and optical imaging systems are $625 \mu\text{m}$ and $185 \mu\text{m}$ respectively, for the focal distances set in this study. The subset size used for performing image correlation is 21×21 pixels. The local mechanical, elastic and thermoelastic

coupling powers are estimated using the local strain and strain rates obtained from DIC.

The local area for the estimation of the local stress any particular instant is given by:

$$A = A_0 \exp(-\varepsilon) \quad - (5.1)$$

where, A_0 is the initial area of cross section and ε the local strain.

5.2 Thermomechanical characterization

The hardness profile across the weld region of the specimen is shown in Fig. 5.2. From Fig. 5.2 the weld and heat affected zones are estimated to cover 6.25 mm of the total gauge length. Heat affected zone is observed to possess higher hardness because of the formation of bainite phase as shown by the optical micrograph in Fig. 5.3(b). The weld zone has hardness lower than the heat affected zone due to the formation of acicular ferrite phase (Fig. 5.3(c)), while the base metal with the ferrite and pearlite phases has the least hardness (Fig. 5.3(a)).

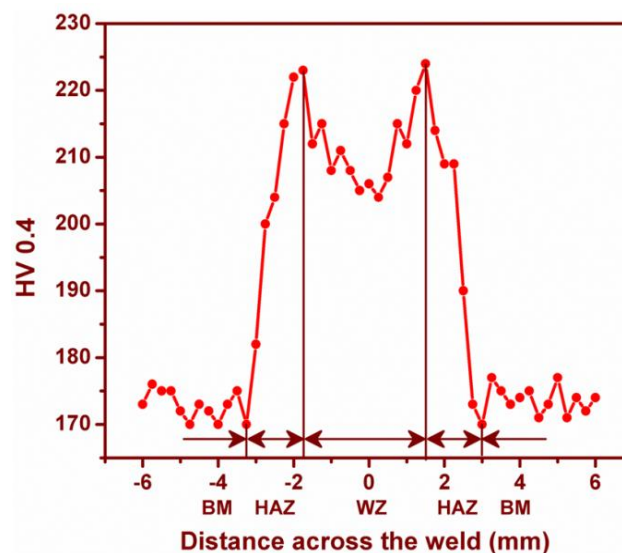


Figure 5.2 Hardness across the weld

Figure 5.4 depicts the spatiotemporal evolutions of (a) temperature, θ (K) and (b) heat power, W'_{hs} (W/m^3) superimposed to the load-time behavior of the specimen deformed at $8.3 \times 10^{-4}/s$ strain rate. The load plateau involving strain localizations accompanying

Lüders band kinematics is identified to be in the interval of 35 s - 67 s. Y axis of the contour plots represents the complete gauge length, the temperature and heat power evolutions over which are averaged along the gauge width at any particular instant and X axis represents time. The nucleation and growth kinematics of two Lüders bands initiated from either ends of the gauge length are reflected by both thermal and heat power evolutions as seen in Fig. 5.4. However, the zones of band nucleation are found to be revealed by heat power evolutions much ahead of the thermal evolutions without the thermal signatures of prior plastic localizations and the associated diffusion effects.

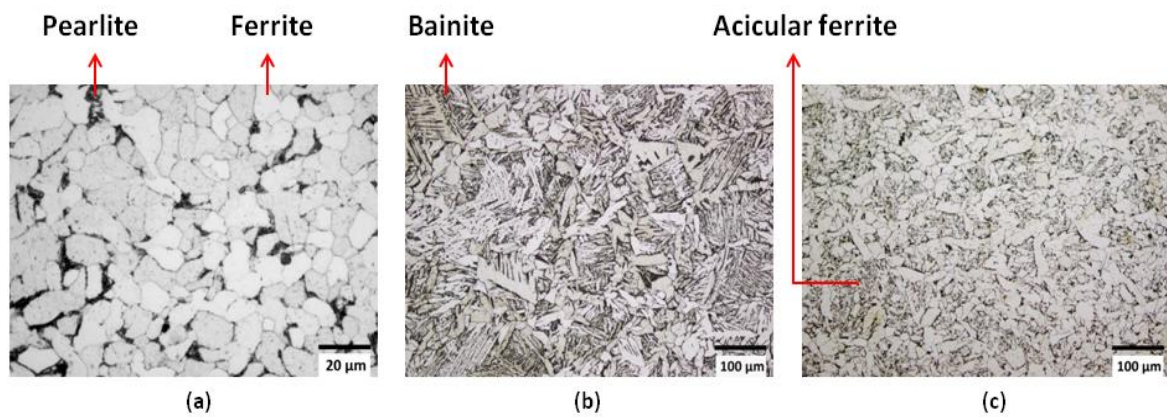


Figure 5.3 Optical micrographs of (a) base metal, (b) heat affected zone and (c) weld zone in the TIG welded mild steel

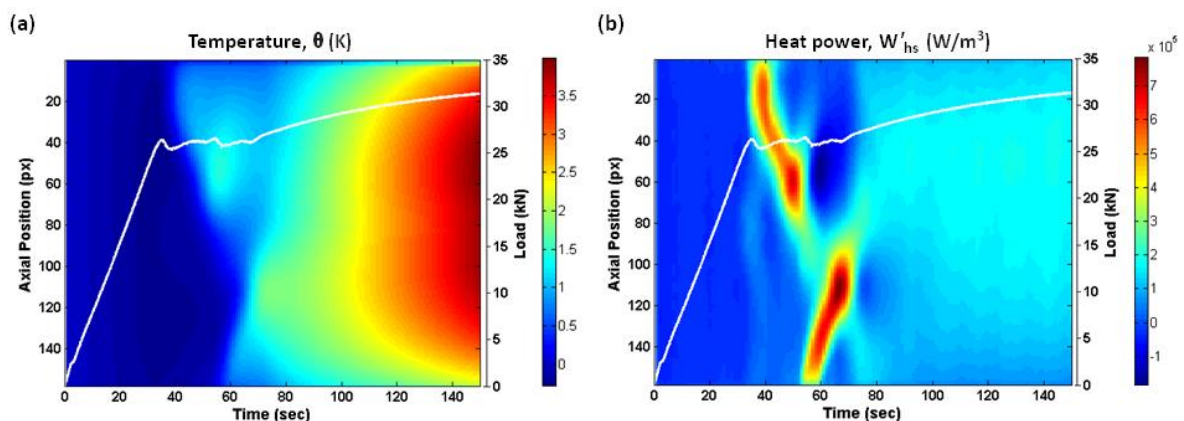


Figure 5.4 Spatiotemporal evolutions of (a) temperature and (b) heat power accompanying Lüders instability in TIG welded specimen

5.2.1 Nucleation and band growth kinematics

Figure 5.5 represents the evolution of temperature and heat power over the entire gauge length of the specimen during the nucleation and growth of Lüders bands. At 30th s, microstrain is localized in the center of the gauge length because of stress concentration in the weld induced by welding process and at the ends of gauge length (close to fillets) due to stress concentration induced by gripping which are manifested through heat power evolution in these zones as observed. The magnitude of heat power at the center of gauge length is more, reflecting the possibility of intense stress concentration leading to nucleation of Lüders band. However, the same information is not clearly reflected in the corresponding thermal field because of the thermoelastic effect.

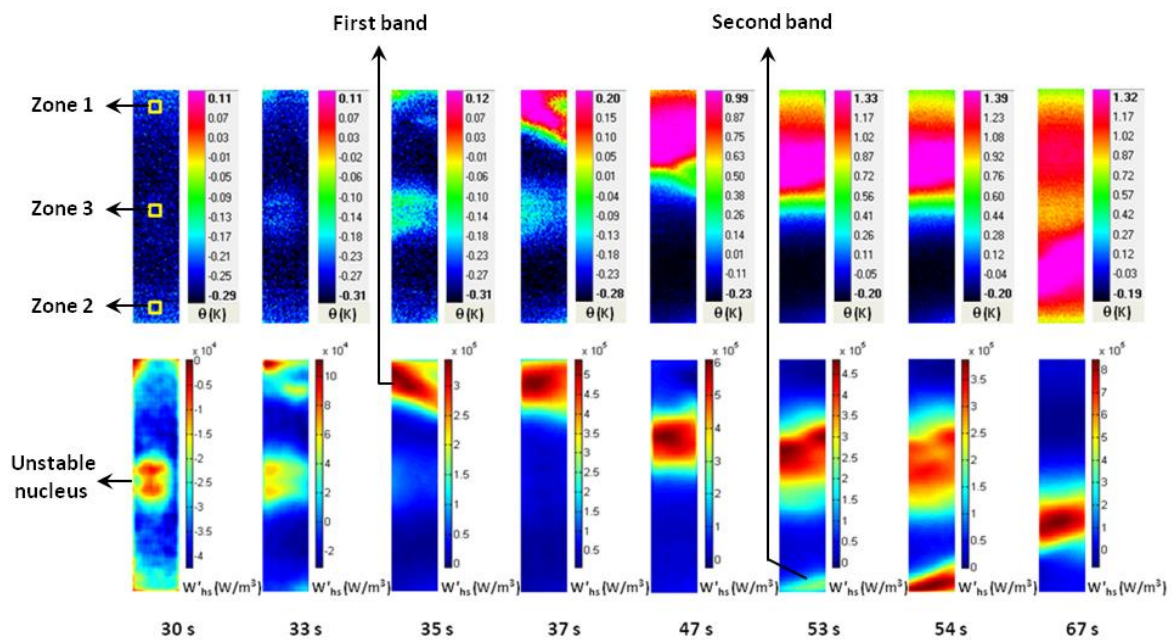


Figure 5.5 Spatial distribution of temperature and heat power accompanying Lüders band nucleation and growth

With further increase in load, nucleus in the center of the gauge length goes unstable and that from the upper end of gauge length develops as revealed by both thermal and heat power fields at 33 s. Nucleus later traverses the complete cross section

developing as a fully grown Lüders band at 35 s corresponding to the upper yield point. This conveys that with increase in load, stress concentration due to gripping builds up more than that of the weld zone, thereby making the upper end of gauge length as the favorable zone for plastic deformation through Lüders band. The band then yields (deforms) the gauge length by means of band front propagation (band growth). At 53 s, the band front covers the upper half of the gauge length with nucleation of second band taking place simultaneously from the lower end as observed in the heat power field. The nucleation of second band is not revealed by the corresponding thermal field due to the sustaining effect of thermoelasticity which masks the information. This is then followed by plastic localization in the lower half of the gauge length accompanying growth of the second band. At 67 s, corresponding to the end of the load plateau, the second band front traverses along the gauge length to some distance but not till the center of the gauge length.

By comparing the heat power fields at 53 s, 54 s and 67 s, it can be realized that from the center of the gauge length (in which weld and heat affected zones are present) to some distance towards the lower half of the gauge length, the magnitude of heat evolutions is relatively less. The same can be quantitatively analyzed from Fig. 5.4(b) where it can be observed that at 67th s corresponding to end of the load plateau, the magnitude of heat power from 76th pixel to 96th pixel covering the weld, heat affected zones with dissimilar microstructures and some portion of the lower base metal region is relatively lower. It is to be highlighted that heat power evolutions are relatively less influenced by thermoelasticity and reveal the plastic localization associated with the band growth (band front propagation) at any instant of time without the effect of signatures of prior plastic localization.

Figure 5.6 represents the strain fields ϵ_{yy} and strain rate fields $\dot{\epsilon}_{yy}$ (of the order of microns, μ) of complete gauge length accompanying Lüders bands nucleation and growth. Although nucleation of Lüders bands in the center, upper and lower ends of the gauge length at 30 s, 35 s and 53 s respectively is depicted in both strain and strain rate fields, localization over the complete cross section at any instant of time is revealed only by the strain rate fields without the effect of the track record of prior strain localizations. Strain field at 67 s clearly reveals that the lower half of the gauge length has yielded relatively lesser in comparison with that of the upper half while lowest strain at the center of the gauge length. Strain rate evolutions in the center of the gauge length and zones adjacent to it in the lower half of gauge length are also observed to be very less, which confirms that these regions have undergone very less deformation. The lower magnitude of heat power and strain rate evolutions in the center of the gauge length is because of the presence of the bainite phase in the weld zone and acicular ferrite in heat affected zone which have relatively higher mechanical property when compared to that of the base metal ferrite.

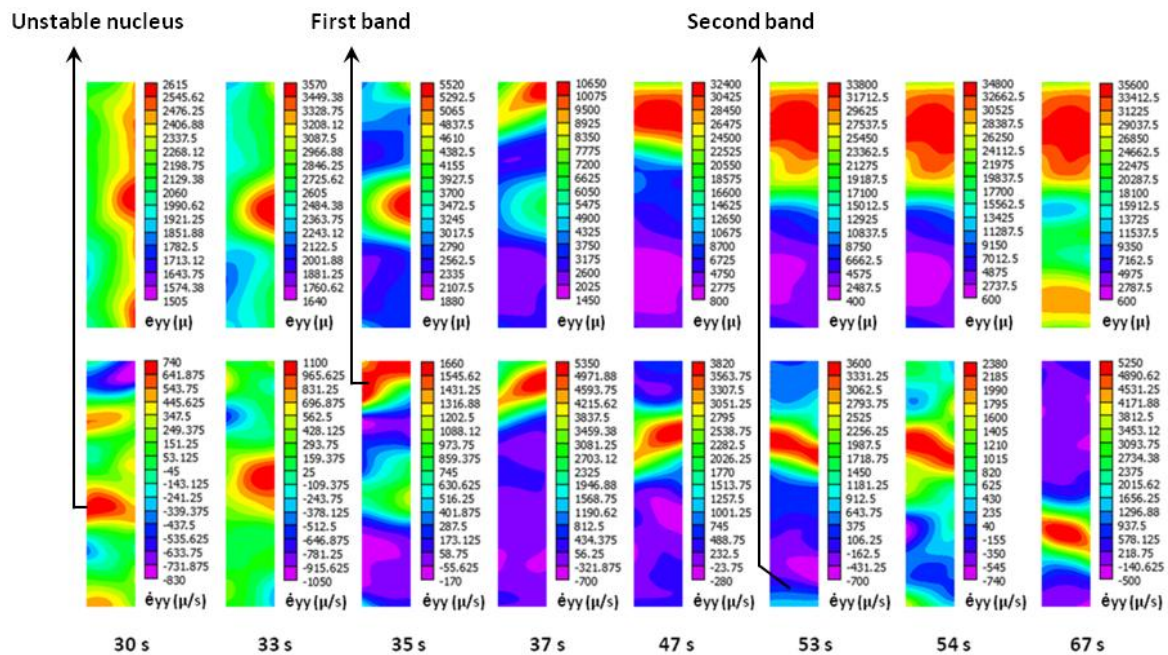


Figure 5.6 Spatial distribution of strain and strain rate accompanying Lüders band nucleation and growth

5.2.2 Uniform strain hardening

Figure 5.7 depicts the thermal and heat power fields in the uniform strain hardening region where it is expected to have uniform temperature and heat evolutions over the complete gauge length.

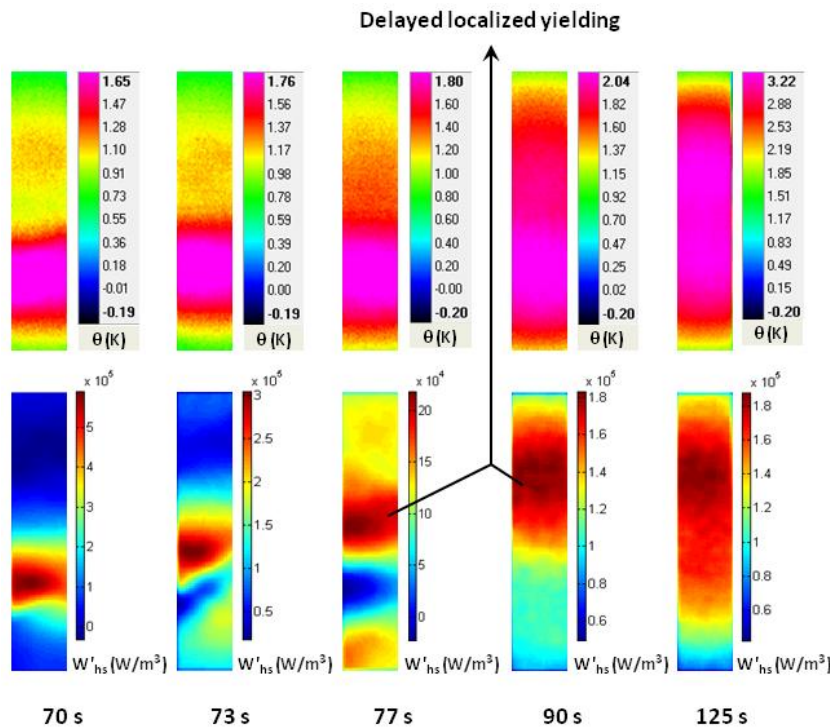


Figure 5.7 Temperature and heat power fields in the initial stages of strain hardening

Localized heat power evolutions is found to continue in the uniform strain hardening region from the same zone of localization at the end of the load plateau as revealed by the heat power fields in the interval of 70 s - 73 s. Although temperature is localized in the lower half of the gauge length, the precise zone of plastic localization is not depicted in the temperature fields due to the effect of thermal diffusion. This is then followed by localization in the upper half of the gauge length till 90 s where band front has already propagated. Such type of plastic localization is due to delayed localized yielding described in the chapter 4. Following this, heat power evolves over the entire gauge length manifesting uniform plastic deformation as seen at 125 s in Fig. 5.7. On the other hand,

strain rate localizes in the same fashion as that of heat power during the initial stages of strain hardening complementing the information revealed by the heat power evolutions as seen in Fig. 5.8. Finally, after 125 s it fluctuates over the complete gauge length manifesting the uniform plastic deformation experienced by the specimen.

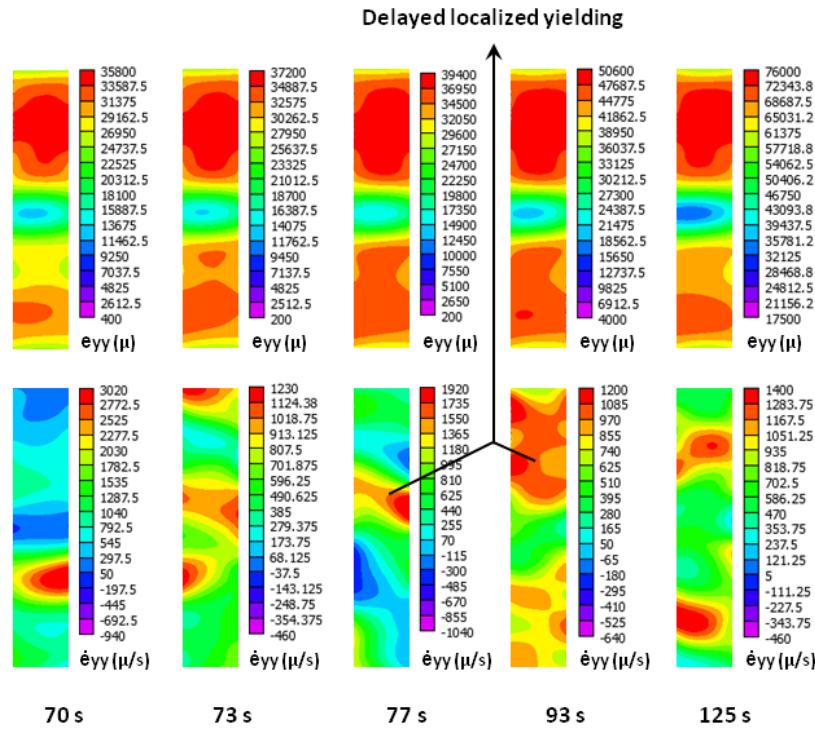


Figure 5.8 Strain and strain rate fields in the initial stages of strain hardening

5.2.3 Local variations of temperature, heat power, strain and strain rate

The temporal evolutions of temperature, heat power, strain and strain rate in different local zones along the gauge length are shown in Fig. 5.9. Three local zones, namely, zone 1 (base metal), zone 2 (base metal) and zone 3 (encompassing weld and heat affect zone) marked in the thermal field at 30th s in Fig. 5.5 are considered. From Fig. 5.9(a) it is observed that temperature initially decreases to a minimum on all the zones till 32 s due to thermoelastic effect, after which it increases in zone 3 corresponding to the nucleation of unstable band as revealed by heat power fields in Fig. 5.5. This is then followed by rapid increase of temperature in zone 1 accompanying the formation and

growth of the first stable Lüders band where temperature saturates to about 0.89 K at 44 s, after which it increases in zone 3 as the band front approaches the center of the gauge length. The formation of second band in the lower end of the gauge length manifests with substantial increase of temperature in zone 2 at 53 s as seen in Fig. 5.9(a). In the uniform strain hardening region, the temperature increases rapidly in all the local zones with highest value in zone 3 (encompassing weld and heat affected zones).

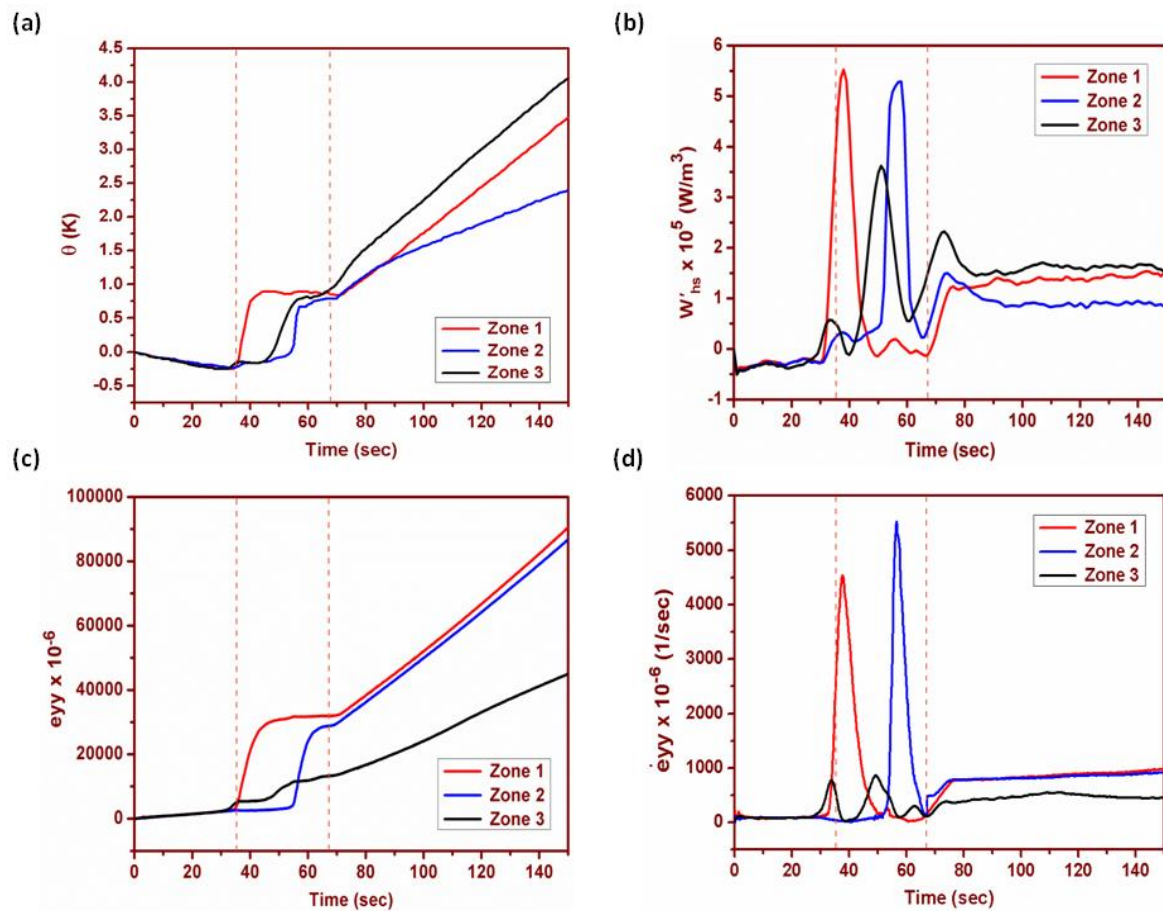


Figure 5.9 Temporal evolutions of (a) temperature, (b) heat power, (c) strain and (d) strain rate on the local zones

On the other hand, heat power increases rapidly in the zone 3 from 27 s itself revealing the plastic localization associated with the formation of unstable band as seen in Fig. 5.9(b). Formation of the first stable band in the zone 1 is revealed through drastic heat power evolution at 31 s itself, which is much ahead of the corresponding temperature

evolutions. This is then followed by heat evolutions in the zones 3 and 2 associated with propagation of first band front to the center of the gauge length and the formation and growth of second band. During uniform strain hardening, i.e. after 67 s, heat evolutions in all the local zones are very less when compared to that of the load plateau. This is because, deformation is now distributed over the entire gauge length and hence mechanical power experienced by the considered local zones is less and in turn the heat power evolutions are also lesser. Similar to temperature, heat evolutions in zone 3 are higher than other local zones during strain hardening.

Strain evolutions in all the local zones are observed to follow the same trend as that of thermal evolutions in the load plateau as shown in Fig. 5.9(c). Formation of unstable band, first stable band and second band at 32 s, 35 s and 53 s respectively are manifested with rapid strain evolutions in the corresponding zones. After the formation of first stable band in zone 1, strain evolutions associated with the unstable band nucleation in zone 3 saturates conveying that material no more yields in this zone. Strain in zone 3 again evolves when the first band front approaches close to the center of the gauge length at 44 s. From this it is clear that the area under the two heat power peaks in Fig. 5.9(b) for zone 3 at 33 s and 50 s have deformations associated. However, for the third peak at 73 s there are not much significant strain evolutions. The possibility of complete transfer of acting power into heat power is more at this instant which can be confirmed through estimation of fraction of acting plastic power converted into heat and stored powers.

On the other hand, strain rate evolutions are found to confirm all the plastic localizations revealed by the heat power variations in all the local zones in the load plateau as observed in Fig. 5.9(d). It is to be noted that strain and strain rate experienced by the zone 3 (encompassing weld and heat affected zones) during strain hardening is very less in comparison with that of other zones, trending opposite to that of temperature and heat

power evolutions. Also, no significant strain rate evolution is observed corresponding to the heat power peak at 73 s where plastic strain localization was earlier doubtful using strain variations. The difference in the deformation behavior of local zones observed during Lüders band kinematics and uniform strain hardening using heat power and strain rate evolutions can be confirmed by analyzing the energy balances involved in each region of the load-time curve on all these zones which is described in the next section.

5.2.4 Local variations of the thermomechanical parameters

The variation of thermomechanical parameters such as plastic power (W'_p), dissipative heat power (W'_{dis}) and stored power (W'_s) in all the local zones are shown in Fig. 5.10. Plastic power in zone 1 is initially zero during elastic deformation and then increases drastically from 31 s itself following the end of thermoelastic effect, although macroscopic yield point corresponds to 35 s as seen in Fig. 5.10(a). Corresponding dissipative heat and stored powers in this zone also increase from 31 s as a manifestation of the formation of first stable band following the same characteristic variations as that of plastic power. At the end of the load plateau, plastic power again increases in this zone due to delayed yielding characterized with significant evolutions of stored power from 63 s. However, the corresponding heat power evolutions are very less at this instant and become prominent only after 68 s (i.e. during initial stages of strain hardening). Such localization in the zone 1 during the initial stages of uniform strain hardening can also be visualized through careful examination of the heat power field at 73 s in Fig. 5.7.

In zone 2, the plastic, dissipative heat and stored powers increase from 53 s and peak at 57 s corresponding to the formation and growth of second band in this zone as seen in Fig. 5.10(b). It is to be noticed that during the formation and growth of first band in zone 1, no plastic power acts in zone 2 and hence no heat or stored powers evolve.

These observations confirm that the two heat power peaks at 37 s and 57 s for zone 1 and 2 respectively in Fig. 5.9(b) during Lüders band growth have plastic strain localizations associated. In zone 3, plastic power and the associated dissipative heat and stored powers increase from 26 s corresponding to the nucleation of unstable band as shown in Fig. 5.10(c). Heat power evolutions due to this nucleation are observed to be very less and stored power has a remarkable evolution revealing the intense strain localization (deformation) associated.

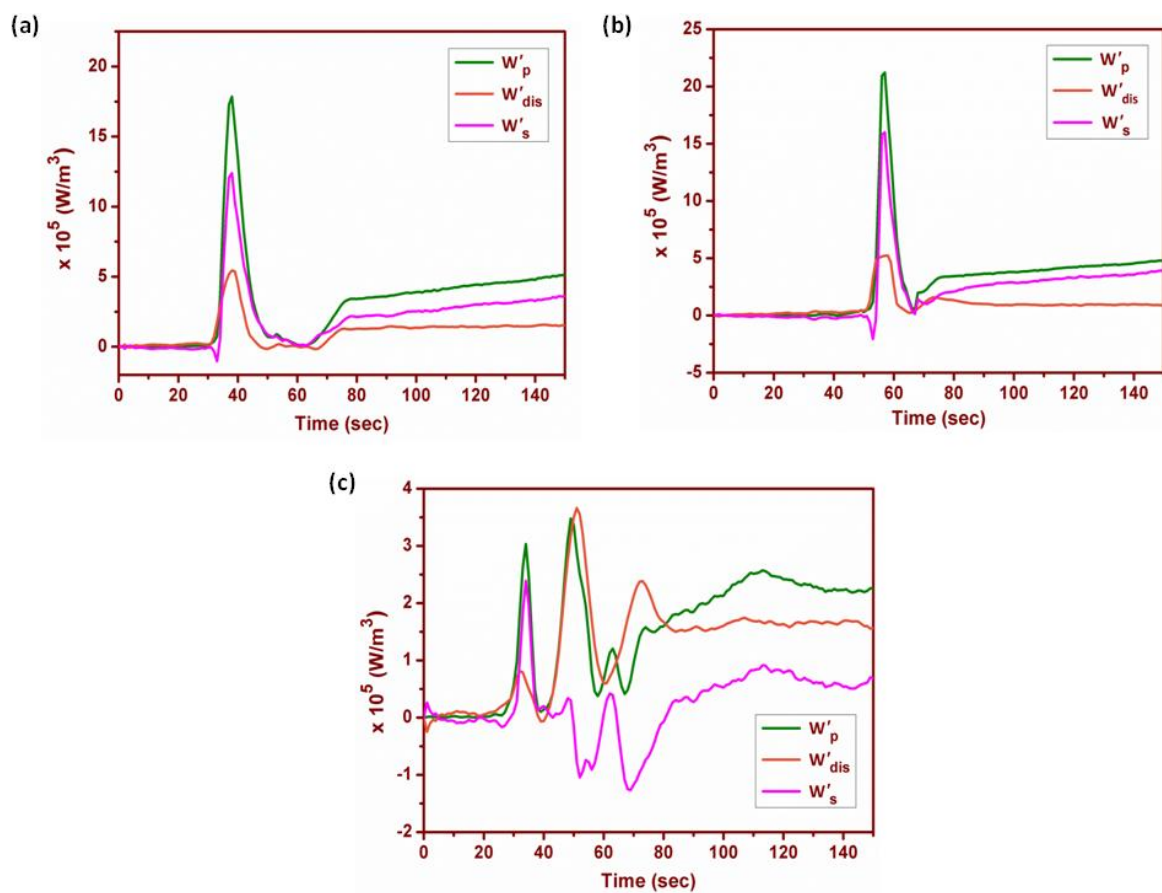


Figure 5.10 Variation of thermomechanical parameters in (a) zone1, (b) zone 2, and (c) zone 3

Although plastic power in zone 3 is significant in the interval of 41 s to 67 s, the corresponding stored power is very less (almost zero) and the dissipative power is equal to or some times more than the plastic power. Hence, zone 3 (encompassing weld and heat

affected zones) experiences significant deformation only during the unstable nucleation, whereas during band front propagations from either end of gauge length in the load plateau plastic strain experienced is very less. In other words, acting plastic power in zone 3 in the interval of 41 s to 67 s is not sufficient to yield this zone significantly through band front propagations. This is because of the bainite and acicular ferrite phases in the weld and heat affected zones encompassing zone 3 which have higher yield strength compared to the ferrite phase present in the base metal zones 1 and 2. At time instants corresponding to mild evolutions of stored power in zone 3, strain rate also evolves as observed in Fig. 5.9(d). During uniform deformation in the strain hardening region, heat power evolutions are more than the stored power unlike other base metal zones (zone 1 and 2). Also, plastic power and the associated dissipative heat and stored powers in zone 3 are very less in magnitude when compared to zones 1 and 2.

5.2.5 Energy conversion rate ratio

The fraction of mechanical power converted into stored power (β_{diff}) in the considered local zones is shown in Fig. 5.11. The variation of β_{diff} in each zone is plotted from an instant at which plastic power evolves in it. In zone 1, β_{diff} increases drastically since the inception of plastic power. Although plastic power acts in this zone only till 49 s, significant values of β_{diff} observed till the end of the load plateau (67 s) is because of the conversion of very small magnitude of plastic power to stored power acting on this zone after 49 s. In zone 2, β_{diff} increases from 53 s associated with the nucleation and growth of second band and significant till the end of the load plateau. It is to be noted that the value of β_{diff} in zones 1 and 2 is almost the same (~ 0.8) when they experience deformations through band kinematics in their respective intervals. In zone 3, the initial negative value of β_{diff} is because dissipative power is more than the plastic power, i.e. rate of heat dissipation is more than the deformation energy rate. As time proceeds, β_{diff} evolves and

becomes significant as a result of the nucleation of unstable band in this zone. The positive values of β_{diff} at selected instants in the interval of 45 s - 50 s and 60 s - 65 s confirm the mild deformations experienced by the zone 3 during the approach of the bands fronts towards it.

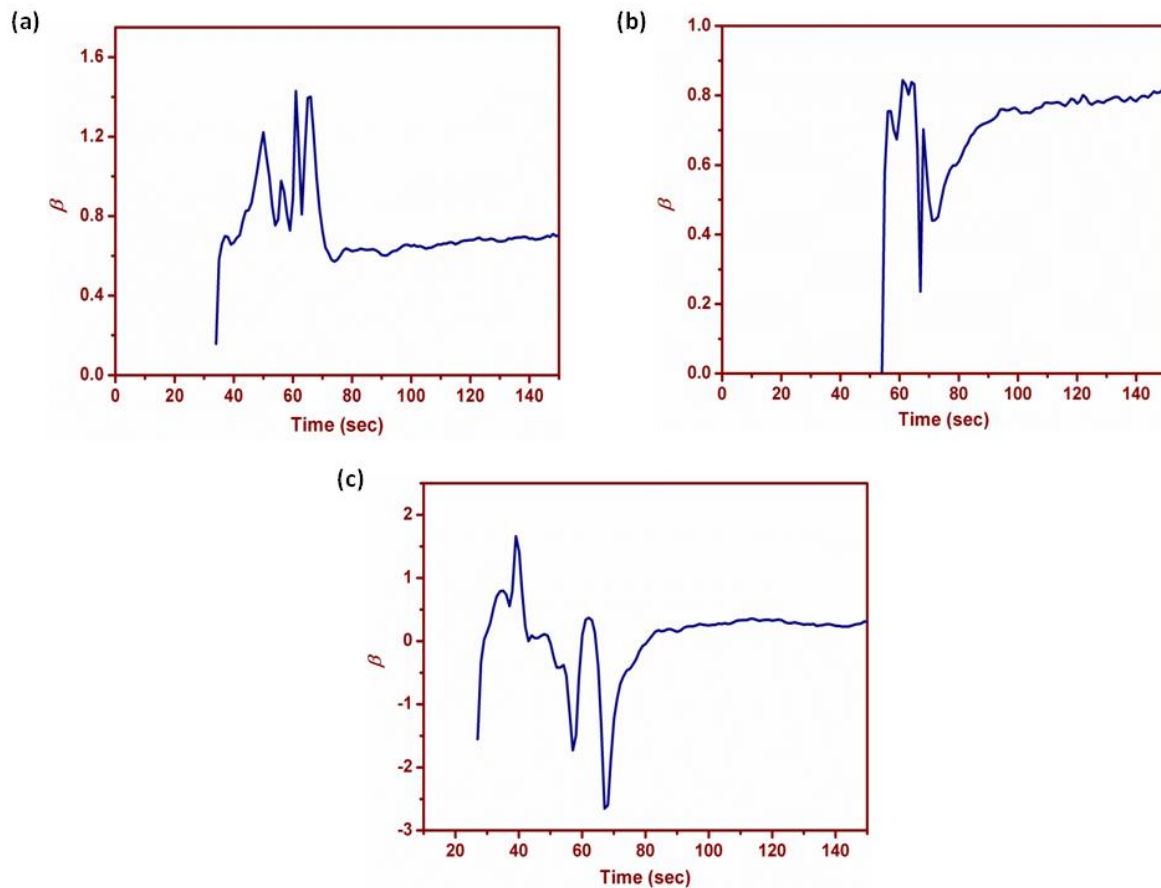


Figure 5.11 Variations of β_{diff} in (a) zone 1, (b) zone 2 and (c) zone 3

Generally, β_{diff} during strain hardening (involving very intense plastic deformation) will be more than that of the load plateau. In the present study, β_{diff} during strain hardening in all the local zones is either comparable or less than that of the load plateau. This is because, the rate at which material is deformed for the smaller magnitude of acting plastic power in the considered local zones becomes less as the material now undergoes uniform deformation with plastic power distributed over the entire gauge length. Among the local zones, zone 3 (weld and heat affected zones) has the least value of β_{diff} in the strain

hardening region conveying the they undergo very less deformation because of the presence of bainite and acicular ferrite phases.

In this study, deformation behavior of welded mild steel accompanying Lüders instability is characterized using the associated thermomechanical responses. Although thermal and strain fields reveal that Lüders bands cease to propagate in the weld and heat affected zones (leaving them undeformed), heat power and strain rate evolutions demonstrate the mild yielding of these zones in the load plateau. Estimated stored power and energy conversion rate ratio confirm the yielding experienced by weld and heat affected zones through unstable and stable Lüders bands. The plastic power and the associated dissipative heat and stored powers in the zone encompassing weld and heat affected zones have been found to be relatively very less because of the presence of bainite and acicular ferrite phases which have relatively higher yield strength compared to the base metal ferrite. From this study, it is also clear that localized heat power evolutions need not be accompanied by strain localizations as there is possibility for complete conversion of acting plastic power into heat power especially when a material with dissimilar microstructures is considered.

CHAPTER – 6

SUMMARY, CONCLUSIONS, HIGHLIGHTS, CONTRIBUTIONS AND FUTURE DIRECTIONS

6.1 Summary and Conclusions

This dissertation describes a study in which Infrared thermal imaging and Digital image correlation have been applied simultaneously to study the inhomogeneous deformation behavior of IS 2062 grade E250 B mild steel exhibiting Lüders instability while subjected to tensile loading. Such steels are widely used as structural materials in many industries including strategic industries like nuclear. Prior to experimentation, all the specimens were qualified through complementary NDE methods such as radiography and visual testing to ensure absence of defects which can otherwise result in erroneous interpretations. During experimentation, appropriate precautions were taken to minimize the effects of background radiations and fluctuations in the ambient temperature, which are potential sources of noise in temperature measurements. Adequate care was also taken to ensure a distributed high contrast random dot pattern on the specimen surface using matt spray paints and no fluctuations in the illuminated light intensity. The results obtained clearly highlight the potential advantage of multi modal NDE - in this case the combined application of IRT and DIC in providing greater insights and enhanced understanding on the Lüders phenomenon through correlation of macroscopic thermomechanical responses to the microscopic dislocation activities. It also helped in validating the existing models on the nucleation and growth aspects of Lüders bands. Some of the significant observations in each of the chapters are summarized below.

In chapter 3, the critical areas of Lüders deformation were studied using temperature and strain fields. In the elastic region, a uniform decrease in temperature due to thermoelastic effect and discontinuous (fluctuating) but self organized microstrain evolutions were observed. The thermoelastic effect has been found to mask the temperature evolutions corresponding to microstrain localizations initially, after which temperature and strain evolutions are rapid in the stress concentration zone reflecting the rapid generation of dislocations. These are in line with the microstructural observations of Suits [70] and P. J. Worthington et al. [76]. It is also confirmed through visualization that at upper yield stress, nucleus is no more a nucleus, but traverses the complete cross section at an angle developing as a fully grown band. This correlates with the reports by D.W. Moon [75] based on microstructural observations. The similarity of observed fluctuating strain evolutions in the elastic region to that of fluctuating strain rate evolutions reported by Mudrock et al [141] intuitively conveys that for any plastic instability phenomenon (static - Lüders bands or dynamic strain ageing - PLC bands) the microplastic behavior during the initial stages of elastic deformation is almost similar. The present study also reveals the potential of IRT and DIC techniques in providing better visualization of the zone of band formation much ahead of the upper yield point.

Thermal and strain evolutions associated with the nucleation and development of the Lüders band before macroscopic yield point clearly demonstrated the band formation behavior which is in line with band formation mechanism proposed by Friedel [142]. The inhomogeneity in the thermal-strain distribution measured across the band front using IRT and DIC has been found to be partially in line with the inhomogeneity in stress-strain distribution proposed by Van Rooyen [102]. The reason for any mismatch of the measured thermal-strain distribution with the stress-strain distribution defined by the model has been discussed considering not only the theoretical aspects of the model, but also other practical

considerations such as experimental conditions and limitations of the techniques used. Experimental results have also led to the first of its kind observations such as the symmetry in strain distribution on either side of nucleation zone and strain evolutions much before band front which were not predicted by the model. It has been observed that for a particular specimen thickness, the effective width of Lüders band is not constant in the load plateau. Active zone has been observed to increase irregularly. Instances with no change in active zone when effective width changes and vice versa are also observed. These observations confirm that the two stages of Lüders band growth mechanism, namely, yielding and work hardening may not be successive and if successive will not generally compensate each other to the same magnitude of region within the band reflecting the irregularity involved in their occurrence. The studies carried out also revealed that strain rate varies in the active zone and always peaks in the effective width of Lüders band.

In chapter 4, heat power and strain rate evolutions accompanying Lüders deformation were estimated for gaining better clarity on the kinematics of localization without the influence of signatures of prior plastic localizations. The band nucleation zones were observed in the heat power and strain rate fields much ahead of the thermal and strain fields. In the elastic and uniform strain hardening regions, heat power and strain rate were distributed with peak strain rate fluctuating over the complete gauge length manifesting the uniform elastic and plastic deformations, whereas in the load plateau, they are localized revealing the plastic localizations accompanying Lüders bands precisely. During the formation of Lüders band, heat power and strain rate were localized within the band representing the deformation inside the band, whereas during band growth they are localized at the band fronts conveying the occurrence of yielding in the elastic region close to the band front thereby experimentally validating the band growth mechanism proposed

by Van Rooyen [102]. The continuation of strain localizations due to delayed localized yielding in the end of load plateau and initial stages of uniform strain hardening which were not revealed by the thermal and strain evolutions has been successfully studied using heat power and strain rate evolutions. Plastic, dissipative heat and stored powers were almost zero till the end of thermoelastic effect, after which they increased drastically marking the onset of strain localizations accompanying nucleation and growth of Lüders bands. The variations in the stored power clearly revealed the difference in plastic deformation experienced by the specimen during the growth of two different Lüders bands. Although fraction of plastic power stored was mostly higher than the dissipative heat power, heat power dissipated was found to be relatively more in the load plateau than the strain hardening region conveying that specimen experiences lesser deformation during the Lüders band kinematics in the load plateau.

In chapter 5, discontinuous yielding behavior of TIG welded mild steel accompanying Lüders instability was studied based on the associated thermomechanical responses. Unlike the plain specimens, Lüders band was found to nucleate in the zone encompassing weld and heat affected zones due to the stress concentrations associated. However, this nucleation was later observed to become unstable following which stable bands from the fillets of the specimen yield the gauge length as a result of buildup of stress concentrations in the fillets when macroscopic yield point is attained. Thermal and strain fields which are influenced by the signatures of prior plastic localization showed that Lüders band fronts cease to propagate in the weld and heat affected zones. This observation is in line with the simulation results of Ramanova et al. [149]. However, the estimated heat power and strain rate evolutions revealed mild plastic strain localizations in the zone encompassing weld and heat affected zones during the growth of Lüders bands in the load plateau. Significant evolution of stored power accompanying unstable band

nucleation close to elastic-plastic transition of the load-time curve revealed the deformation experienced by the weld and heat affected zones. Also, the estimated stored power and the differential Taylor-Quinney coefficient confirmed the mild yielding of the weld and heat affected zones through band front propagations in the load plateau. The plastic power acting in the zone encompassing weld and heat affected zones and the associated dissipative heat and stored powers have been found to be less in comparison with that of other zones because of the presence of bainite and acicular ferrite phases. For the same reason, fraction of plastic power dissipated as heat was observed to be higher in this zone during strain hardening unlike the base metal zones. This study has also proved that localization of heat power not necessarily be accompanied by strain localization, where the possibility of complete conversion of acting plastic power into heat is also more especially when a material with dissimilar microstructures is studied.

6.2 Highlights

The primary focus of this dissertation has been on the substantial areas of interest such as microstrain localization leading to Lüders band nucleation, deformations of the local zones within the Lüders band which constitutes to the band growth, stress-strain-strain rate distributions across the band front and delayed localized yielding etc. *The study on the correlation of the macroscopic thermal and strain responses to the microstrain evolution and localization leading to the Lüders band nucleation is one of the first of its type. Also, the insights provided on the band growth mechanism based on the measurements of the magnitude of local zones of Lüders band using DIC is yet another unique work of this thesis.* In addition to the studies carried out using temperature and strain variations, heat power and strain rate evolutions have also been estimated for quantitative analysis of the kinematics of localization accompanying Lüders deformation without the influence of signatures of prior plastic localization. *Using the heat power and*

strain rate evolutions, the occurrence of delayed localized yielding in the end of the load plateau and initial stages of uniform strain hardening has been successfully studied and visualized for the first time. The other important highlight of this dissertation is the understanding that is achieved on the difference in the fractional dissociation of acting plastic power into dissipative heat and stored powers during Lüders band nucleation and growth in the load plateau and uniform strain hardening. *The study on the discontinuous yielding behavior of welded mild steel under influence of dissimilar microstructures on the nucleation and growth behavior of Lüders bands is yet another benchmark study of this dissertation. Also, for the first time, the difference in yielding behavior of local zones of welded mild steel during Lüders band kinematics in the load plateau and uniform deformation in the strain hardening region has been studied and quantified through characteristic variations of the thermomechanical parameters such as dissipative heat power, stored power and the energy conversion rate ratio.*

It is to be also highlighted that all the above mentioned significant observations have been published in peer reviewed international journals with good impact factors.

6.3 Contributions

Some of the major contributions of this dissertation are briefed below

- ❖ The proposed models and concepts on the Lüders band formation and stress-strain distribution across the band has been experimentally validated with additional insights which were not predicted by the models.
- ❖ The deformation of local zones within the Lüders band studied using image correlation has led to understanding the irregularity in the occurrences of two stages of band growth mechanism.

- ❖ An insight into the nature of Lüders yielding behavior of TIG welded mild steel with dissimilar mechanical properties across the weld has been provided.
- ❖ The continuation of strain localization due to delayed localized yielding at the end of the load plateau and initial stages of uniform strain hardening has been experimentally demonstrated and visualized.
- ❖ The fractional rate of energy conversions studied in both plain and welded mild steel revealed the strain softening/hardening behavior of the material during instability in the plastic flow, globally as well as on local zones.

6.4 Future directions

It is well known that modeling, simulation, calibration and systematic experimentation are the keys to successful research and technology development. In science, any work is still a start in itself, as more puzzles and queries are thrown up as one delves deeper in the quest for excellence. While the focused studies in this thesis have significantly contributed in gaining newer insights, validating many of the propounded theories and correlating observations by other international researchers on some of the important aspects of Lüders instability, there is still scope for further research. Some of the possible areas which can be explored include:

- ❖ The Lüders yielding behavior during biaxial and multi axial loading conditions and other types of testing such as compression, shear and torsion or combinations of these. This would provide more realistic insights into the Lüders deformation behavior in an industrial structural component and the associated band characteristics.
- ❖ The effect of various cross sections of the specimen on the Lüders band characteristics. Since plastic instabilities are strongly influenced by strain ageing, application of IRT and DIC can play a crucial role in revealing the effect of

interrupted loading on the band characteristics such as band front velocity, orientation, upper and lower yield stresses and Lüders strain etc.

- ❖ The thermomechanical response across the Lüders band at the grain scale by achieving high spatial resolution in a local region, which would provide an insight into the micro mechanisms involved in band growth. High spatial resolution in a local region can be achieved by using high magnification lenses coupled with infrared and optical cameras. However, this setup needs the grain size of the material at least in the order of 1-3 mm.
- ❖ The coupled characterization using SEM-DIC-EBSD setup where the image correlation can be performed on the captured SEM images during in situ tensile testing of materials. Also, electron backscatter diffraction (EBSD) can be carried out on the same field view of the specimen. The EBSD pattern when overlaid on the strain map would help in quantifying the kinematics of microstrain and their localization leading to Lüders band nucleation. The inhomogeneity in stress-strain distribution across the Lüders band and the occurrence of delayed localized yielding can be understood in terms of slip activities at the grain scale.
- ❖ The effect of temperature, which strongly influences the plastic instabilities in materials by modifying the diffusion of dislocations and thereby the locking-unlocking mechanism. Performing high temperature experiments which are generally performed in a closed chamber could be relatively challenging. Provisions for recording the infrared and digital images of the surface of the specimen can be made using glass windows which are transparent to IR and visible radiations. Also, high temperature spray paints must be used for making black coating and random dot pattern on the specimen surface.

References

- [1] H. Yi, G.E. Hicho, R.J. Fields. Infrared measurement of heating and cooling emissions in aluminium and steel during tensile and cyclic loading. *Chin. J. Met. Sci. Tech.* 6 (1990) 106-111.
- [2] B. Venkatraman, C.K. Mukhophadyay, Baldev Raj. Effect of variation of strain rate on thermal and acoustic emission during tensile deformation of nuclear grade AISI type 316 stainless steel. *Mat. Sci. Tech.* 20 (2004) 1-7.
- [3] B. Venkatraman, C.K. Mukhophadyay, Baldev Raj. Prediction of tensile failure of 316 stainless steel using infrared thermography. *Exp. Tech.* 28 (2004) 35-38.
- [4] B. Venkatraman, Baldev Raj, C.K. Mukhophadyay. *J. Korean. Soc. NDT.* 22 (2002) 609-620.
- [5] W. Tong. Detection of plastic deformation patterns in a binary alloy. *Exp. Mech.* 37 (1997) 452-459.
- [6] M.M. Kutin, S.S. Ristic, M.R. Prvulovic, M.M. Prokolab, N.M. Markovic, M.R. Radosavijevic. Application of thermography during tensile testing of butt welded joints. *FME Trans.* 39 (2011) 133-138.
- [7] C. Leitao, I. Galvao, R.M. Leal, D.M. Rodrigues. Determination of local constitutive properties of aluminium friction stir weld using digital image correlation. *Mater. Des.* 33 (2012) 69-74.
- [8] B.L. Boyce, P.L. Reu, C.V. Robino. The constitutive behavior of laser welds in 304L stainless steel determined by digital image correlation. *Metall. Mater. Trans. A* 37A (2006) 2481-2492.
- [9] M. Kartal, R. Molak, M. Turski, S. Gungor, M.E. Fitzpatrick, L. Edwards. Determination of weld metal mechanical properties utilizing novel tensile testing methods. *Appl. Mech. Mater.* 7-8 (2007) 127-132.

-
- [10] A.P. Reynolds, F. Duvall. Digital image correlation for determination of weld and base metal constitutive behavior. *Welding Res. Supplement* 10 (1999) 355-360.
- [11] H. Louche, P. Vacher, R. Arrieux. Thermal observation associated with the Portevin- Le Chatelier effect in an Al-Mg alloy. *Mater. Sci. Eng. A*, 404 (2005) 188-196.
- [12] J. Zdunek, T. Brynk, J. Mizera, Z. Pakiela, K.J. Kurzydowski. Digital image correlation investigation of Portevin- Le Chatelier effect in an aluminium alloy. *Mater. Charact.* 59 (2008) 1429-1433.
- [13] L. Chen, H.S. Kim, S. Kyu, B.C. De Cooman. Localized deformation due to Portevin- Le Chatelier effect in 18 Mn-06C TWIP austenitic steel. *ISIJ Inter.* 47 (2007) 1804-1812.
- [14] G. Scavino, C.D. Salvo, P. Matteis, R.Sesana, D. Firrao. Portevin-Le Chatelier effects in a High-Mn austenitic steel. *Metall. Mater. Trans. A* 44A (2013) 787-792.
- [15] H. Louche, K. Bouabdallah, P. Vacher, T. Coudert, P. Balland. Kinematic fields and acoustic emission observations associated with the Portevin-Le Chatelier effect on an Al-Mg alloy. *Exp. Mech.* 48 (2008) 741-751.
- [16] P.D. Zavattieri, V. Savic, L.G. Hector Jr, J.R. Fekete, W. Tong, Y. Xuan. Spatio-temporal characteristic of the Portevin-Le Chatelier effect in austenitic steel with twinning induced plasticity. *Int. J. Plast.* 25 (2009) 2298-2330.
- [17] H. Ait-Amokhtar, C. Fressengeas S. Boudrahem. The dynamics of Portevin-Le Chatelier bands in an Al-Mg alloy from infrared thermography. *Mater. Sci. Eng. A*, 488 (2008) 540-546.
- [18] L. Casarotto, H. Dierke, R. Tutsch, H. Neuhauser. On nucleation and propagation of PLC bands in an Al-3Mg alloy. *Mater. Sci. Eng. A* 527 (2009) 132-140.

-
- [19] C. Bernard, J. Coer, H. Laurent, P. Chauvelon, P.Y. Manach. Relations between local strain jumps and temperature bursts due to the Portevin-Le Chatelier effect in an Al-Mg alloy. *Exp. Mech.* 53 (2013) 1025-1032.
- [20] A. Benallal, T. Berstad, T. Borvik, O.S. Hopperstad, I. Koutiri, R. Nogueira de Codes. An experimental and numerical investigation of the behaviour of AA5083 aluminium alloy in presence of the Portevin-Le Chatelier effect. *Int. J. Plast.* 24 (2008) 1916-1945.
- [21] D. Favier, H. Louche, P. Schlosser, L. Orgeas, P. Vacher, L. Debove. Homogeneous and heterogeneous deformation mechanisms in an austenitic polycrystalline Ti-50.8 at. % Ni thin tube under tension. Investigation via temperature and strain fields measurements. *Acta Mater.* 55 (2007) 5310-5322.
- [22] S. Daly, A. Miller, G. Ravichandran, K. Bhattacharya. An experimental investigation of crack initiation in thin sheets of Nitinol. *Acta Mater.* 55 (2007) 6322-6330.
- [23] S. Daly, D. Rittel, K. Bhattacharya, G. Ravichandran. Large deformation of Nitinol under shear dominant loading. *Exp. Mech.* 49 (2009) 225-233.
- [24] R.F. Hamilton, H. Sehitoglu, K. Aslantas, C. Efstathiou, H.J. Maier. Inter-martensite strain evolution in NiMnGa single crystals. *Acta Mater.* 56 (2008) 2231-2236.
- [25] W.S. Farren, G.I. Taylor. The heat developed during plastic extension of metals. *Proc. Roy. Soc. Series A* 107 (1925) 422-451.
- [26] G.I. Taylor, H. Quinney. The latent heat remaining in a metal after cold work. *Proc. Roy. Soc. Series A* 143 (1934)307-326.
- [27] W. Oliferuk, S.P. Gadaj. Energy storage during the tensile deformation of armco iron and austenitic steel. *Mater. Sci. Eng.* 70 (1985) 131-141.

-
- [28] W. Oliferuk, A. Korbel, M.W. Grabski. Mode of deformation and the rate of energy storage during uniaxial tensile deformation of austenitic steel. *Mater. Sci. Eng. A* 220 (1996)123-128.
- [29] R. Kapoor, N.S. Nemat. Determination of temperature rise during high strain rate deformation. *Mech. Mater.* 27 (1998) 1-12.
- [30] D. Macdougall. Determination of the plastic work converted to heat using radiometry. *Exp. Mech.* 40 (2000) 298-306.
- [31] W. Oliferuk, M. Maj, B. Raniecki. Experimental analysis of energy storage rate components during tensile deformation of polycrystals. *Mater. Sci. Eng. A* 374 (2004) 77-81.
- [32] J.J. Mason, A.J. Rosakis, G. Ravichandran. On the strain and strain rate dependence of the fraction of plastic work converted in to heat: an experimental study using high speed infrared detectors and the Kolsky bar. *Mech. Mater.* 17 (1994) 135-145.
- [33] A.T. Zehnder, E. Babinsky, T. Palmer. Hybrid method for determining the fraction of plastic work converted to heat. *Exp. Mech.* 38 (1998) 295-302.
- [34] J. Hodowany, G. Ravichandran, A.J. Rosakis, P. Rosakis. Partition of plastic work into heat and stored energy in metals. *Exp. Mech.* 40 (2000) 113-123.
- [35] D. Rittel. On the conversion of plastic work to heat during high rate deformation of glassy polymers. *Mech. Mater.* 31 (1999) 131-139.
- [36] G. Ravichandran, A. Rosakis, J. Hodowany, P. Rosakis. On the conversion of plastic work into heat during high strain rate deformation. *AIP Conference Proceedings* 620 (2002) 557-562.

-
- [37] H. Louche, L. Tabourot. Experimental energetic balance associated to the deformation of an aluminium multycrystal and monocrystal sheet. *Mater. Sci. Forum* 467-470 (2004) 1395-1400.
- [38] A. Chrysocoos, B. Wattrisse, J.M. Muracciole, Y.E. Kaim. Fields of stored energy associated with localized necking of steel. *J. Mech. Mater. Struct.* 4 (2009) 245-262.
- [39] A.M. Ivanov, E.S. Lukin. Investigation of the stored energy change of steel Fe360 subjected to equal-channel angular pressing. *Mater. Sci. Eng. A* 503 (2009) 45-47.
- [40] A. Rusinek, J.R. Klepaczko. Experiments on heat generated during plastic deformation and stored energy for TRIP steels. *Mater. Des.* 30 (2009) 35-48.
- [41] T. Chan, D. Backman, R. Bos, T. Sears, I. Brooks, U. Erb. In situ heat generation and strain localization of polycrystalline nanocrystalline nickel. *Thermomechanics and Infrared imaging* 7 (2011) 17-22.
- [42] D. Rittel, A.A. Kidane, M. Alkhader, A. Venkert, P. Landau, G. Ravichandran. On the dynamically stored energy of cold work in pure single crystal and polycrystalline copper. *Acta Mater.* 60 (2012) 3709-3728.
- [43] A.Y. Fedorova, M.V. Bannikov, O.A. Plekhov. A study of the stored energy in titanium under deformation and failure using infrared data. *Fract. Struct. Integ.* 24 (2013) 81-88.
- [44] A. Chrysochoos, B. Berthel, F. Latourte, A. Galtier, S. Pagano, B. Wattrisse. Local energy analysis of high cycle fatigue using digital image correlation and infrared thermography. *J. Strain. Anal. Eng. Des.* 43 (2008) 411-422.
- [45] A. Chrysochoos. Thermomechanical analysis of the cyclic behavior of materials. *Procedia IUTAM* 4 (2012) 15-26.
-

-
- [46] T. Pottier, F. Toussaint, H. Louche, P. Vacher. Inelastic heat fraction estimation from two successive mechanical and thermal analyses and full-field measurements. *Euro. J. Mech. A/Solids* 38 (2013) 1-11.
- [47] A. Benaarbiaa, A. Chrysochoos, G. Robert. Kinetics of stored and dissipated energies associated with cyclic loadings of dry polyamide 6.6 specimens. *Polym. Test.* 34 (2014) 155-167.
- [48] M.P. Luong. Fatigue limit evaluation of metals using an infrared thermographic technique. *Mech. Mater.* 28 (1998) 155-163.
- [49] G.L. Rosa, A. Risitano. Thermographic methodology for rapid determination of the fatigue limit of materials and mechanical components. *Int. J. Fatigue* 22 (2000) 65-73.
- [50] J.C. Krapez, D. Pacou, G. Gardette. Lock-in thermography and fatigue limit of metals. *Proc. QIRT2000* (2000) 277-282.
- [51] T. Boulanger, A. Chrysochoos, C. Mabru, A. Galtier. Calorimetric analysis of dissipative and thermoelastic effects associated with the fatigue behavior of steels. *Int. J. Fatigue.* 26 (2004) 221-229.
- [52] B. Berthel, B. Wattrisse, A. Chrysochoos, A. Galtier. Thermographic analysis of fatigue dissipation properties of steel sheets. *Strain.* 43 (2007) 273-279.
- [53] A.E. Morabito, A. Chrysochoos, V. Dattoma, U. Galietti. Analysis of thermoelastic and dissipative effects related to the fatigue of 2024 T3 aluminium alloy. *QIRT 1* (2004) 99-116.
- [54] M.L. Pastor, X. Balandraud, M. Grediac, J.L. Robert. Applying infrared thermography to study the heating of 2024-T3 aluminium specimens under fatigue loading. *Infrared Phys. Technol.* 51 (2008) 505-515.

-
- [55] A.Y. Fedorova, M.V. Bannikov, O.A. Plekhov. Infrared thermography study of the fatigue crack propagation. *Fract. Struct. Integ.* 21 (2012) 46-53.
- [56] T. Pottier, M.P. Moutrille, J.B. Le Cam, X. Balandraud, M. Grediac. Study on the use of motion compensation techniques to determine heat sources. Application to large deformations on cracked rubber specimens. *Exp. Mech.* 49 (2009) 561-574.
- [57] A. Saai, H. Louche, L. Tabourot, H.J. Chang. Experimental and numerical study of the thermo-mechanical behavior of Al bi-crystal in tension using full field measurements and micromechanical modeling. *Mech. Mater.* 42 (2010) 275-292.
- [58] A. Mayanadier, M. Poncelet, K. Lavernhe Taillard, S. Roux. One shot measurement of thermal and kinematic fields: Infrared image correlation (IRIC). *Exp. Mech.* 52 (2012) 241-255.
- [59] L. Bodelot, L. Sabatier, E. Charkaluk, P. Dufrenoy. Experimental setup for fully coupled kinematic and thermal measurements at the microstructural scale of AISI 316 steel. *Mater. Sci. Eng. A* 501 (2009) 52-60.
- [60] L. Bodelot, E. Charkaluk, L. Sabatier, P. Dufrenoy. Experimental study of heterogeneities in strain and temperature fields at the microstructural level of polycrystalline metals through fully coupled full field measurements by digital image correlation and infrared thermography. *Mech. Mater.* 43 (2011) 654-670.
- [61] L.P. Kublin, Y. Estrin. Strain nonuniformities and plastic instabilities. *Revue Phys. Appl.* 23 (1988) 573-583.
- [62] E.O. Hall. *Yield Point Phenomena in Metals and Alloys*. Macmillan, London, (1970).
- [63] W.E. Dalby. Load-Extension Diagrams Taken with the Optical Load-Extension Indicator. *Proc. Roy. Soc. A* 88 (1913) 281-288.

-
- [64] E.O. Hall. The deformation and ageing of mild steel - III Discussion of results. Proc. Phys. Soc. B. 64 (1951) 747-502.
- [65] A.H. Cottrell, B.A. Bilby. Dislocation theory of yielding and strain ageing of iron. Proc. Phys. Soc. A 62 (1949) 49-61.
- [66] W. Sylwestrowicz, E.O. Hall. The deformation and ageing of mild steel. Proc. Phys. Soc. B. 64 (1951) 495-502.
- [67] J.J. Gilman, W.G. Johnston. Dislocations and mechanical properties of crystals. John Wiley (1957).
- [68] G.T. Hahn. A model for yielding with special reference to the yield point phenomena of iron and related BCC metals. Acta Metall. 10 (1962) 727-738.
- [69] A.H Cottrell. Symposium on Plastic Deformation of Crystalline Solids, Carnegie Institute of Technology (1950) 60.
- [70] J.C. Suits, B. Chalmers. Plastic microstrain in silicon-iron. Acta. Metall. 9 (1961) 854-860.
- [71] R. Rosenberg. Pre-upper-yield-point initiation of a Lüders band in pure iron Acta Metall. 13 (1965) 561-563.
- [72] N.J. Petch. The upper yield stress of polycrystalline iron. Acta Metall. 12 (1964) 59-65.
- [73] P.J. Worthington. The upper yield stress of polycrystalline 3% silicon iron. Acta Metall. 15 (1967) 1795-1798.
- [74] P.J. Worthington. Slip propagation in polycrystalline 3% silicon-iron. Acta Metall. 14 (1966) 1015-1017.
- [75] D.W. Moon, T. Vreeland. The initiation of yielding in silicon-iron. Acta Metall. 17 (1969) 989-996.

-
- [76] P.J. Worthington, E. Smith. The formation of slip bands in polycrystalline 3% silicon iron in the pre-yield microstrain region. *Acta Metall.* 120 (1964) 1277-1281.
- [77] W.E. Carryington, D. McLean. Slip nuclei in silicon iron. *Acta Metall.* 13 (1965) 493-499.
- [78] S. Mahajan, D. Brasen, P. Haasen. Lüders bands in deformed silicon crystals. *Acta Metall.* 27 (1979) 1165-1173.
- [79] W. Bonfield. Some observations on the microstrain characteristics of silver. *Acta Metall.* 13 (1965) 551-554.
- [80] V.S. Ananthan, E.O. Hall. Microscopic shear bands at Lüders fronts in mild steel. *Scripta Metall.* 21 (1987) 519-520.
- [81] V.S. Ananthan, E.O. Hall. Surface features of microscopic shear bands at Lüders fronts in mild steel. *Scripta Metall.* 27 (1987) 1699-1704.
- [82] V.S. Ananthan, E.O. Hall. Shear and kink angles at the Lüders band front. *Scripta Metall.* 23 (1989) 1075-1089.
- [83] W.M. Lomer. The yield point phenomenon in polycrystalline in mild steel. *J. Mech. Phys. Solids.* 1 (1952) 64-73.
- [84] E.O. Hall. The deformation and ageing of mild steel - II Characteristics of Lüders deformation. *Proc. Phys. Soc. B.* 64 (1951) 742-747.
- [85] J.F. Butler. Lüders front propagation in low carbon steels. *J. Mech. Phys. Solids* 10 (1962) 313-334.
- [86] V.S. Ananthan, E.O. Hall. Macroscopic aspects of Lüders band deformation in mild steel. *Acta Metall. Mater.* 39 (1991) 3153-3160.
- [87] D.E. Delwiche, D.W. Moon. Orientation of Lüders band fronts. *Mater. Sci. Eng.* 7 (1971) 203-207.

-
- [88] H.B. Sun, F. Yoshida, M. Ohmori, X. Ma. Effects of strain rate on Lüders band propagation velocity and Lüders strain for annealed mild steel under uniaxial tension. *Mater. Lett.* 57 (2003) 4535-4539.
- [89] D.J. Lloyd, L.R. Morris. Lüders band deformation in a fine grained aluminium alloy. *Acta Metall.* 25 (1977) 857-861.
- [90] N. Balasubramaniam, J.C.M. Li, M. Gensamer. Plastic deformation and Lüders band propagation in α -Brass. *Mater. Sci. Eng.* 14 (1974) 37-45.
- [91] H. Fujita, S. Miyazaki. Lüders deformation in polycrystalline iron. *Acta Metall.* 26 (1978) 1273-1281.
- [92] S. Miyazaki, H. Fujita. Dynamic observation of the process of Lüders band formation in polycrystalline iron. *Trans. Jpn. Inst. Mets.* 20 (1979) 603-608.
- [93] K. Prewo, J.C.M. Li, M.Gensamer. Lüders band motion in iron. *Metall. Trans.* 3 (1972) 2261-2269.
- [94] T. Vreeland, D.S. Wood, D.S. Clark. Preyield plastic and anelastic microstrain in low-carbon steel. *Acta Metall.* 1 (1953) 414-421.
- [95] N. Brown, K.F. Lukens. Microstrain in polycrystalline metals. *Acta Metall.* 9 (1961) 106-111.
- [96] B.J. Shaw, G.A. Sargent. Stress relaxation prior to the yield point in niobium and molybdenum. *Acta Metall.* 12 (1964) 1225-1230.
- [97] Z. Lining, Z. Ping, Z. Jinyin. Resistance of metals to microstrain and its influential factors. *Acta Metall. Sin. B* 3 (1990) 420-425.
- [98] G.T. Van Rooyen. Basic factors which influence the Lüders strain during discontinuous yielding. *Mater. Sci. Eng.* 7 (1971) 37-48.
- [99] J.C. Fisher, H.C. Roger. Propagation of Lüders bands in steel wires. *Acta Metall.* 4 (1956) 180-185.

-
- [100] J. Zhang, Y. Jiang. Lüders bands propagation of 1045 steel under multiaxial stress state. *Int. J. Plast.* 21 (2005) 651-670.
- [101] J. Zhang, Y. Jiang. A study of inhomogeneous plastic deformation of 1045 steel. *ASME J. Eng. Mater. Tech.* 126 (2004) 164-170.
- [102] G.T. Van Rooyen. The stress and strain distribution in a propagating Lüders front accompanying the yield-point phenomenon in iron. *Mater. Sci. Eng.* 3 (1968/69) 105-117.
- [103] D.W. Moon. Strain distribution through a propagating Lüders band front. *Scripta Metall.* 5 (1971) 213-216.
- [104] R. Iricibar. Meaning of the strain profile of a propagating Lüders band front. *Scripta Metall.* 9 (1975) 1045-1050.
- [105] R. Iricibar. The microscopic strain profile of a propagating Lüders band front in mild steel. *Scripta Metall.* 9 (1975) 1051-1058.
- [106] R. Iricibar. The contribution of creep to the strain profile of a propagating Lüders band front in mild steel. *Scripta Metall.* 10 (1976) 289-294.
- [107] C. Scruby, H. Wadley, J.E. Sinclairs. The origin of acoustic emission during deformation of aluminium and an aluminium-magnesium alloy. *Philos. Mag. A* 44 (1981) 249-274.
- [108] D.L. Armentrout, H. Carpenters. An investigation on Lüders band deformation and the associated acoustic emission in Al-4.5 Mg alloys. *J. Acoust. Emission* 15 (1997) 43-52.
- [109] A. Lazarev, A. Vinogradov. About plastic instabilities in iron and power spectrum of acoustic emission. *J. Acoustic Emission* 27 (2009) 144-156.
- [110] T.V. Muravev, L.B. Zuev. Acoustic emission during the development of a Lüders band in a low-carbon steel. 53 (2008) 1094-1098.

-
- [111] Z. Han, H. Luo, H. Wang. Effects of strain rate and notch on acoustic emission during the tensile deformation of a discontinuous yielding material. *Mater. Sci. Eng. A* 528 (2011) 4372-4380.
- [112] A.A. Shibkov, A.E. Zolotov. Acoustic and optical monitoring of Lüders band in aluminium-magnesium 5456 alloy. *Crystallogr. Rep.* 56 (2011) 141-148.
- [113] M.A. Campos, C. Sanchez. Magnetic Barkhausen measurements to evaluate formation of heterogeneous plastic deformation zones in carbon steel. Fourth Conferencia Panamericana de END Buenos Aires - October (2007) 1-9.
- [114] J.C. Sanchez, M.A. Campos, L.R. Padovese. Magnetic Barkhausen measurements for evaluating the formation of Lüders bands in carbon steel. *NDT&E Inter.* 40 (2007) 520-524.
- [115] A. Dhar, L. Clapham, D.L. Atherton. Influence of Lüders band on magnetic Barkhausen noise and magnetic flux leakage signals. *J. Mat. Sci.* 37 (2002) 2441-2446.
- [116] O. Stupakov, T. Uchimoto, T. Takagi. Magnetic anisotropy of plastically deformed low-carbon steel. *J. Phys. D: Appl. Phys.* 43 (2010) 1-6.
- [117] S. Yoshida, H. Ishii, K. Ichinose, K. Gomi, K. Taniuchi. An optical interferometric band as an indicator of plastic deformation front. *Trans. ASME* 72 (2005) 792-794.
- [118] B. Guelorget, M. Francois, G. Montay. Strain localization band width evolution by electronic speckle pattern interferometry strain rate measurement. *Scripta Mater.* 60 (2009) 647-650.
- [119] R. Shabadi, S. Kumar, H.J. Roven, E.S. Dwarakadasa. Characterisation of PLC band parameters using laser speckle technique. *Mater. Sci. Eng. A* 364 (2004) 140-150.

- [120] H. Louche, A. Chrysochoos. Thermal and dissipative effects of accompanying Lüders band propagation. *Mater. Sci. Eng. A*. 307 (2001) 15-22.
- [121] B. Wattrisse, A. Chrysochoos, J.M. Muracciole, M. Nemoz-Gaillard. Kinematic manifestations of localisation phenomena in steels by digital image correlation. *Eur. J. Mech. A* 20 (2001) 189-211.
- [122] E.S. Lukin, A.M. Ivanov, B.G. Vainer. Thermal imaging investigations in experimental mechanics. *Russ. J. Nondestruct.* 39 (2003) 472-477.
- [123] E.A. Moiseichik. Heat generation and fracture initiation in a stretched steel plate with a process induced structural defect. *J. Appl. Mech. Tech. Phys.* 54 (2013) 116-123.
- [124] S. Dumoulin, H. Louche, O.S. Hopperstad, T. Borvik. Heat sources, energy storage and dissipation in high-strength steels: experiments and modeling. *Euro. J. Mech. A/Solids* 29 (2010) 461-471.
- [125] J. Wullink, F. Van Den Berg, P. Van Liempt, M. De Haas. Thermography applied to the evaluation of non-uniform deformation heat of metals. *QIRT* 5 (2008) 69-80.
- [126] R. Nogueira De Codes, O.S. Hopperstad, O. Engler, O.-G. Lademo, J.D. Embury, A. Benallal. Spatial and Temporal Characteristics of Propagating Deformation Bands in AA5182 Alloy at Room Temperature. *Metall. Mater. Trans. A* 42A (2011) 3358-3369.
- [127] X. Feng, G. Fisher, R. Zielke, B. Svendsen, W. Tillmann. Investigation of PLC band nucleation in AA5754. *Mater. Sci. Eng. A* 539 (2012) 205-210.
- [128] J. Coer, P.Y. Manach, H. Laurent, M.C. Oliveira, L.F. Menezes. Piobert-Lüders plateau and Portevin- Le Chatelier effect in an Al-Mg alloy in simple shear. *Mech. Res. Comm.* 48 (2013) 1-7.

- [129] D.W. Beardsmore, J. Quinta da Fonseca, J. Romero, C.A. English, S.R. Ortner, J. Sharples, A.H. Sherry, M.A. Wilkes. Study of Lüders phenomena in reactor pressure vessel steels. *Mater. Sci. Eng. A* 588 (2013) 151-166.
- [130] X. Maldague. *Theory and practice of infrared technology for nondestructive testing*, John Wiley & Sons, INC. (2001).
- [131] <http://www.photonics.com/EDU/Handbook.aspx?AID=25132>
- [132] X. Maldague. *Nondestructive testing handbook, third edition: Infrared and thermal testing*, ASNT (2001).
- [133] http://www.ips-innovations.com/bilder/blackbody_emissive.gif
- [134] W. Sharpe. *Springer handbook of experimental solid mechanics*, Springer (2008) 565-600.
- [135] J. Chen, G. Xia, K. Zhou, G. Xia, Y. Qin. Two step digital image correlation for micro-region measurement. *Opt. Lasers Eng.* 43 (2005) 836-846.
- [136] B. Pan, K. Qian, H. Xie, A. Asundi. Two dimensional digital image correlation for in-plane displacement and strain measurement: a review. *Meas. Sci. Tech.* 20 (2009) 1-17.
- [137] P. Vacher, S. Dumoulin, F. Morestin, S.M. Touchal. Bidimensional strain measurement using digital images. *Proc. Instn. Mech. Engrs. Part C J. Mech. Eng. Sci.* 213 (2011) 811-817.
- [138] G. Caglioti, *Mechanical properties and behaviour of solids: Plastic instabilities*, World Scientific Publishing Company (1986).
- [139] George. E. Dieter, *Mechanical Metallurgy*, Mc Graw-Hill (1988).
- [140] T. Vreeland, D.S. Wood, D.S. Clark. *Trans. Am. Soc. Metals.* 45 (1953) 620-624.

-
- [141] R.N. Mudrock, M.A. Lebyodkin, P. Kurath, A.J. Beaudoin, T.A. Lebedkina. Strain rate fluctuations during macroscopically uniform deformation of a solution-strengthened alloy. *Scripta Mater.* 65 (2011) 1093-1096.
- [142] J. Friedel, *Dislocations*, 1967, 1st ed., Pergamon Press Ltd.
- [143] S. Kyriakides, J.E. Miller. On the propagation of Lüders bands in steel strips. *J. Appl. Mech.* 67 (2000) 645-654.
- [144] A.W. Sleswyk, D.J. Verel. The rate determining process in Lüders band growth. *Scripta Metall.* 6 (1972) 677-679.
- [145] A. Chrysocoos, H. Louche. An infrared image processing to analyse the calorific effects accompanying strain localization. *Int. J. Eng. Sci.* 38 (2000) 1759-1788.
- [146] J.M. Muracciole, B. Wattrisse, A. Chrysochoos. Energy balance of a semicrystalline polymer during local plastic deformation. *Strain* 44 (2008) 468-474.
- [147] P. Germain, Q.S. Nguyen, P. Suquet. Continuum thermodynamics. *J. Appl. Mech.* 50 (1983) 1010-1020.
- [148] A. Chrysochoos. Infrared thermography applied to the analysis of material behavior: A brief overview. *QIRT* 9 (2012) 193-208.
- [149] V. Romanova, R. Balokhonov, S. Schmauder. *Mater. Sci. Eng. A.* 528 (2011) 5271-5277.